

Three-dimensional Printing of Conductive Composite for Wireless Chemical Sensor Systems

by
Taeil Kim

M.Sc., Korea Advanced Institute of Science and Technology, 2004

B.Sc., Pohang University of Science and Technology, 2002

Thesis Submitted in Partial Fulfillment of the
Requirements for the Degree of
Doctor of Philosophy

in the
School of Mechatronic Systems Engineering
Faculty of Applied Sciences

© Taeil Kim 2019

SIMON FRASER UNIVERSITY

Fall 2019

Copyright in this work rests with the author. Please ensure that any reproduction or re-use is done in accordance with the relevant national copyright legislation.

Approval

Name: Taeil Kim

Degree: Doctor of Philosophy

Title: Three-dimensional Printing of Conductive Composite for Wireless Chemical Sensor Systems

Examining Committee:

Chair: Helen Bailey
Lecturer

Woo Soo Kim
Senior Supervisor
Associate Professor

Byron Gates
Supervisor
Associate Professor
Department of Chemistry

Edward Jung Wook Park
Supervisor
Professor

Faranak Farzan
Internal Examiner
Assistant Professor

Tse Nga Ng
External Examiner
Associate Professor
Electrical and Computer Engineering
University of California, San Diego

Date Defended/Approved: September 6, 2019

Abstract

Three-dimensional (3D) printing technologies were developed in a variety of processes and applied in various fields such as manufacturing, healthcare, construction, etc. The extrusion-based 3D printing is one of the major 3D printing technologies which usually uses filaments or ink materials. Viscous liquid type ink materials may include polymer matrix and filler materials which are optimized to formulate the ink with the required printability with shear thinning behavior and functionality based on electrical conductivity or dielectric properties. The property of prints will largely depend on the choices of the polymer matrix and filler materials as well as types of printing technologies. The objective of this study is to understand the electrical properties of prints depending on printing parameters such as nozzle shapes and interaction between polymer matrix and fillers. The cross-sectional shapes of nozzles determine the flow of matrix material and fillers and affect the orientation of conductive fillers with a high aspect ratio like silver nanowires (AgNWs) in prints, which has a close relationship with the conductivity of prints. Matrix materials also play a significant role for the orientation of fillers in prints. Rod-like CNCs work like a media for AgNWs to move or rotate freely in it. In contrast, CNFs have shapes like spaghetti noodles which prevent AgNWs from moving or rotating in the matrix. A wireless electro-chemical sensing platform was developed by using 3D printable conductive cellulose composite. An inductor and capacitor (LC) resonator was prepared from a conductive nanocellulose ink by extrusion 3D printing for RF wireless chemical sensing. This LC resonator printed by direct ink writing with AgNW-CNF ink material was connected to an ion selective membrane electrode (ISME) to make a wireless sensor system which is a series connection of an LC resonator and an ISME. This wireless ISME-LC sensor was demonstrated with high selectivity and sensitivity of detection. This thesis demonstrated wireless ion-selective sensing using RF communication. To our best knowledge, this is the first thesis which report on wireless detection of selective ions from an ISME integrated with a wireless LC circuit. As an application of wireless sensing platform, wireless chemical sensing robot was developed by 3D printing using eco-friendly conductive composites based on nanocellulose. The aforementioned ISME-LC sensor was embedded on the tip of humanoid robotic fingers which actuated by quantitative chemical sensing of primary ions and demonstrated with an intelligent sensing robot. It is expected that this disposable wireless sensing robot system composed of simple ISME and LC will open an innovative way to contribute in the various sensing robot applications.

Keywords: extrusion-based 3D printing; eco-friendly cellulose materials; wireless chemical sensing; sensing robot

*Dedicated to my lovely wife, Amy Hyejung
and my precious sons,
Daniel Juhwan and Timothy Juhyun*

Acknowledgements

I would like to express my sincere gratitude to my senior supervisor Dr. Woo Soo Kim, for giving me the special opportunity to work with him and providing great advice and support during my PhD study. I am thankful for your guidance and insights as well as patience over the past four years. I would like to thank Michael Hausmann, Dr. Gilberto Siqueira, and Dr. Tanja Zimmermann from Swiss Federal Laboratories for Materials Science and Technology (Empa) who contributed to the research of 3D Printed Disposable Wireless Ion Sensors with Biocompatible Cellulose Composites. I also thank Dr. Hyunmin Park from Korea Research Institute of Standards and Science (KRISS) who encouraged a lot in many ways for lab members during his visit for one year.

I would like to thank my thesis examining committee members, Dr. Byron Gates and Dr. Edward Jung Wook Park for accepting to be my advisory committee, spending time to review my work, and supporting throughout. I would like to thank the examining committee, Dr. Faranak Farzan and Dr. Tse Nga Ng as well as the chair of the session, Dr. Helen Bailey for accepting to be part of my thesis defense. I would like to thank the staff and students of the Mechatronic Systems Engineering of Simon Fraser University for being kind and supportive. I would also acknowledge the use of shared facilities at 4D LABS supported by the Canada Foundation for Innovation (CFI), British Columbia Knowledge Development Fund (BCKDF), Western Economic Diversification Canada (WD), and Simon Fraser University (SFU).

I am deeply thankful for my lab mates of Additive Manufacturing Lab (AML) who helped me and shared precious time together. Thank you, Manpreet, Chao, Xin, Jae Sung, Abrar, Yue, Seonghyeon, Tae Ho, Daina. I also thank all co-op students from SFU, Varis, Ramita, Tom, Ryan, Kevin, Lucas as well as Global Intern Students from City University of Hong Kong, Ng, Riaz, Mandy, Louis, Jacky, and Chun Fai. I really enjoyed discussing interesting ideas with you as well as having picnics and dining out together. I really appreciate all the time we spent together.

Lastly, I am deeply grateful to my wife, Amy for awesome support and encouragement over the years and for being patient. I would like to thank my precious two sons Daniel and Tim for giving me creative ideas and joy during my study. I would like to thank all of my friends for their love and care. It was so helpful, wonderful, and beautiful.

Table of Contents

Approval.....	ii
Abstract.....	iii
Dedication.....	v
Acknowledgements.....	vi
Table of Contents.....	vii
List of Figures.....	x
List of Tables.....	xiii
List of Acronyms.....	xiv
Nomenclature and Greek Symbols.....	xvi
Chapter 1. Introduction.....	1
1.1. Background and Motivation.....	1
1.2. Objectives and Scope of Thesis.....	3
1.3. Thesis Organization.....	5
Chapter 2. Literature Review.....	8
2.1. 3D Printing Materials.....	8
2.1.1. Polymers and Composites.....	9
2.1.2. Metals and Alloys.....	13
2.1.3. Ceramics.....	14
2.2. 3D Printing Technologies.....	15
2.2.1. Overview of 3D Printing Techniques.....	15
2.2.2. Fused Deposition Modeling.....	17
2.2.3. Direct Ink Writing (DIW).....	17
2.2.4. Powder Bed Fusion.....	18
2.2.5. Stereo Lithography.....	18
2.2.6. Direct Energy Deposition.....	19
2.3. 3D Printed Electronics Applications.....	19
2.3.1. Overview.....	19
2.3.2. Electro-chemical Sensors.....	20
Ion Selective Membrane Electrodes (ISME).....	21
2.3.3. RF Wireless Sensing.....	22
Inductor Capacitor (LC) Resonator.....	22
Passive RFID System.....	24
Active RFID System.....	26
Chapter 3. Nozzle-dependent Extrusion-based 3D Printing.....	28
3.1. Abstract.....	28
3.2. Introduction.....	29
3.3. Materials and Methods.....	33
3.3.1. Photo-curable Extrusion Printing System – Print & Cure.....	33
3.3.2. Preparation of AgNW/P&C Resin Printed Samples.....	33

3.3.3. Simulation of Printing Composite	33
3.4. Results and Discussion	34
3.4.1. Filler Extrusion Simulation	34
3.4.2. Filler Distribution Morphology	39
3.4.3. Dielectric Permittivity	40
3.5. Conclusion.....	43
Chapter 4. Matrix-dependent Extrusion-based 3D Printing.....	45
4.1. Abstract.....	45
4.2. Introduction.....	45
4.3. Comparison of Filler Alignment Depending on Matrix Materials	47
4.4. Resistivity and Printable Properties of CNF-AgNW Ink	51
4.5. Conclusion.....	53
Chapter 5. Wireless Chemical Sensing and Sensing Robot.....	54
5.1. Abstract	54
5.2. Introduction.....	55
5.3. Results and Discussion	58
5.3.1. Humanoid Robot Finger's Sensor Design and Fabrication.....	58
5.3.2. The Selection of Optimal LC Circuits	59
5.3.3. Simulation of Input Impedance with Different Quality Factor	62
5.3.4. Quality Factor Depending on the Thickness of Printed LC.....	62
5.3.5. Wireless Ion Detection System	65
5.3.6. Characterization of ISME-LC Sensors on Humanoid Fingers.....	69
5.3.7. Demonstration of Differential Motion of Humanoid Fingers	70
5.4. Materials and Methods	73
5.4.1. Fabrication of LC Circuits and Electrodes	73
5.4.2. Fabrication of Humanoid Robotic Finger.....	74
5.4.3. Actuating Mechanism of Humanoid Finger	74
5.5. Conclusion.....	75
Chapter 6. Conclusions and Future Work	77
6.1. Conclusions.....	77
6.2. Contributions	81
6.3. Publications.....	82
6.4. Opportunities for Future Work.....	83
References	85
Appendix A. Journal paper discussed in Chapter 3.....	99
Appendix B. Journal paper discussed in Chapter 4 and 5.....	108
Appendix C. Journal paper discussed in Chapter 5.....	116
1. Introduction	118
2. Results	120

2.1. 3D-printed embedded chemical sensor design for humanoid robot fingers	120
2.2. The selection of optimal LC circuits.....	121
2.3. Simulation of input impedance with different Q factor.....	122
2.4. Characterization of ISME-LC sensors on the humanoid hand	123
2.5. Demonstration of differential motion of humanoid fingers depending on ion concentration	124
3. Conclusion	126
4. Experimental Section	127
Supporting Information	128
Acknowledgements	128
References.....	129

List of Figures

Figure 1.1.	Schematic illustration of a direct ink writing technique, continuous filament writing. [3].....	3
Figure 2.1.	Polymerization profiles of five different UVcurable systems (1: acrylate, 2: vinyl ether, 3: cycloepoxide, 4: methacrylate, and 5: glycidyl ether). [12]	10
Figure 2.2.	a) Electrical conductivity depending on MWCNT content in PLA. The inset is the log–log plot of the electrical conductivity depending on the volume fraction of MWCNTs; b) SEM micrograph of cryo-fractured 3D printed MWCNT/PLA nanocomposites (10 wt% MWCNT in PLA). [13]	11
Figure 2.3.	The mechanism of producing CNC and CNF from cellulose. [14].....	12
Figure 2.4.	Tensile strength, Elongation, Tensile modulus, and Fracture energy for 3D printed PEGDA hydrogels depending on CNC loading. [15]	12
Figure 2.5.	Schematic illustration of the integration of current distributor, bipolar plate, gasket, and LGDL into one AM plate via additive manufacturing. [16]....	14
Figure 2.6.	Additive manufacturing process of polymer-derived ceramics. a) UV-curable monomers and photo initiator are mixed; b) UV light cures the resin using a SLA 3D printer or a patterned mask; c) A 3D printed pre-ceramic polymer part; d) Polymer-derived ceramic after the pyrolysis. [17]	15
Figure 2.7.	Four main methods of additive manufacturing; a) fused deposition modelling; b) inkjet printing; c) SLA; d) powder bed fusion. [18]	16
Figure 2.8.	Miniaturization of pH sensors. Four conventional potentiometric pH sensors are shown on the left side. The three sensors on the right side are printed. [33]	20
Figure 2.9.	Schematics for the preparation of a sodium ion-sensing screen-printed electrode. [36]	22
Figure 2.10.	a) Schematic representation of an LC sensor interrogating system; b) Equivalent circuit of an LC sensor interrogating system. [37]	23
Figure 2.11.	Characteristic curve of Re (Z_{in}) and Phase (Z_{in}). [37]	24
Figure 2.12.	Near-field communication using inductive coupling. [38]	25
Figure 2.13.	Near-field RFID tags for different applications [38]	25
Figure 2.14.	Far-field RFID tags for different applications [38].....	26
Figure 2.15.	Active RFID reader for a large-scale active RFID system [39]	27
Figure 2.16.	Active RFID tag for a large-scale active RFID system [39]	27
Figure 3.1.	Schematics of the extrusion at nozzles and Print & Cure extrusion 3D printing system. a) The scheme of print-induced aligned/random distribution of high aspect ratio fillers of a circular nozzle and a flat nozzle; b) The scheme of Print & Cure extrusion 3D printing system (up) and a close-up image of Print & Cure printing head (bottom).	32
Figure 3.2.	Filler extrusion simulation depending on nozzle shapes. Velocity profile of the fluid extruded at a circular nozzle (a) and a flat nozzle (b), and Average Velocity Y, Z, and X (c, d, and e) of fluid around the exit of a circular nozzle and a flat nozzle.	37

Figure 3.3.	Filler distribution morphology. Optical microscope images of Print & Cure samples printed through a circular nozzle (a) and a flat nozzle (b) and SEM images of cross sections of samples printed through a circular nozzle (c) and a flat nozzle (d).....	40
Figure 3.4.	Permittivity of Print & Cure (AgNW vol. fraction: 0, 0.2, 1.6 %) and Silicone (AgNW vol. fraction: 0, 0.2 %) samples printed with a circular or a flat nozzle.	41
Figure 3.5.	The RFID tag design and the detection of a fabricated RFID tag by an RFID reader. a) Design of antenna and circuit layout; b) Detection of the RFID tag consisted of an antenna printed with AgNW (1.5% vol. fraction) and P&C resin composite through a flat nozzle and interconnected with an RFID chip; c) Temperature sensing result from 25 to 40 °C: yellow bars show heater's temperature (25, 35, and 40 °C) and, blue bars show corresponding temperature detected by the RFID tag (26, 35, and 41 °C).	42
Figure 4.1.	Comparison of printed CNF-AgNW ink and CNC-AgNW ink. a) Schematic of printed CNF-AgNW ink; b) Schematic of printed CNC-AgNW ink; c) Microscopic images of printed ink of 36 wt% AgNW in CNF; d) Microscopic images of printed ink of 30 wt% AgNW in CNC.	48
Figure 4.2.	Comparison of AFM images of printed cellulose-AgNW inks. a) shows AFM image of printed nanofibril (CNF)-AgNW ink; b) shows AFM image of printed CNC-AgNW ink.	49
Figure 4.3.	Cordinate system in the computation of fiber's radial motion and rotation. [104].....	50
Figure 4.4.	Resistivity and printable properties of CNF-AgNW ink. a) Resistivity of CNF-AgNW ink; b) 3D printing schematics of an antenna; c) 3D printed antenna on a hemisphere; d) Corresponding graphs of magnitude of reflection coefficient S_{11} (black) and the real part of input impedance depending on frequency (red).	52
Figure 4.5.	The rheological properties of CNF-AgNW ink. a) shows how storage modulus (G') and loss modulus (G'') of CNF-AgNW ink change when the shear stress changes; b) depicts the relationship between viscosity and shear rate which shows a typical shear thinning behavior.	53
Figure 5.1.	Schematics of wireless sensing overview and 3D printing. a) Experimental setup for wireless chemical sensing; b) 3D printing sequence of humanoid finger body by FFF, followed by DIW printing.	59
Figure 5.2.	Characterization of wireless LC circuits. a) Designs for 3D printing/Wireless characterization of LCs with different inductor shapes (Square, Hexagonal, Octagonal, Circular) with 3 turns; b) Calculated inductance values for 12 types of designs (The alphabet shows the shape of inductors. (S: Square, O: Octagonal, H: Hexagonal, C: Circular) The number means the number of turns.); c) Simulated relation between the conductivity across ISME and maximum real part of input impedance; d) Simulated distribution of H field around the chosen square type LC for the conductivity of 0.1 and 6 S/m across ISME; e) H field distribution comparison of simulation results for the conductivity of 0.1 and 6 S/m across ISME.	60
Figure 5.3.	Q factor depending on LC thickness. a) Design of LC circuit with different height of IDC; b) Design of LC circuit with different height of inductor; c)	

	Simulation result for the $\max(\text{re}(Z_{in}))$ depending on the thickness of IDC or inductor; d) Experiment result of resonant frequency intensity depending on the thickness of IDC or inductor.....	63
Figure 5.4.	3D printed inductor-capacitor (LC) circuits with different thickness. a) shows three LC samples with different printing paths. For example, 2L8C contains doublelayered inductor and 8-layered capacitor (C4 in Figure 5.3 a). Eight different samples were measured for R_i change in Figure 5.3 d; b) shows the thickness of CNF-AgNW ink depends on the number of printing paths.	64
Figure 5.5.	The equivalent circuit of sensor system - shows an equivalent circuit of the sensor system consisted of an ion selective membrane electrode (ISME) (sensing part) and inductor-capacitor (LC) circuit part.	66
Figure 5.6.	Raw data for selectivity of ISME with NH_4^+ membrane - shows the change of magnitude of S_{11} in ISME with NH_4^+ membrane depending on the frequency change for 4 different concentrations of NH_4Cl solution. This graph is the raw data of the selectivity of ISME with NH_4^+ membrane (Figure 5.7).....	66
Figure 5.7.	Wireless ion detection system. a) Schematic of IS-LC sensor design and loop antenna with VNA; b) Printed sample of IS-LC sensor; c) Experimental result of IS-LC sensor with NH_4^+ membrane.....	67
Figure 5.8.	Experimental result of IS-LC sensor with NH_4^+ membrane – shows ΔR_i intensity of ISME with NH_4^+ membrane depending on 4 different concentrations of NH_4^+ and K^+ ion.....	68
Figure 5.9.	Qualification of wireless sensing of LC circuit connected with embedded ISME sensors. a) Design images of both sides (LC side and Sensor side) of a fingertip; b) Actual sample images of both sides of a fingertip; c) Electrical resistance change across K^+ ISME with application of different K^+ ion concentration; d) Electrical resistance change of NH_4^+ ISME applied with different ions such as 1 M NH_4^+ , 1 M K^+ , and 1 M Ca^{2+} ion solutions depending on time; e) R_i intensity change of the LC on a fingertip with the NH_4^+ ISME depending on NH_4^+ ion concentration.....	69
Figure 5.10.	Differential bending motion of humanoid fingers with quantitative chemical sensing. a) The schematic of humanoid robotic hand with a voltage divider circuit diagram; b) The actual image of fabricated humanoid robotic hand with three movable fingers for detecting primary ions; c) The resistance change depending on the K^+ ion concentration; d), e) Demonstration of different bending angle of the finger movement actuated by different K^+ ion concentrations to the extent defined for the voltage thresholds.	72

List of Tables

Table 1.	Coefficients for modified wheeler expression.	61
Table 2.	Coefficients for current sheet expression.	61

List of Acronyms

2PP	Two-Photon Polymerization
3D	Three-Dimensional
ABS	Acrylonitrile Butadiene Styrene
AFM	Atomic Force Microscopy
AgNW	Silver nanowire
AM	Additive Manufacturing
CAD	Computational Aided Design
CFD	Computational Fluid Dynamics
Cir	Circular
CNF	Cellulose Nanofiber
CNC	Cellulose Nanocrystal
CNT	carbon nanotube
DED	Direct Energy Deposition
DIW	Direct Ink Writing
DLF	Directed Light Fabrication
DLP	Digital Light Processing
DMD	Direct Metal Deposition
EBAM	Electron Beam AM
EM	Electromagnetic
EMF	Electromotive Force
EMI	Electromagnetic Interference
FDM	Fused Deposition Modeling
FFF	Fused Filament Fabrication
FETs	Field Effect Transistors
FIB	Focused Ion Beam
HF	High Frequency
IoT	Internet of Things
ISFETs	Ion Selective Field Effect Transistors
IS-LC	Ion-Selective inductor–capacitor
ISME	Ion Selective Membrane Electrode
LC	Inductor Capacitor
LCVD	Laser Chemical Vapor Deposition

LDM	Liquid Deposition Modelling
LF	Low Frequency
LGDL	Liquid/Gas Diffusion Layer
LIFT	Laser-Induced Forward Transfer
LSF	Laser Solid Forming
MWCNT	Multi-Walled Carbon Nanotubes
P&C	Print & Cure
PBF	Powder Bed Fusion
PDMS	Polydimethylsiloxane
PI	Polyimides
PMMA	Poly (methyl methacrylate)
PNCs	Polymer Nanocomposites
PVC	Polyvinyl Chloride
Q factor	Quality factor
RF	Radio Frequency
RFID	Radio-Frequency Identification
RTIR	Real-Time Infrared
SEM	Scanning Electron Microscope
SLA	Stereo Lithography
SLM	Selective Laser Melting
SLS	Selective Laser Sintering
STL	Stereo-Lithography
UHF	Ultra-High Frequency
UV	Ultra Violet
VNA	Vector Network Analyzer

Nomenclature and Greek Symbols

η_0	Zero-Shear-Rate Viscosity
λ	Natural Time
$\dot{\gamma}$	Shear Rate
m	Power-Law Index
ϵ_r	Relative Permittivity
ϵ_0	Vacuum Permittivity
$\Psi(\theta, t)$	Difference Between Values of Velocity at Both Ends of a Fiber
β	Correction Factor for the Nonlinear Variation of Velocities along the Length of the Fiber
d_{avg}	Average Diameter
d_{out}	Outer Diameter
d_{in}	Inner Diameter,
ρ	Fill Ratio,
R_S	Resistance of LC sensor
L_S	Inductance of LC sensor
C_S	Capacitance of LC sensor
K_1, K_2	Layout Dependent Coefficients
c_1, c_2, c_3	Layout Dependent Coefficients
R_f	Resonant Frequency
Z_{in}	Input Impedance

Chapter 1.

Introduction

1.1. Background and Motivation

Three-Dimensional (3D) printing which was initially called as rapid prototyping is now used interchangeably with additive manufacturing which was decided as the standard terminology in ASTM F42 committee in 2007. [1]

3D printing technologies have been developed in various types in order to realize the additive manufacturing with higher resolution and improved mechanical and electrical properties using optimized materials based on polymer, metal, and ceramic in types of filament, ink, or powder. The early 3D printing technology used photo-curable resin and a mask pattern or a scanning fiber transmitter to control UV exposure area. The fused deposition modeling (FDM) also known as fused filament fabrication (FFF) was developed later, which became the most commonly used 3D printing technology. [2] It is a representative type of the extrusion-based 3D printing technologies which uses nozzles and continuous filament material that passes through the heated nozzles and is deposited to build a 3D object on the printing bed.

One useful example of 3D printed structure is 3D periodic structures made of colloidal or polymeric materials. These structures can be used as sensors, microfluidic channels, and scaffolds for tissue engineering. Direct ink writing (DIW) 3D printing is an alternative type of the extrusion-based 3D printing methods and offers flexible choice of materials, low cost, and possibility to generate advanced 3D structure in multidisciplinary research fields. The term DIW describes that it involves the controlled movement of ink-extruding nozzles with respect to the printing bed to build designed structures. [3]

The ink is extruded through a nozzle by the pressure applied to the syringe which contains the ink and printed following the sliced patterns as shown in Figure 1.1. Viscous liquid type of ink materials are used for DIW 3D printing instead of filament materials used in FFF. The ink for DIW 3D printing can be formulated as colloidal suspensions, colloidal gels, and polymer melts according to the design requirements regarding printability as well

as mechanical and electrical properties of printed objects. For example, conductive fillers such as metal nanoparticle or nanowires as well as metal flakes may be added to a matrix material in order to prepare an ink that enables printing a conductive or a dielectric parts. It is well known that high aspect ratio fillers in matrix material may be aligned along the printing direction due to the shear stresses applied in the process of direct ink writing. It is necessary to find a new approach so that high aspect ratio fillers such as AgNWs are distributed randomly and generate a conductive percolation network to make printed parts conductive.

The motivation of this study is to understand how important factors of extrusion-based 3D printing have effects on electrical properties of 3D printed objects. For this objective, nozzle-dependent extrusion-based 3D printing was studied by experiments as well as simulations based on a finite element analysis to understand the distribution of high aspect ratio fillers in photo-curable resin depending on the shape of extrusion nozzles. Matrix-dependent extrusion-based 3D printing was also studied by experiments to understand the different results in terms of the distribution of high aspect ratio fillers in different matrix materials such as cellulose nanofiber (CNF) and cellulose nanocrystal (CNC). CNFs have flexible fiber shape like spaghetti noodles and form an entangled web-like network structure with higher aspect ratio. On the other hand, CNCs have rod like shape similar to whiskers with lower aspect ratio. [4]

3D printing technologies were massively applied in flexible electronics such as antenna and sensors because of the easy fabrication of flexible parts and cost effectiveness. There have been a lot of research on these printed electronics using conductive and dielectric ink materials. Eco-friendly printed electronics is also studied in terms of material preparation and degradation of printed objects as the pollution caused by using excessive plastic products is generating problems and issues around the world. The need to find solutions for renewable and sustainable material which can replace the plastic products is increasing. This trend is driving the research for 3D printed green electronics which can be realized by the development of sustainable and biodegradable materials for 3D printing such as cellulose based materials as well as 3D printing technologies which are optimized to these eco-friendly materials. Here eco-friendly chemical sensor printed with biodegradable nanocellulose inks using extrusion-based 3D printing is studied.

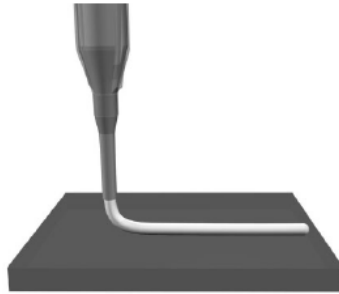


Figure 1.1. Schematic illustration of a direct ink writing technique, continuous filament writing. [3]

1.2. Objectives and Scope of Thesis

The overall objective of this thesis is to study photo-curable polymer or nanocellulose based composite material which can be used in extrusion-based 3D printing systems. This composite material can be used to build a printed flexible antenna for RFID communication system or a flexible disposable type or an embedded type sensors for wireless chemical sensing. To achieve this objective, the fundamental understanding of material properties such as electrical properties as well as printability of photo-curable polymer or nanocellulose based composite material is required. The conductivity of printed parts is one of the most important properties to study to enable the fabrication of these electrical components. The distribution of the conductive fillers in constituent materials was focused because the conductivity has a close relationship with this aspect. Therefore, the **first objective** is to study photo-curable polymer based composite material and the electrical properties of manufactured parts using Print&Cure system which uses UV light to cure the photo-curable polymer based composite material which includes conductive fillers, silver nanowires. The **second objective** is to study extrusion-based 3D printing focusing on the relationship between the nozzle shapes and the electrical properties of printed objects where two types of nozzles, circular and flat nozzles are used for the extrusion of the same photo-curable polymer based composite material. The **third objective** is to study extrusion-based 3D printing focusing on the relationship between the matrix materials of nanocellulose and the distribution of conductive fillers with high aspect ratio. Two types of ink materials were developed, one with CNF and the other with CNC which have silver nanowires in common to show different electrical properties. The **final objective** is to demonstrate sensor applications such as 3D printed RFID antenna, flexible

disposable chemical sensor, and embedded chemical sensor system for humanoid sensing robot system.

The scope of this thesis is to develop RF wireless communication systems and printed flexible or embedded chemical sensing systems based on the extrusion-based 3D printing of ink materials with conductive fillers in a polymeric or a nanocellulose constituent material. The scope of this thesis is described more specifically as below.

- 1) Composite inks which include photo-curable polymers and high aspect ratio conductive fillers are prepared for extrusion-based 3D printing. These inks are studied to understand the effect of nozzle shapes on the distribution of the fillers in the matrix material. The fillers distribution will eventually determine the electrical properties of the printed parts.
- 2) Biodegradable nanocellulose materials (CNC and CNF) were used as constituent material together with conductive fillers (AgNWs) to make a conductive ink for extrusion-based 3D printing and studied in terms of the electrical properties and printability. The resistivity of the ink depending on the ratio of conductive fillers was studied. The printability and the shear thinning behavior of the formulated ink were also examined.
- 3) For the wireless chemical sensing, ion selective membrane electrode (ISME) plus inductor capacitor (LC) circuit is explored and fabricated as disposable flexible sensors. The ISME was studied in terms of the sensitivity to detect different concentrations of the primary ion and the selectivity to show the ability to distinguish the primary ion from non-primary ions as the concentrations of these ion solutions change.
- 4) The LC was studied to optimize the wireless communication of this ISME-LC sensor system. The relationship between the quality factor of LC and the design parameters such as the shapes and turns of inductor, thickness of inductors and capacitors was studied by both experiments and simulations, which is also closely related to the readout distance of LC.
- 5) Embedded ISME-LC sensors on a humanoid robot hand is also studied. A simulation shows that stronger H field is generated around LC as the

conductivity between two electrodes of ISME increases, which is equivalent to the increasing concentration of primary ion solution. This robot hand demonstrated to perform smart movement of fingers triggered by chemical sensing of primary ions at the ISME on fingertips. Applying droplets of primary ion solution with higher concentrations resulted in bending movements of robot fingers with higher level of bending angles. However, the improvement of accuracy of the movement of robot fingers is out of the scope of this thesis.

- 6) It should be noted that the study towards achieving the statistical data from the experiment using numerous number of ISME-LC sensors is not the scope of this thesis.

Here the combination of ISME and LC resonator is chosen for primary ion detection and radio frequency (RF) wireless communication. This ISME-LC sensor is fabricated by using extrusion-based 3D printing technologies such as FFF and DIW 3D printing. Biodegradable and eco-friendly materials were utilized in DIW 3D printing systems to build disposable flexible sensor system as well as the embedded sensor system for a humanoid robot hand with bendable fingers which were obtained through FFF 3D printing.

1.3. Thesis Organization

The thesis is structured as a series of six chapters which includes four chapters of the research work of PhD program as well as an introduction and conclusion of this work. Chapter 3, 4, and 5 are written based on journal papers reported based on this work. There is overlapping information among these chapters inevitably. However, chapters 3, 4, and 5 start with the objective and the explanation of the approach used. The chapters are organized as follows:

Chapter 1 is dedicated to the background and motivations of the thesis, introduction of the extrusion-based 3D printing, and discussion of the need for the study on ink materials and extrusion-based 3D printing system. The objectives of this thesis work are also explained.

Chapter 2 provides a comprehensive literature review on three major aspects of this thesis: (i) *3D Printing Materials* such as polymers and composites, metals and alloys, and ceramics, (ii) *3D Printing Technologies* in the context of taking an overview and

reviewing five representative fabricating methods such as fused deposition modeling (FDM), DIW, powder bed fusion (PBF), stereo lithography (SLA), direct energy deposition (DED) using aforementioned various 3D printing materials, (iii) 3D *Printed Electronics Applications* focusing on Electro-chemical sensors and RF wireless sensing, which is the review of inductor capacitor (LC) resonator and passive and active RFID system.

Chapter 3 is titled as “Nozzle-dependent Extrusion-based 3D Printing”, which is equivalent to the published journal paper, *T. Kim, R. Trangkanukulkij and W. S. Kim, “Nozzle Shape Guided Filler Orientation in 3D Printed Photo-curable Nanocomposites”*. *Scientific Reports* **8** (2018) 3805”; with minor modifications. To investigate the effect of nozzle shape on electrical properties of extrusion-based 3D printing, experiments are designed to study dielectric property of extrusion-based 3D printed samples. Chapter 3 provides the observations and the results of extrusion-based 3D printed samples which were printed with nozzles of different shapes such as circular and flat (oval) cross sections.

Chapter 4 is titled as “Matrix-dependent Extrusion-based 3D printing”, which includes sections derived from the journal paper, *T. Kim, and W. S. Kim, “3D Printed Disposable Wireless Ion Sensors with Biocompatible Cellulose Composites”*. *Advanced Electronic Materials* **5** (2019) 1800778”; with minor modifications. To investigate the matrix dependent extrusion-based 3D printing, experiments are designed to study electrical properties of different nanocellulose composite materials which are composed of silver nanowires as a filler material in common and either CNF or CNC as a matrix material. Chapter 4 provides the observation result and measurement data of electrical properties of printed nanocellulose composites with different matrix materials.

Chapter 5, titled as “Wireless Chemical Sensing & Sensing Robot”, presents a flexible disposable ISME-LC sensor as well as an embedded ISME-LC sensor. This work is written into a journal paper which is accepted for publication, *T. Kim, M. Kaur, W. S. Kim, “Humanoid Robot Actuation Through Precise Chemical Sensing Signals”*. *Advanced Materials Technology* (2019); with minor modifications. Chapter 5 shows the optimization of LC circuit of different shape of inductors for improved Q factor. This chapter demonstrates the ISME-LC sensors applied to a flexible disposable sensor first. The ISME-LC sensors are also embedded in a humanoid robot finger and triggers the movement of fingers according to the predefined thresholds of primary ion concentrations. This chapter also gives the result of optimization of LC circuit thickness for higher quality

(Q) factor as well as the demonstration of wireless ion detection system, which is from the published journal paper, *T. Kim, and W. S. Kim, "3D Printed Disposable Wireless Ion Sensors with Biocompatible Cellulose Composites". Advanced Electronic Materials* **5** (2019) 1800778"; with minor modifications.

Finally, **Chapter 6** concludes the thesis by identifying the achievements, contributions, and novelties of this research work. Furthermore, provides possible improvements and future work that can be explored further.

Chapter 2.

Literature Review

The environment has been polluted by massive use and disposal of conventional polymers such as polyethylene and polypropylene. As a solution for this issue, biodegradable polymers have been developed, and the consumption of these eco-friendly materials is increased over the past years. Biodegradable materials were applied in packaging materials, consumer goods, and agricultural products. Various technologies were applied to realize eco-friendly 3D printing using biodegradable materials based on cellulose materials which are abundant, renewable, and sustainable.

Appropriate 3D printing technology as well as material preparation are necessary for 3D printing of biodegradable materials. Here two representative techniques such as 3D printing by photon energy and 3D printing by extrusion are briefly reviewed. The former technique is applied for printing urethane based photo-curable polymer. The latter technique is used to print biodegradable ink materials which are composed of nanocellulose, AgNW, and deionized water.

Chemical sensing is important and necessary in a wide range of fields such as environment, agriculture, and healthcare. Fast and cost effective solutions were widely studied for chemical sensing using printed electronics technologies. In this thesis, a novel ISME-LC sensor system is developed and studied to detect primary ions.

In the era of Internet of Things (IoT), wireless communication is taking place in every interfaces between data generating points and the data acquisition point. RF wireless communication system is one of the most representative approaches of wireless communication and is massively used in many applications such as tracking shipments, inventory checking, and building access. In this thesis, passive and active RF wireless communication systems are reviewed briefly.

2.1. 3D Printing Materials

3D printing technology supports various materials such as polymers, metals, ceramics, and composites of different types of materials as well as bio materials. Each of

these materials requires different additive processes which can be developed into a relevant 3D printing technologies. In this chapter 2.1., 3D printing materials such as polymers and composites which include nanocellulose materials, metals and alloys, ceramics are briefly reviewed. In chapter 3., 4., and 5., the main focus of 3D printing materials is on two types of materials such as photo-curable polymers and nanocellulose composite materials which were used to print electrical components such as antennae, inductors, and capacitors and fabricate sensing applications.

2.1.1. Polymers and Composites

Polymers are the most commonly used materials in 3D printing technologies. Polymers offer wide range of choice of material and can be adopted to various 3D printing methods such as SLA, Selective laser sintering (SLS), FDM, inkjet printing, etc. Various forms of polymers such as thermoplastic polymer filaments, resin, and powder are used for 3D printing. Numerous industrial applications have been made in medical and architectural fields utilizing the advantage of fast prototyping. However, the strength and functionality were lacking for the 3D printed pure polymers, and advanced polymer composite materials and suitable printing methods which provide higher mechanical strength and better performance have been developed. [5]

Thermoplastic polymer filaments such as Polylactic acid (PLA) and Acrylonitrile Butadiene Styrene (ABS) are used in FDM. PLA is environmentally friendly but is poor in terms of mechanical strength. ABS is good at mechanical strength but produces an odour while it is processed. [6] Thus, eco-friendly thermoplastic filaments which have good mechanical properties are desirable materials to be developed. 3D printed PLA showed better mechanical properties in both compression and tension compared to injection-moulded PLA. [7] The addition of fibre reinforcement may enhance the mechanical properties of polymers even though it is challenging. [8, 9] Different types of alumina fillers have been used with a polymer matrix material to improve mechanical properties of polymers and manufacture a wear-resistant filament material. [10, 11]

Photo-curable polymers were widely studied for 3D printing materials. Figure 2.1 shows typical polymerization profiles of five kinds of photo-curable systems. The conversion depending on exposure time was measured by Real-time infrared (RTIR) spectroscopy applying intense UV light to those photo-curable polymers. [12] UV light

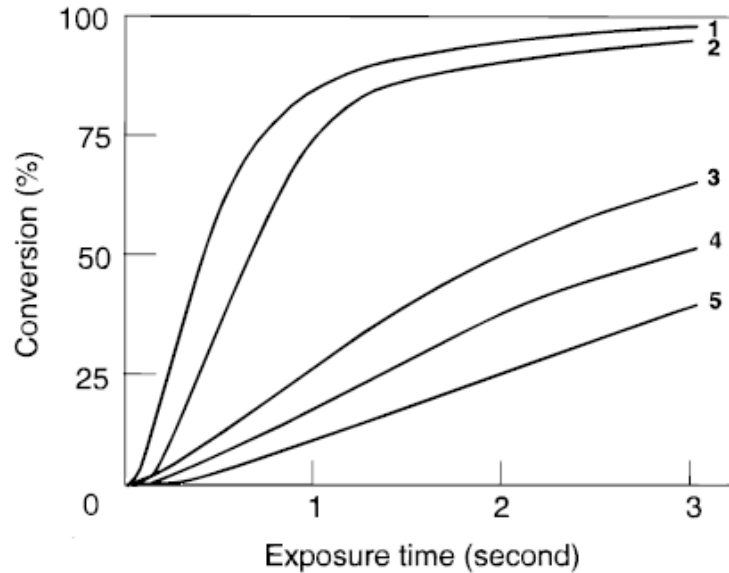


Figure 2.1. Polymerization profiles of five different UVcurable systems (1: acrylate, 2: vinyl ether, 3: cycloepoxide, 4: methacrylate, and 5: glycidyl ether). [12]

which is known to be in the range of electromagnetic radiation with a wavelength from around 400 nm to 4 nm may be used to cure the photo-curable polymers. As the UV light is applied to the photo-curable polymer resins, the photo initiator in the resin will initiate the polymerization that makes oligomers and monomers to be connected to each other and result in crosslinking. This means that UV light can be controlled to polymerize a certain part of photo-curable polymer to make the crosslinking happen locally.

3D objects can be generated if this local crosslinking happens along the printing path continuously to add one layer on top of another making each layer connected to each other. The representative technologies for photo-curable polymers are SLS and SLA which will be discussed in chapter 2.2.4 and 2.2.5 respectively.

Nanocomposites have been developed to obtain improved properties such as mechanical strength and electrical or thermal conductivity. 3D printing of nanocomposite products by integrating nanomaterials and blending into constituent materials has significant potential. For example, a cost effective liquid deposition modelling (LDM) 3D printing technology was developed for manufacturing conductive microstructures from polymer nanocomposites based on PLA and multi-walled carbon nanotubes (MWCNT) as shown in Figure 2.2. [13]

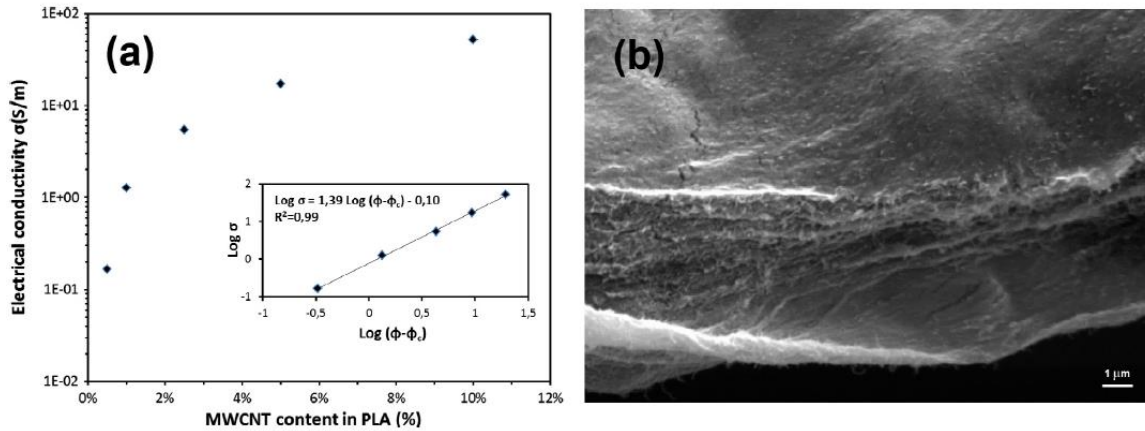


Figure 2.2. a) Electrical conductivity depending on MWCNT content in PLA. The inset is the log–log plot of the electrical conductivity depending on the volume fraction of MWCNTs; b) SEM micrograph of cryo-fractured 3D printed MWCNT/PLA nanocomposites (10 wt% MWCNT in PLA). [13]

Figure 2.2 shows the electrical conductivity depending on MWCNT content in PLA as well as the SEM image of 3D printed nanocomposite with 10 wt% MWCNT in PLA. The aggregation of nanomaterials and light scattering due to the high ratio of nanomaterial is the main challenge for the development of this type of material.

Cellulose materials are widely studied because of merits that cellulose materials are abundant, biodegradable, renewable, and biocompatible. Various cellulose composite materials such as cellulose PLA, cellulose inks with conductive fillers are developed to utilize the unique properties of cellulose. Figure 2.3 shows the mechanism of producing representative nanocellulose materials such as CNC and CNF. These CNC and CNF have been studied for 3D printing to achieve enhanced mechanical properties of printed parts. For example, if the CNC is aligned in the matrix material according to a printing direction during extrusion, it reinforces the tensile strength in the same direction. Figure 2.4 shows that mechanical properties such as tensile strength, elongation, and fracture energy of 3D printed PEGDA hydrogels depend on CNC loading (wt%).

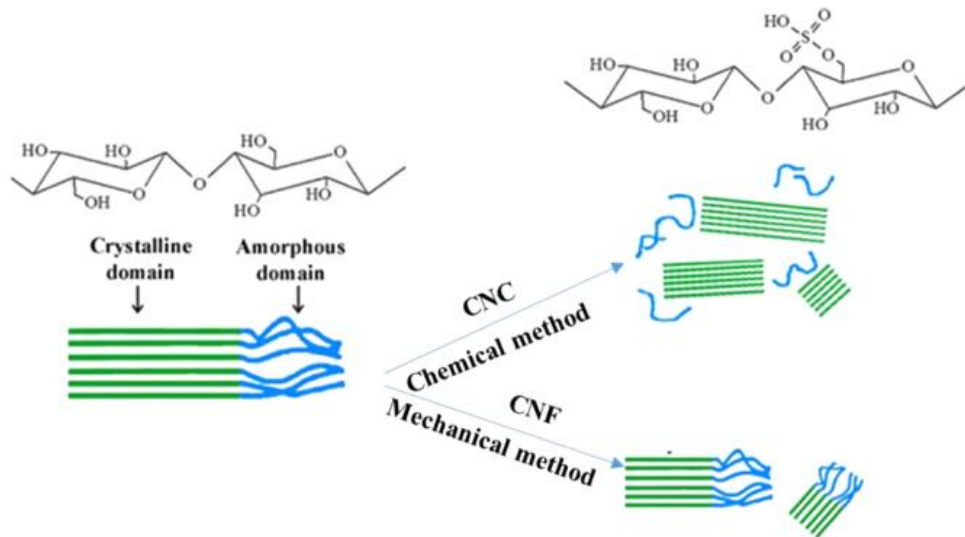


Figure 2.3. The mechanism of producing CNC and CNF from cellulose. [14]

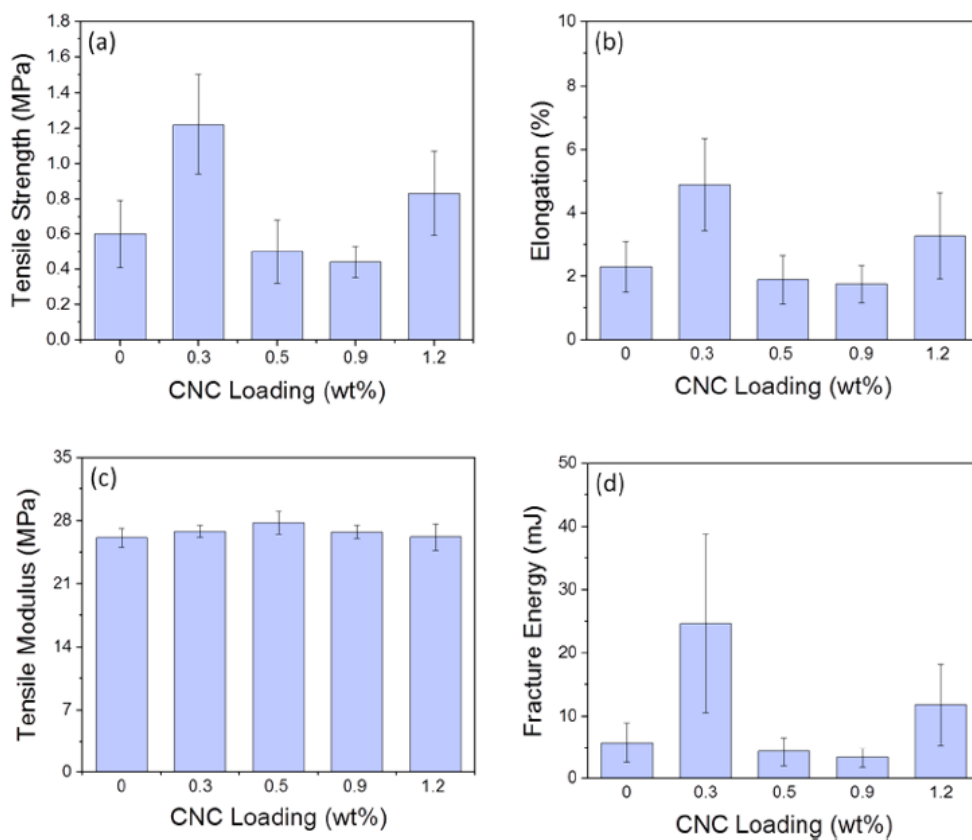


Figure 2.4. Tensile strength, Elongation, Tensile modulus, and Fracture energy for 3D printed PEGDA hydrogels depending on CNC loading. [15]

In this thesis, nanocellulose inks which include conductive fillers such as AgNWs are used to print biodegradable flexible sensors as well as embedded sensors. FDM and extrusion-based 3D printing technologies, DIW which can handle nanocellulose filaments or nanocellulose composite inks are discussed in 2.2.2 and 2.2.3 respectively.

2.1.2. Metals and Alloys

Metal additive manufacturing (AM) is used for research as well as manufacturing parts for the aerospace industry. Metal AM enables manufacturing more complex structures compared to conventional methods. The first step of metal AM process is usually melting metallic powder or filaments using a source of energy such as a laser or an electron beam. The melted metal material form a layer on top of the previous layer, which result as a 3D object. PBF and DED are the most commonly used techniques.

Stainless steel, tool steel, titanium, aluminium alloys, and nickel-based alloys are manufactured by PBF method with high accuracy (± 0.02 mm). However, the low speed of this technology resulted in the limited application only for small sized parts. Ultrafast lasers such as femtosecond lasers are used for alloys and metals such as tungsten and rhenium with higher melting temperature and higher thermal conductivity.

If the metal AM is combined with conventional manufacturing process, it is possible to realize mass production of high quality products. The benefits of metal AM are reduced costs of tooling, achieving complex structure, and eliminating assembly of parts. Figure 2.5 shows an example of fully printed electrolyzer cells which integrates four different parts such as current distributor, bipolar plate, gasket, and liquid/gas diffusion layer (LGDL) into one 3D printed multifunctional part by selective laser melting (SLM).

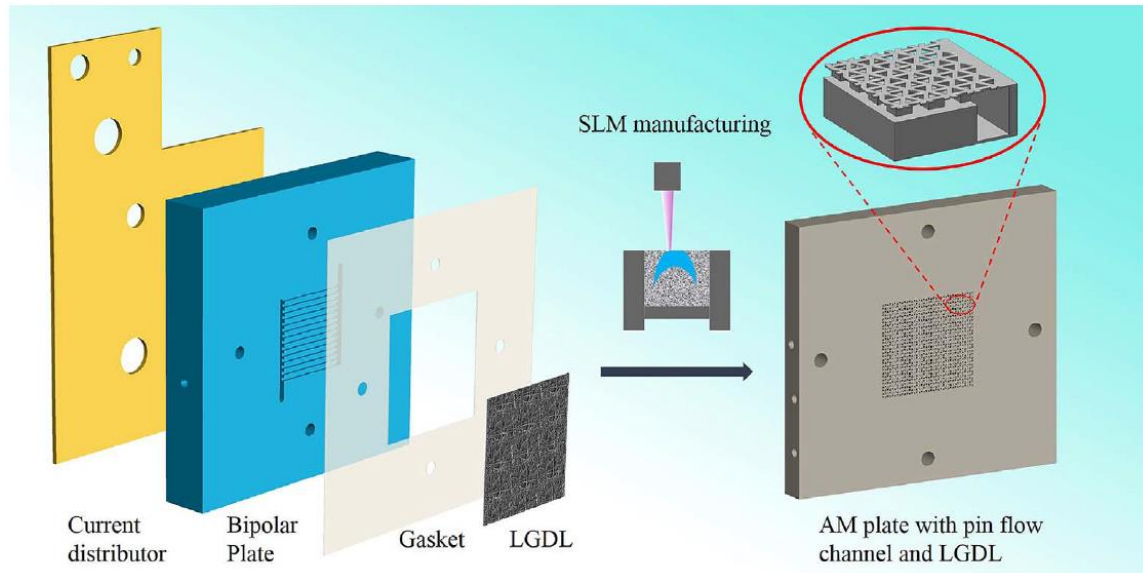


Figure 2.5. Schematic illustration of the integration of current distributor, bipolar plate, gasket, and LGDL into one AM plate via additive manufacturing. [16]

2.1.3. Ceramics

AM is an essential technology for fabrication of advanced ceramic structures such as scaffolds for bones and teeth in medical fields. Main challenges of 3D printing of ceramics are layer-by-layer appearance and limitation of choice of materials. 3D printing of complex ceramic parts which involves 3D printing and sintering is beneficial because the post-processing of ceramic parts after sintering is usually time-consuming and costly. 3D printing technology enables the control of the porosity of lattices. [17] Inkjet, powder bed fusion, paste extrusion, SLA, and SLS are the main methods for 3D printing of ceramic parts. Figure 2.6 shows the additive manufacturing process of polymer-derived ceramics. Ceramifiable monomers such as silicon oxycarbide can be 3D printed, cured to be polymerised by UV light, and sintered at a high temperature to manufacture a complex ceramic lattice.

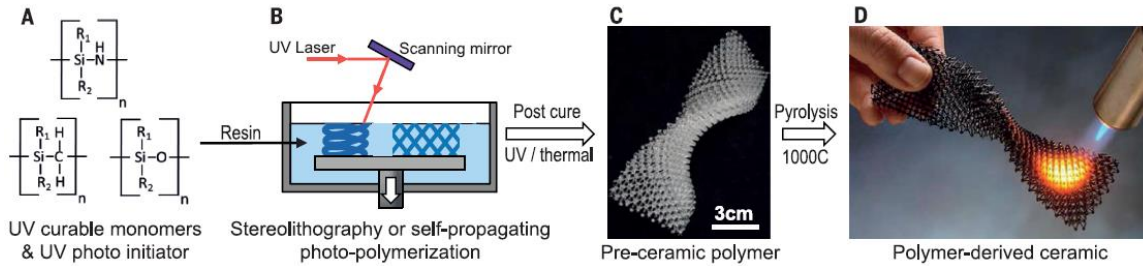


Figure 2.6. Additive manufacturing process of polymer-derived ceramics. a) UV-curable monomers and photo initiator are mixed; b) UV light cures the resin using a SLA 3D printer or a patterned mask; c) A 3D printed pre-ceramic polymer part; d) Polymer-derived ceramic after the pyrolysis. [17]

2.2. 3D Printing Technologies

A 3D printing technology is an additive manufacturing method to fabricate 3D objects from 3D designs. The procedure of 3D printing involves design, slicing, printing, and post processing. The design can be prepared using Computational Aided Design (CAD) software like SolidWorks. After the CAD model is designed, it can be converted into stereo-lithography (STL) file which is usually used in a 3D printing software tools such as Cura, Repetier and KISSlicer. The next step for 3D printing is slicing the STL file which generate a sequence of order using a predefined code like the G-code to prepare the order of printing layer by layer of the designed object. The principle of printing is different depending on 3D printing technologies. Different post processing steps such as removing supports and etching are needed depending on the printing methods.

2.2.1. Overview of 3D Printing Techniques

A 3D printing technology was developed by Charles Hull in 1986 originally as SLA. 3D printing technology has general advantages such as fast prototyping, minimized waste, and manufacturing complex structures. Major techniques of 3D printing such as fused deposition modelling, inkjet printing, SLA, and powder bed fusion are developed according to the requirements of 3D printing as well as properties of printing materials.

Initially, 3D printing was used to generate prototypes because it is fast and cost-effective. Nowadays 3D printing is used to fabricate final products, too. Customized products are challenging for manufacturing because it involves high cost processes such

as rearranging manufacturing processes. 3D printing, by contrast, is very useful for manufacturing customized products with minimum cost. For example, patient-customized products such as prosthetic arms or legs are made cost-effectively through 3D printing in the medical field. 3D printing is also effectively used in construction field. Buildings are 3D printed with less time and man power. For example, WinSun, an architecture company printed a group of houses (200 m² each) in Shanghai, China within a day successfully.

3D printing is getting adapted in manufacturing final products instead of traditional technologies because there are advantages such as fabrication of complex design with higher resolution, materials saving, design flexibility, and product customization.

Figure 2.7 shows 4 main methods of 3D printing which are fused deposition modelling, inkjet printing, SLA, and powder bed fusion.

Following sub chapters of this thesis describes a brief review on 3D printing technologies such as FDM, DIW, PBF, SLA, and DED.

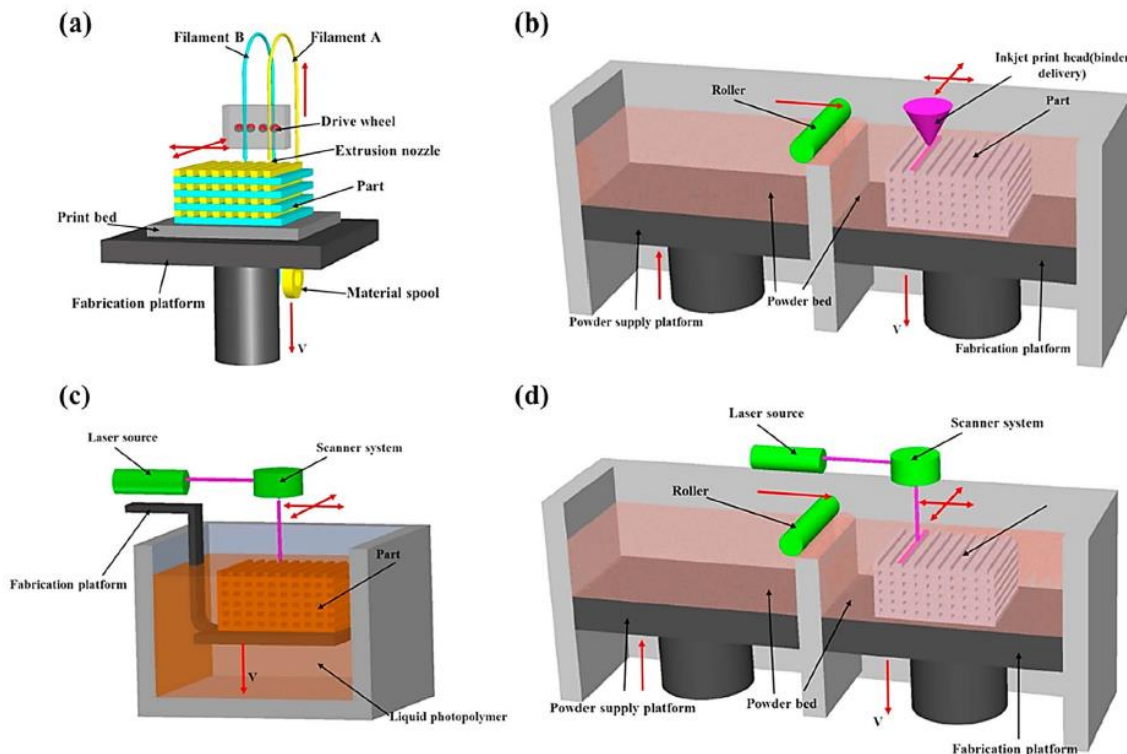


Figure 2.7. Four main methods of additive manufacturing; a) fused deposition modelling; b) inkjet printing; c) SLA; d) powder bed fusion. [18]

2.2.2. Fused Deposition Modeling

The FDM also known as FFF is a simple method that works with thermoplastic polymer filaments. Thanks to the plasticity, a thermoplastic polymer filament heated in an extruder becomes semi-liquid state and extruded through a nozzle and may be deposited to the printing bed or the previous layer to build a 3D object layer by layer and solidified as it is cooled down at room temperature after printing. The temperature of extruder and the printing bed should be optimized to have better results with higher printing quality depending on the properties of materials to be printed. The main parameters that affect the mechanical property of printed objects are layer thickness, width and orientation of filaments. [19] The FFF has advantages such as low cost, simple process, and fast prototyping. It also has drawbacks such as poor surface quality, limitation of choice for thermoplastic materials, and weak mechanical properties. [20]

In this study, the FFF method is used to print a finger body with a Semiflex filament and a fingertip with two kinds of filaments such as ABS and Electrifi, a conductive filament through dual printing.

2.2.3. Direct Ink Writing (DIW)

DIW uses ink material which is not solid type but paste or liquid with comparatively high viscosity. DIW technology can be used for 2D writing as well as 3D writing which uses methods such as laser chemical vapor deposition (LCVD), focused ion beam (FIB), aerosol jet process, laser-induced forward transfer (LIFT), and nozzle dispensing processes which work with a precision pump and a deposition system with a syringe to obtain high resolution for 3D printed objects. [21]

DIW can be also used for eutectic materials. High-operating-temperature direct ink writing (HOT-DIW) was reported as a new process which enables direct patterning of eutectic materials. A molten eutectic ink composed of silver chloride (AgCl) and potassium chloride (KCl) was printed on a glass substrate in air under ambient conditions. This ink solidifies under its eutectic temperature. [22]

DIW combined with a focused laser was also reported, which anneals printed metal parts locally. The nozzle-to-laser separation distance was optimized by modeling the heat transfer in the printed part as a function of printing speed, laser intensity, etc. [23]

The advantage of DIW is the rapid fabrication of materials in complex 3D shapes without spending time and cost for tooling, dies, and lithographic masks. The challenge is to formulate inks which meet requirements for direct writing at the microscale. Viscoelastic inks like colloidal gels or fugitive organic inks experience clogging at the deposition nozzle or require extremely high pressures to make ink flow.

2.2.4. Powder Bed Fusion

SLS can be used for metal and polymer powders to fabricate 3D objects. For the case of metal material, post-processing such as sintering, infiltration, and finishing is necessary to complete the fabrication. For the case of polymer material, local sintering of powder is executed along the designed pattern layer by layer using a laser beam to heat and fuse the polymer powders in the powder bed. The most important factors of this method are powder size distribution and packing which affect the density of the printed objects. [24]

The main advantages of PBF are fine resolution and high quality of printing which are desirable for printing a complex geometry. Advanced applications such as scaffolds for tissue engineering and aerospace may be printed with this method. Another advantage is that the powder bed is working as the support during 3D printing. Thus, removing support material after 3D printing is not necessary. The main drawbacks of this method is the low speed, high cost, and high porosity if the powder is fused with a binder.

2.2.5. Stereo Lithography

SLA uses laser to polymerize photo-curable resin materials and generate designed objects. The objects are printed layer by layer where the current layer is cross-linked to the previous layer printed until the design is fully printed. Other printing methods such as DLP and two-photon polymerization (2PP) work in a similar principle as SLA. The difference between SLA and DLP is that SLA uses the point-source illumination while the DLP uses a pattern of illumination by using a liquid-crystal mask. The speed of printing for DLP is better than SLA. 2PP has its merit of the highest lateral resolution around 100 nm by using squared point-spread function. [25] SLA enables printing high quality parts with a high resolution of 10 micro meter level. [18]

This method can be applied to do 3D printing of complex nanocomposites. [26] However, it is comparatively slow and costly. The choice of materials is limited. The complex kinetics of the reaction and the curing process is one of the drawbacks.

2.2.6. Direct Energy Deposition

DED which is also known as direct metal deposition (DMD), directed light fabrication (DLF), laser solid forming (LSF), or electron beam AM (EBAM) is used for fabrication of super-alloys with high performance. DED uses laser or electron beam which can be directly focused on a small area and used to melt metal powder or wire within a short time. As the source of energy moves the melted part is deposited into the substrate and solidified. [27] DED has no powder bed which is essential for SLM. The metal material is melted with extremely high energy and deposited layer by layer in a similar way as FDM. This method is useful to repair fabricated parts by filing cracks or vacancy which is difficult to achieve in PBF method. This method is usually used for titanium, stainless steel, aluminum as well as alloys for aerospace applications. In general, this method has high speeds and large work envelopes. [28-30] DED reduces the time and cost of manufacturing and gives excellent mechanical properties. However, the accuracy and the surface quality is lower compared to SLS or SLM. [27] Thus, DED is usually used for manufacturing large parts with low complex geometry and repairing large parts like turbine engines.

2.3. 3D Printed Electronics Applications

2.3.1. Overview

3D printing techniques can be applied to produce many different electrical components including the most basic components such as resistors, capacitors, and inductors. More complicated electrical parts such as Light-Emitting Diodes and capacitive sensors can also be 3D printed efficiently. [31, 32] Sensors are among the most intensively studied components because printed electronics have a lot of merits in these applications compared to traditional technologies.

Wearable sensors gained lots of attention because of numerous possible applications in the area of on-body sensing and monitoring. Electrochemical sensors are

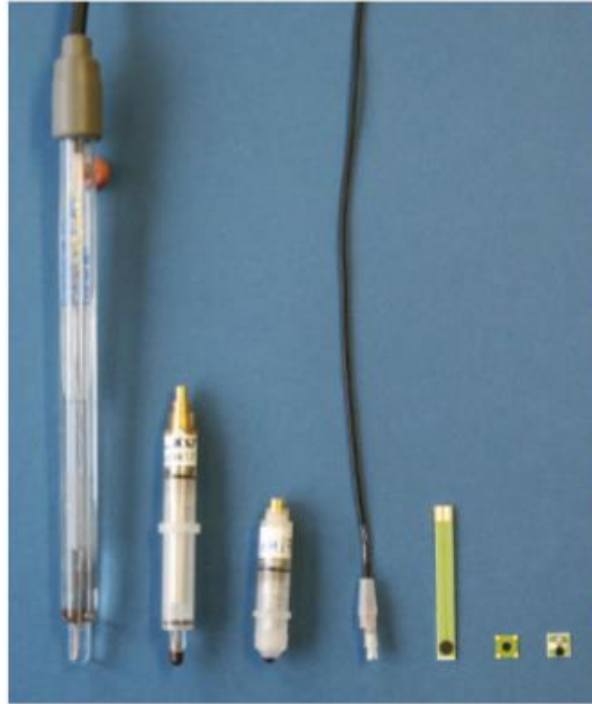


Figure 2.8. Miniaturization of pH sensors. Four conventional potentiometric pH sensors are shown on the left side. The three sensors on the right side are printed. [33]

promising because these may be manufactured as wearable chemical sensors with high performance, compact size, and low cost. As Figure 2.8 shows the miniaturization of potentiometric pH sensors, printing technologies enabled the miniaturization of a wide range of electrochemical sensors. Numerous kinds of wearable electrochemical sensors have been developed for real-time health monitoring of users. Here the focus is on printed electrochemical sensors and wireless communication.

2.3.2. Electro-chemical Sensors

There are various kinds of electrochemical sensors which may be categorized into potentiometric sensor, electrochemical gas sensors, voltammetric sensors, and electrochemical biosensors. [33]

Electrochemical sensors are studied in a wide range of fields from all around the world. Potentiometric sensors are widely studied as one of the major research areas because the detection limits are lowered. These are developed for better robustness and improved detection limits by avoiding the influence of the inner solution. Solid contact

formulations based on conducting polymers are applied to generate long diffusion paths between the inner solution and samples.

A capacitive gas sensor is an attractive platform considering its fabrication and interrogation. However, it shows humidity interference because of the high dielectric constant of water vapor. The selectivity of such sensors can be determined from the thickness of sensing film, which was proved by theory and experiment. The sensitivity to an analyte vanishes when the layer thickness approaches a critical point. For an example, an arrangement of a difference signal from two layers of different thickness demonstrated to be independent of irregular humidity level and showed more stable signal and maintained sensitivity to the analyte.

Ion transfer voltammetry is rapidly developed to be a practical sensor platform to solve fundamental problems. The concept of calibration-free, coulometric ion detectors, and ion transfer voltammetric and pulsed chronopotentiometric sensors for polyionic analytes are the most important advances in this field. Molecularly imprinted polymers are applied as artificial and potentially more durable receptor material in voltammetric sensors. Fouriertransformations are utilized with Voltammetric sensors to extract useful data and enhance selectivity of sensors.

Electrochemical biosensors may show the detection capability which is fast and cost-effective. Novel sensing strategies were widely studied. The enhancement of specificity, sensitivity and response time was reported. [34] In this thesis, the main focus is on the potentiometric sensor which is fabricated with ISME.

Ion Selective Membrane Electrodes (ISME)

ISME is defined as an electroanalytical sensor with a membrane whose potential indicates the activity of the ion to be determined in a solution. ISME has advantages such that, (1) it does not affect the test solution, (2) they are portable, (3) they are suitable both for direct determinations and as sensors for titrations; and (4) they are not expensive. The first SME is originated from the search for biological membrane models which involves a thin glass membrane separating the two electrodes of a galvanic cell that make the electromotive force (EMF) of the cell dependent on hydrogen ion concentration. [35] In this study, ISME with polyvinyl chloride (PVC) membrane is used to detect primary ions

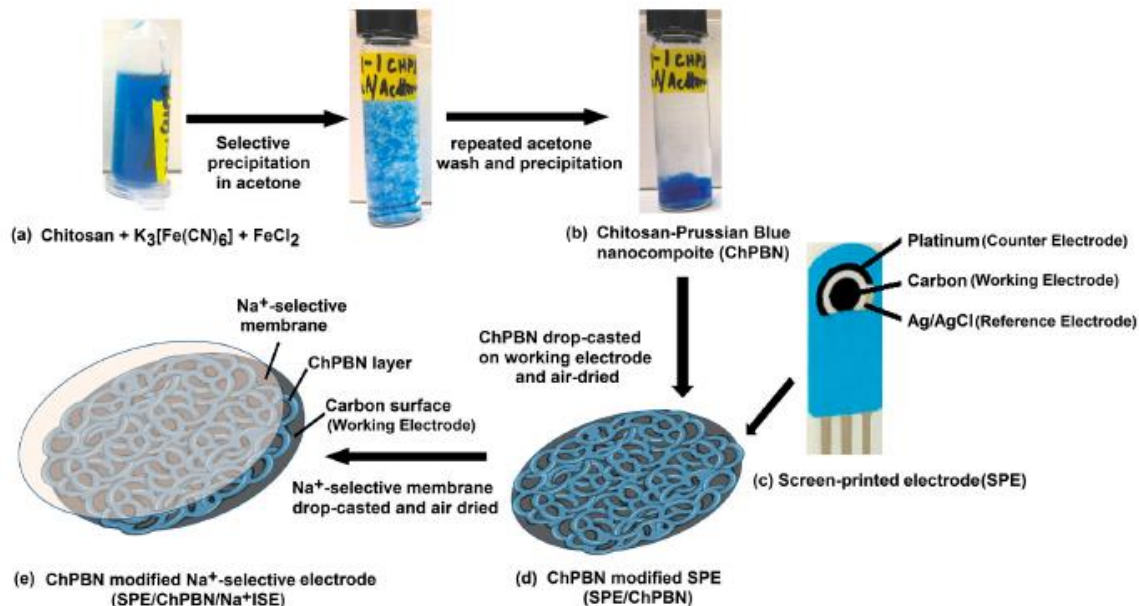


Figure 2.9. Schematics for the preparation of a sodium ion-sensing screen-printed electrode. [36]

such as potassium, calcium, and sodium ions. Figure 2.9 shows an example of a sodium ion-sensing screen-printed electrode.

2.3.3. RF Wireless Sensing

In wearable devices, data acquired from sensors should be transferred to devices to be analyzed. Traditional methods for transferring data is wiring. However, a wireless communication is required nowadays. Here the focus is on LC resonator as well as the RFID system for wireless chemical sensing. These LC resonators and RFID systems can be fabricated by 3D printing.

Inductor Capacitor (LC) Resonator

LC resonator is a closed circuit of an inductor (L) and a capacitor (C). It is called as a resonator because it oscillates at its resonant frequency. A capacitor stores energy in the electric field, and an inductor stores energy in the magnetic field. If an inductor is connected to a capacitor, the energy stored in either inductor or capacitor will make the current flow back and forth between the capacitor and inductor. The energy oscillates back and forth between the capacitor and inductor until the internal resistance consumes the

energy completely. The resonance of the LC resonator is useful in applications in signal processing and wireless communication systems.

An LC sensor may be fabricated using an LC resonator which has a spiral inductor connected with a sensing capacitor. A schematic image of a typical LC sensor is shown in Figure 2.10 (a). Figure 2.10 (b) shows the corresponding equivalent circuit. The capacitance of the capacitor changes when the parameter of interest changes, which shifts the resonant frequency. A readout coil may be used to interrogate the LC sensor wirelessly. If the readout coil is magnetically coupled with the LC sensor, the resonant frequency shift can be detected by measuring the impedance of readout coil.

Figure 2.11 shows that the resonant frequency f_s can be obtained from the maximum of $\text{Re}(Z_{in})$. $f_{\max}(\text{Re})$ is approximately considered as f_s in normal conditions.

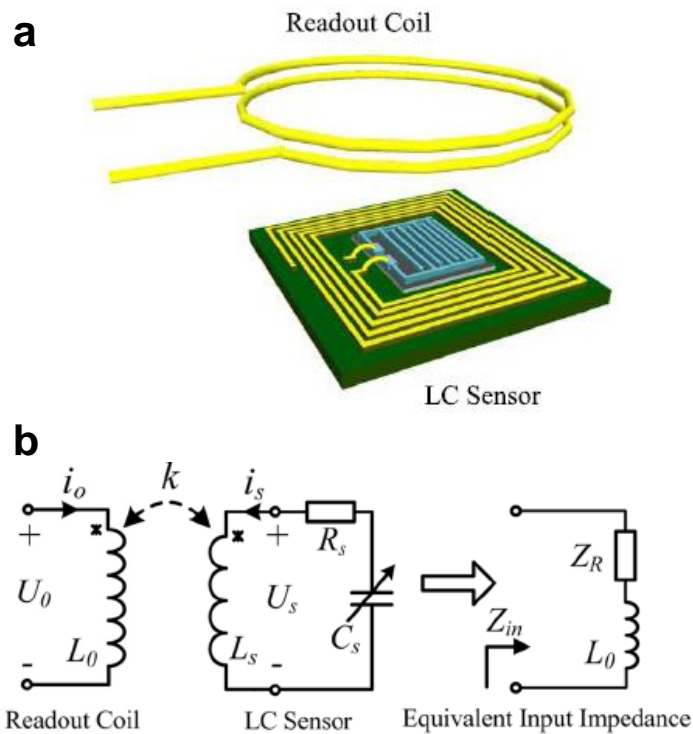


Figure 2.10. a) Schematic representation of an LC sensor interrogating system; b) Equivalent circuit of an LC sensor interrogating system. [37]

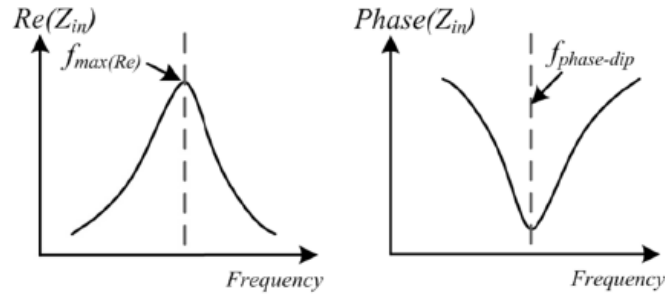


Figure 2.11. Characteristic curve of $Re(Z_{in})$ and $Phase(Z_{in})$. [37]

The ISME-LC Sensor suggested in this study is composed of an ISME and an LC in a series connection. The ISME part of ISME-LC sensor is used for the detection of primary ions. The LC part of ISME-LC sensor is used for wireless communication.

Passive RFID System

An RFID system includes readers (interrogators) and tags (transponders). An RFID system usually includes a smaller number of readers and numerous tags attached to a lot of objects to be detected. A reader communicates with tags and receives the information about objects from the tags attached to them in the range of wireless communication. In a passive RFID system, the passive RFID tag has no power source. Instead, a reader transmits the electromagnetic field (the signal transmitted by the antenna) which powers the internal circuit of a passive RFID tag. A continuous sine wave is transmitted, and reflected signal with the same frequency is received from the tag at the same time. It is important to suppress the leakage signal from the transmitter to the receiver in order to improve sensitivity and readout distance of the system.

The electromagnetic (EM) field has a reactive nature in the near-field region. The electric field and the magnetic field are orthogonal and quasi-static. Most near-field tags work based on the inductive coupling of the coil in the tag and the reader. This follows Faraday's principle of magnetic induction. A current in the coil of a reader generates a magnetic field. This magnetic field makes a current flow in the coil of a tag as shown in Figure 2.12. Examples of near-field tags are shown in Figure 2.13. Two most common carrier frequencies used in near-field coupling tags are 128 kHz (LF) and 13.56 MHz (HF).

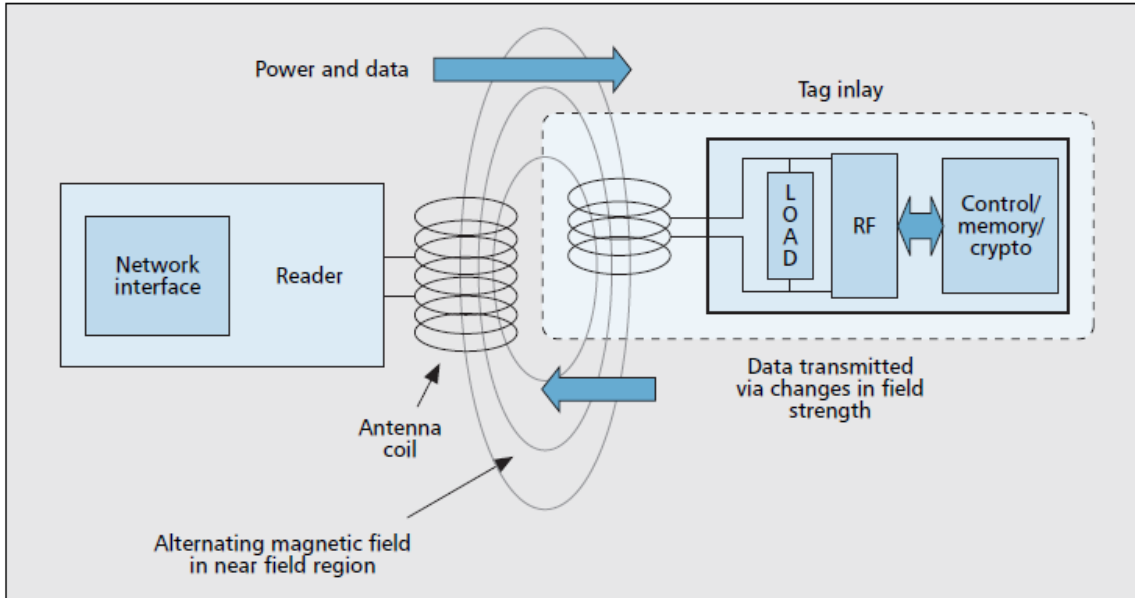


Figure 2.12. Near-field communication using inductive coupling. [38]

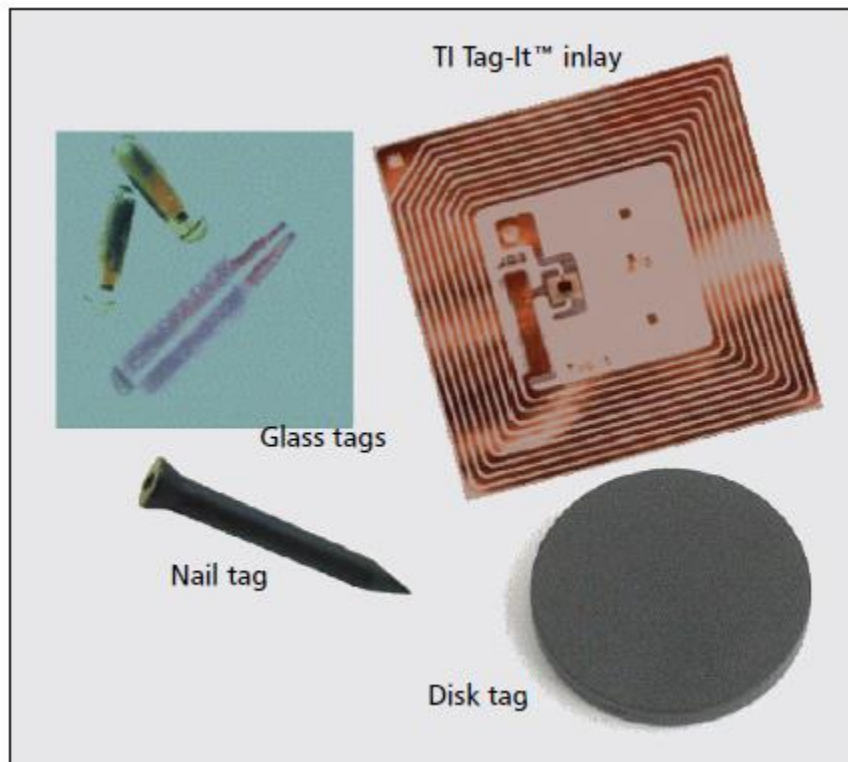


Figure 2.13. Near-field RFID tags for different applications [38]

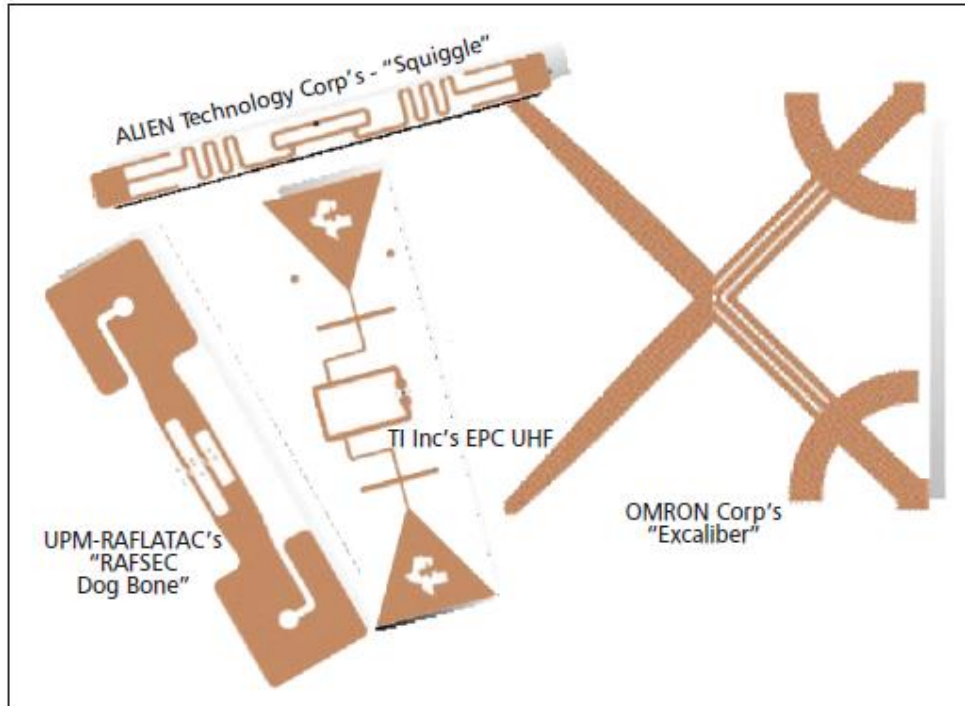


Figure 2.14. Far-field RFID tags for different applications [38]

The EM has a radiative nature in the far-field region. Coupling captures EM energy as a potential difference at the antenna of a tag. The energy incident on the antenna of a tag is partially reflected back due to a mismatch of impedance between the antenna and the load circuit. If the mismatch or the loading on the antenna is changed, the amount of reflected energy is varied. This is called as backscattering. Far-field coupling is used for long-range (5-20 m) RFID. Far-field tags usually operate in the 860-960 MHz ultra-high frequency (UHF) band or in the 2.45 GHz Microwave band. Examples of far-field tags for different applications are shown in Figure 2.14.

Active RFID System

RF wireless communication can be done by using an active system where the active RFID tag has an internal power source such as a battery to power the chip and transmit (or broadcast) signals (interrogation) to the RFID reader autonomously. The reader does not have to provide power for the tag. The available signal strength from the tag to the reader is much lower due to the longer communication distance compared to passive RFID system. Active tags are more expensive and have larger memories and much wider range of operations compared to passive tags in general. Figure 2.15 and

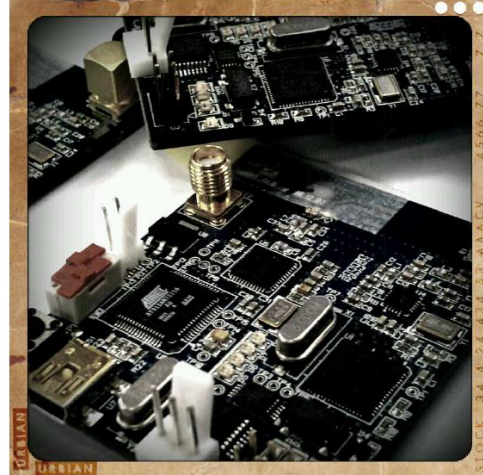
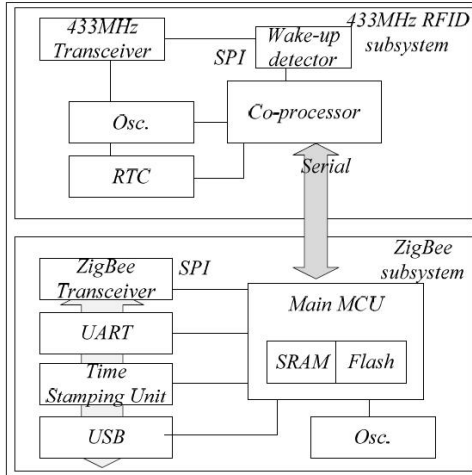


Figure 2.15. Active RFID reader for a large-scale active RFID system [39]

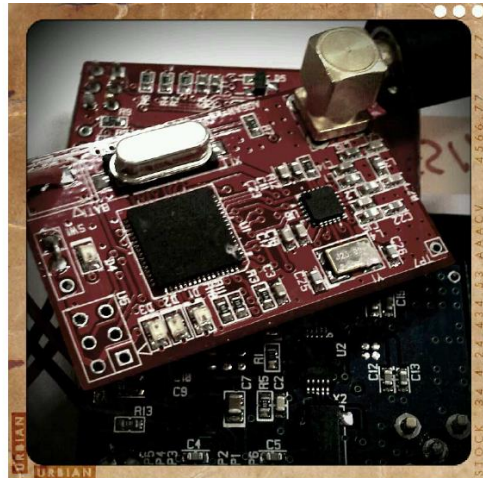
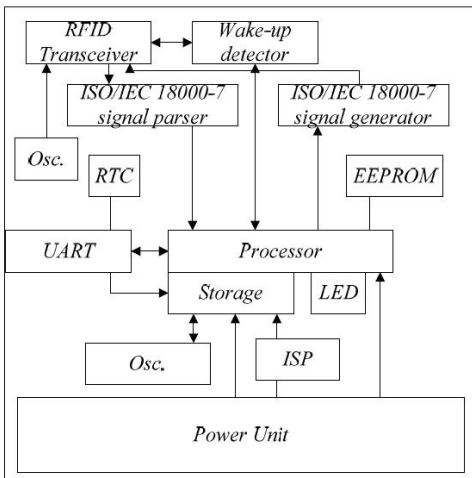


Figure 2.16. Active RFID tag for a large-scale active RFID system [39]

Figure 2.16 show the active RFID reader and the active RFID tag for a large-scale active RFID system.

Chapter 3.

Nozzle-dependent Extrusion-based 3D Printing

This chapter discusses about the nozzle-dependent extrusion-based 3D printing. UV curable polymer material was used as a matrix material together with high aspect ratio silver nanowires as a conductive filler material to make an ink material for extrusion-based 3D printing. A filament based FFF 3D printer was modified by adding an extruder system with syringes and laser diodes at the printing head which will give UV light for curing while printing. Two types of nozzles, a round nozzle with a circular cross section and a flat nozzle with an oval cross section were used to see the different distribution of high aspect ratio silver nanowires in the printed samples and understand the resultant electrical properties. A computer simulation using ANSYS Polyflow was designed and conducted to understand the main cause of the different distribution of high aspect ratio fillers in polymer matrix depending on different shapes of nozzles.

The chapter includes sections derived from the journal paper: **T. Kim, R. Trangkanukulij and W. S. Kim. *Nozzle Shape Guided Filler Orientation in 3D Printed Photo-curable Nanocomposites*. Scientific Reports 8 (2018) 3805.**

3.1. Abstract

This study reports guided orientation of silver nanowires (AgNWs) in extruded patterns with photo-curable 3D printing technology. A printable conductive composite material composed of polymer matrix and silver nanowires shows significantly varied electrical properties depending on the cross-sectional shape of printing nozzles: flat or circular. The composite is designed to have highly conductive AgNWs and a dielectric polymer matrix like photo-curable methacrylate resin. The dielectric permittivity of photo-curable composite resin with 1.6 vol. % of AgNWs printed through a circular nozzle showed 27. However, the same resin showed much lower permittivity with 20 when it is printed with a flat nozzle. The cross-sectional sample morphology shows that AgNWs printed with a circular nozzle are aligned, and AgNWs printed with a flat nozzle are randomly distributed. A computational simulation of paste extrusion with two different nozzle shapes showed clearly different fluidic velocities at the nozzle exit, which

contributes to different fiber orientation in printed samples. A radio frequency identification sensor is fabricated with 3D printed composite using a flat nozzle for the demonstration of AgNW based 3D printed conductor.

3.2. Introduction

Polymer nanocomposites (PNCs) became a promising solution of various applications for their flexibility and processability as well as differentiated mechanical, electrical properties compared with pristine polymers. [40] Recent development of PNCs demonstrates functional properties as well as easy processability required in current electronic device industry. Especially materials with high conductivity or high dielectric permittivity gained great attention. Materials with high conductivity can be applied to fabricate basic electrical parts such as interconnections, inductors, and electrodes of batteries. [41] PNCs with high conductivity can be utilized for 3D printing of electromagnetic interference (EMI) shielding applications which will contribute to miniaturization of portable electronic devices. Materials with high dielectric permittivity can be applied to parts with high capacitance and improved energy storages. [42] PNCs with high dielectric permittivity can be applied to flexible and transparent parts of wearable electronic devices. [43-45]

Various types of PNCs were investigated to prepare a flexible material with high conductivity or high dielectric permittivity. [45-47] Numerous kinds of different polymers such as epoxy, Polyimides (PI), Poly (methyl methacrylate) (PMMA), and Polydimethylsiloxane (PDMS) were used as a matrix in PNCs. Ferroelectric ceramic fillers such as BaTiO₃, PbTiO₃, and TiO₂ or conductive nano wires such as carbon nanotube (CNT) and AgNW were applied to attain enhanced electrical properties. [47-50] But high loads of ceramic fillers, which is required for high dielectric constant, sometimes worsen the mechanical property of the material. [51] PNCs with conductive fillers may exhibit better mechanical flexibility as well as improved electrical properties with lower volume fraction of fillers compared to PNCs with ceramic fillers. A PNC with conductive fillers like AgNWs can be conductive if these conductive nanoscale fillers form a conductive path called as a percolated network which enables the electrons travel through the material. Electrons can move from one conductive filler to another if they are in contact or jump between conductive fillers if they are close to each other, known as tunneling effect. [52] On the other hand, conductive nanoscale fillers and polymer matrix may be arranged in

an ordered structure so that the conductive nanoscale fillers can work as pairs of electrodes of capacitors. And the polymer matrix between nanoscale fillers can work as dielectric to form millions of nanoscale capacitors and exhibit high dielectric properties. [50]

In this study, we chose AgNW as a nanoscale conductive filler to prepare PNCs in order to utilize the high anisotropic character of AgNWs. AgNW is a rod-like anisotropic structure. So its properties may be controlled more effectively by alignment in a matrix material compared to other isotropic nanoscale fillers with a spherical structure. Also, high aspect ratio (100~500) of AgNW induces lower percolation threshold compared to spherical structure. [53] Therefore, AgNW has higher conductivity compared to other fillers like carbon nanotube for highly conductive or highly dielectric applications. [41, 54] Also, the large surface area of AgNW contributes to the efficient improvement of conductive or dielectric property of polymers.

The orientation of fillers in the matrix of nanocomposites affects conductive or dielectric properties as well as mechanical properties. Research has been focused on enhanced mechanical property of nanocomposites with aligned distribution of fillers. [55, 56] The relation between electrical properties such as conductivity or permittivity and the orientation of fillers has been also investigated. [57, 58] If it is possible to use the same compositional materials with the same volume fraction of AgNWs to differentiate electrical properties, then it makes price competitiveness. And if it is possible to control the alignment and orientation of filler distribution, then composites' electrical properties can be tuned by a small part of manufacturing process. For example, changing the nozzle shape of an extruder can give more efficient processability. In this report, it is demonstrated that the electrical properties of composite materials can be tunable through nozzle dependent extrusion 3D printing.

Controlling the filler orientation of PNCs may improve electrical properties. One of the simple and useful techniques to control filler orientation in extrusion printing is to change nozzles' shapes at the end of the extruder. In an extrusion process through nozzles, the converging parts of nozzles will increase and the diverging parts of nozzles will decrease the level of alignment of fillers along the extruded direction. [59] By applying these converging and diverging nozzles in extrusion printing, we can study the relation between the orientation of nanoscale fillers and composites' electrical properties. It is

known that the fabrication process determines material's properties. There are many 3D printing methodologies such as solution casting, filament printing, extrusion printing, and Digital Light Processing (DLP). [50, 60] The extrusion printing is an adequate printing method for nanocomposite materials because it enables us to control filler orientation more easily than other fabrication methods such as solution casting and DLP. This study mainly demonstrates attaining different electrical properties with the nanocomposite, which has same concentration of AgNWs in polymer composites by controlling the orientation of fillers.

A silicone rubber (Ecoflex® 00–30) was utilized as a polymer matrix in a PNC with AgNWs. This PNC was extruded and dried at room temperature. Initially distributed AgNWs inside of polymer sank down to the bottom region of printed sample during the drying process. Because AgNWs are heavier than silicone polymer, they are able to move to the bottom of prints. Therefore, more AgNWs were precipitated at the bottom of a printed sample in case of a PNC with a higher volume fraction of AgNWs. In order to solve this sinking issue, Print & Cure (P&C) system was newly developed to fix AgNWs' distribution inside of polymer matrix using by UV light right after the extrusion. It has been reported with direct writing of carbon nanotube/polymer nanocomposite materials. [61, 62] In P&C system, extruded AgNWs were not sunk down and stayed in the layer where they were printed because methacrylate polymer resin is photo-cured right after printing. Eventually, the cured composite holds AgNWs as printed. Photo-curing is an appropriate technique to keep distribution of AgNWs as printed. The P&C resin, a UV curable resin composed of oligomer (Urethane triacrylate), photo initiator (Phenylbis phosphine oxide), and monomer (Methacrylic acid) is prepared as a matrix which will be cured by UV light with 405 nm in wavelength. The change depending on the extent of alignment of AgNWs was investigated.

Figure 3.1 a shows a schematic of the extrusion of high aspect ratio fillers in a matrix and print-induced distribution of fillers with two kinds of nozzle tips. The left image describes the extrusion from a circular nozzle which has a cylinder shape with a circular cross section. The right image shows the extrusion from a flat nozzle which has a cylinder shape with an ellipse-like flat cross section in the lower part at the end of nozzle. These two images also visualize the assumption that the circular nozzle generates aligned orientation of fillers in a printed sample, and the flat nozzle generates random distribution of fillers after extrusion. This assumption was investigated and verified by experiments as

well as a computational simulation. The actual circular nozzle has a diameter of 840 μm and length of 17 mm. The dimensions of nozzle was chosen to have the best printing results after testing 3 different circular nozzles with diameters of 330 μm and 1360 μm . The flat nozzle has the same length as the circular nozzle with tapered end part of the nozzle: 3 mm. The tapered flat part at the end of the nozzle has an ellipsoidal cross section with the wider and the narrower inner diameters of 1.2 mm and 360 μm respectively.

Figure 3.1 b shows the scheme of P&C extrusion 3D printing system and the real image of its printing head. Four laser diodes give UV light with the wavelength of 405 nm to the printed object and cure it. The focal range of UV light from one diode is about 4 mm in diameter. These diodes are arranged on a line which is parallel to the printing direction along X axis for the most effective curing. It is important to keep diodes as close as possible from the printing surface in order to secure best curing performance because the intensity of the light is dramatically decreased when the distance between diodes and the printing surface is increased.

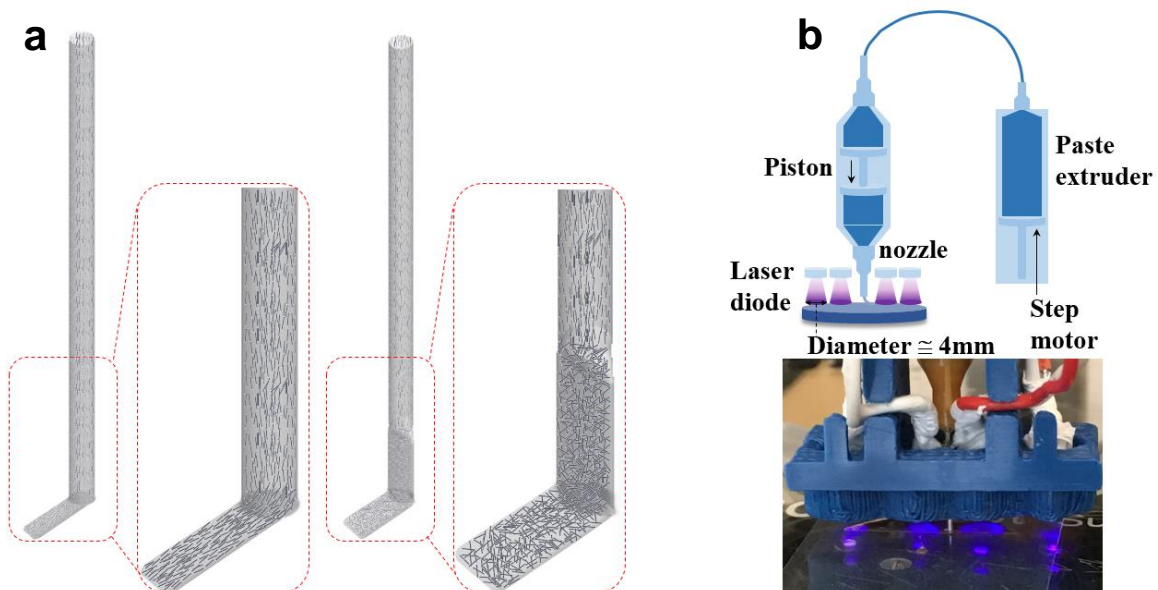


Figure 3.1. Schematics of the extrusion at nozzles and Print & Cure extrusion 3D printing system. a) The scheme of print-induced aligned/random distribution of high aspect ratio fillers of a circular nozzle and a flat nozzle; b) The scheme of Print & Cure extrusion 3D printing system (up) and a close-up image of Print & Cure printing head (bottom).

3.3. Materials and Methods

3.3.1. Photo-curable Extrusion Printing System – Print & Cure

4 Laser diodes were mounted right beside the position of the printing nozzle in the printing head of extrusion printing system to conduct photo-curable extrusion printing. The wavelength of UV light of a diode is 405 nm, and the optical power of a diode is 120 mW. To supply a stable 5 V DC voltage for each diode, drivers for diodes were made with a regulator 7805, two capacitors of 0.33 μ F and 10 μ F, and a resistor of 47 Ω . The power was supplied from the RamBo board of a delta FDM 3D printer (Orion, SeeMeCNC). A paste extrusion system (Discov3ry, Structur3d Printing) was modified to save printing material. Two syringes were connected by a tube which is filled with water in order to transfer the pressure from the primary syringe to the syringe at the extrusion side. The motor of Discov3ry extruder gives pressure to the primary syringe, and the pressure is transferred to the smaller syringe at the extrusion side.

3.3.2. Preparation of AgNW/P&C Resin Printed Samples

AgNWs were prepared by polyol process which make AgNWs with high aspect ratio. The aspect ratio is about 200. The diameter and length of AgNWs are 100 nm and 20 μ m respectively. AgNWs are mixed with P&C resin which is made of an oligomer (Urethane triacrylate), a photo initiator (Phenylbis phosphine oxide), and a monomer (Methacrylic acid). Prepared composite material is mixed thoroughly by a vortex mixer and a magnetic stirrer. To study permittivity of AgNW/P&C resin, 4 samples are printed with two different nozzles and two different AgNW vol. fractions of 0.2% and 1.6%. Assuming that the percolation threshold of AgNWs is around 0.7% volume fraction based on our group's previous research with same AgNWs, [40] concentrations of 0%, 0.2%, and 1.6% volume fraction were chosen in order to compare three different cases such as pristine polymer matrix, PNC with AgNWs of volume fraction under the percolation threshold, and PNC with AgNWs of volume fraction over the percolation threshold.

3.3.3. Simulation of Printing Composite

Fluid models of composite material in a circular and a flat nozzle tips and extrudates are generated with the Solidworks. After fluid models are made, these

geometry files are saved as parasolid format (.x_t). By using these parasolid files, meshes were created in a simulation software, Ansys Workbench (ANSYS, Inc.). After improving mesh quality by CFD (Computational Fluid Dynamics), models are analyzed through polyflow extrusion of the Ansys Workbench to find velocity profile of composite material. According to the mesh quality report, number of total elements of the circular nozzle case is 204222. Among these elements, 96% have quality value greater than 0.8227535. On the other hand, the flat nozzle case has a larger number of total elements, 666816 compared to the circular nozzle case. It's mainly because mesh elements in the shape transition part of the flat nozzle (from cylindrical to flat) should be refined enough to meet the convergence criteria. Among these elements, 86.3% have quality value greater than 0.8177935. 77.0% of elements have skew value less than 0.9295337 which is acceptable.

3.4. Results and Discussion

3.4.1. Filler Extrusion Simulation

In this section, experimental sample morphology is investigated with velocity profile images to prove AgNWs' nozzle dependent extruding distribution in PNCs, then measured dielectric permittivity of printed samples with two types of nozzles are discussed. Finally, randomly distributed AgNWs' conductive printing was demonstrated for the application of RFID tag. The numerical model was solved by ANSYS polyflow using Cross law as the governing equation. The geometry of computational domain was defined and generated as a model composed of two parts which are the fluid in a nozzle and the extrudate for two types of nozzles respectively. Figure 3.2 a, b show the simulation result of extrusion printing with a circular and a flat nozzle. This simulation was designed as a decoupled model. [63] It is assumed that the nanoscale fillers will orient following the flow of polymer matrix because the volume fraction of nanoscale fillers is very low. The extrusion direction is from positive Y to negative Y along the Y axis. A type of generalized Newtonian fluid, Cross model was used for the calculation of simulation.

$$\eta = \frac{\eta_0}{1 + (\lambda\dot{\gamma})^m} \quad (\text{Eq.3.1})$$

where, η_0 = zero-shear-rate viscosity, λ = natural time (inverse of the shear rate at which the fluid changes from Newtonian to power-law behavior), $\dot{\gamma}$ = shear rate, and m = power-

law index. Cross model exhibits shear-thinning behavior, which is dominant viscoelastic behavior of majority of polymers. The degree of dependence of viscosity on shear rate in shear-thinning region can be easily adjusted by changing power-law index. For example, lower power-law index means less dependence of viscosity on shear rate. Zero-shear-rate viscosity was estimated as 1500 cps, because the P&C resin with 1.6 vol. % of AgNWs shows viscosity around 1500 cps. Natural time was set as 0.2 s, which is close to the Newtonian limit where natural time is 0. Though Cross initially proposed that power-law index = $2/3$ was satisfactory for large number of cases, power-law index of this study was set as 0.3 to reflect the lower dependence of viscosity on shear rate of the AgNW P&C resin composite of this study. [64] As it is assumed that there is a uniform velocity profile at the end of extrudate, normal and tangential forces were set to zero.

Since the problem involves a free surface, the domain was divided into two subdomains. Subdomain 1 is the fluid inside of a nozzle. Subdomain 2 is the extrudate outside of a nozzle. Boundaries were defined only at the inlet, nozzle wall, free surface, and outlet (at the end of extrudate), No boundary was defined at the nozzle exit where the fluid in the nozzle interfaces the fluid in the extrudate. Thus, it is not necessary to justify the inaccuracy at the boundary at the nozzle exit. Boundary conditions are as following. At the inlet, volumetric flow rate Q is set as $4 \times 10^{-5} \text{ cm}^3/\text{s}$. The boundary between the nozzle wall and the fluid is set as zero velocity because the fluid is assumed to stick to the wall, which is the no-slip condition. Hence the fluid has no velocity relative to the nozzle wall at this solid-fluid interface. At the boundary of the free surface after nozzle exit, velocity profile is not uniform. The velocity field must be tangential to a free surface, which corresponds to the kinematic condition, $\mathbf{v} \cdot \mathbf{n} = 0$. This condition requires the starting line of the free surface as initial condition. The starting line of the free surface is the intersection of nozzle wall and surface of Extrudate in this study. Lastly, the boundary condition at the flow outlet (the end of extrudate) is zero normal and tangential forces because it is assumed that a uniform velocity profile is reached at the end of the extrudate where no external stress is applied to the extrudate. Whole nozzle and extrudate was simulated without generating symmetry surfaces. Coordinate system is defined as following.

Y axis is at the center of nozzles. Negative Y direction is extrusion direction. X axis and Z axis are perpendicular to Y axis. The center of coordinate system is located at the center of the nozzle exit where $X = Y = Z = 0$ for two types of nozzles. While coupled model is with fluid and filler, decoupled model, a model without the filler is applied in order

to simplify the simulation process. Velocity profile images of the fluid (Figure 3.2 a, b) clearly show higher velocity (red color) at the center of both nozzles. 10 equally spaced lines were defined on XY planes to analyze fluid dynamics more in detail and understand the fiber orientation. In case of the circular nozzle, 10 yellow vertical lines were defined on XY plane which lies on the axis of rotation (a black vertical line) of cylinder shape model of fluid in the nozzle as in Figure 3.2 a. Because of the symmetric structure of a circular nozzle, 10 lines were placed only on the half of the plane where X is positive.

In case of a flat nozzle, 10 equally spaced lines were placed on XY plane which lies on the axis of rotation of cylinder shape part of fluid model and cuts the flat part through the largest diameter of the ellipse-like cross section. Because of the symmetric structure of a flat nozzle, 10 lines were placed only on the half of the plane where X is positive. Fluid velocities were calculated along these 10 lines first. Then the average velocity graphs in Figure 3.2 c–e were attained from these velocity graphs along 10 lines. First of all, equally spaced 10 lines were defined to obtain detailed local velocity data as the velocity profile is not uniform. Then, the average flow velocity was calculated from obtained data along equally spaced 10 lines in order to compare the major difference of fluid flow in two types of nozzles.

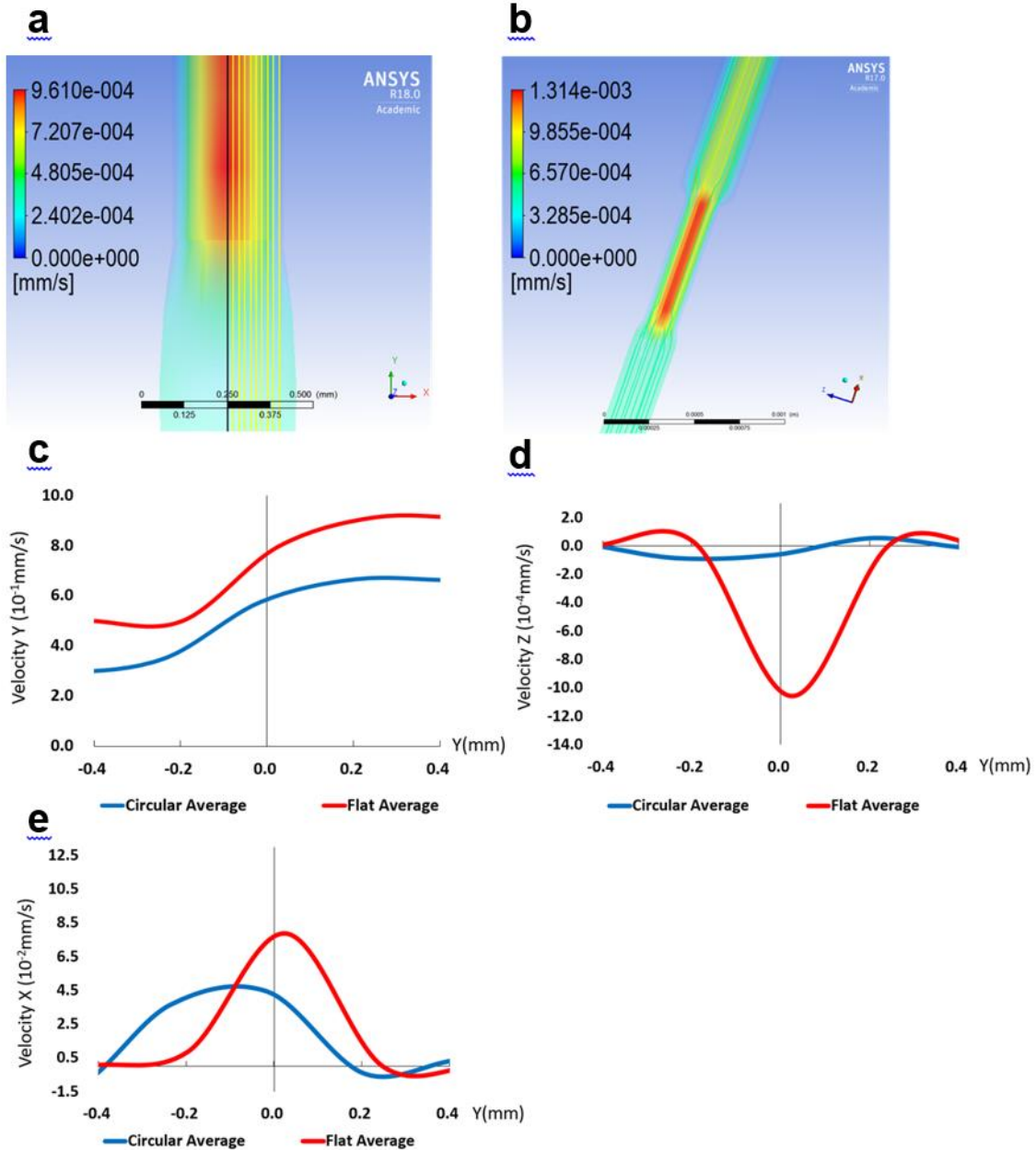


Figure 3.2. Filler extrusion simulation depending on nozzle shapes. Velocity profile of the fluid extruded at a circular nozzle (a) and a flat nozzle (b), and Average Velocity Y, Z, and X (c, d, and e) of fluid around the exit of a circular nozzle and a flat nozzle.

The fiber orientation is estimated by calculation of the second order orientation tensor, A_{33} by using velocity gradients of fluid. The second order orientation tensor is defined as $A_{ij} = \int p_i p_j \psi(p) dp$. Here, p is the unit vector in the direction of primary axis of the fiber. $p_1 = \sin\theta \cos\varphi$, $p_2 = \sin\theta \sin\varphi$, $p_3 = \cos\theta$, θ and φ are angles between coordinate

axis and vector p . The A_{33} component shows the fiber alignment according to the extrusion direction. [60] The velocities and velocity gradients can be calculated along 10 equally spaced lines from CFD results. If A_{33} is close to 1, it means a nearly uniaxial alignment of fibers along the extrusion direction. After the nozzle exit, A_{33} decreases mainly due to the expansion flow and the negative elongation component. [60] In this simulation, calculated A_{33} component varies from 0.94 to 1.00 for a flat nozzle and from 0.97 to 1.00 for a circular nozzle along 10 equally spaced lines around nozzle exits. The difference in calculated A_{33} component is not so enormous, but the fact that A_{33} component shows higher value in case of a circular nozzle reflects that there is more aligned distribution of fillers in case of a circular nozzle. In addition to that, velocity Y, velocity Z, and velocity X represents different extrusion for a circular and a flat nozzles. The aligned and random distribution of fillers depending on nozzle shapes can be understood by investigation of fluid movement. The fluid velocity graphs along equally spaced lines explain how fluid moves. The focus is especially on the nozzle exit because the movement of fluid at the nozzle exit will determine the orientation of fillers in printed samples.

After the nozzle exit ($Y = 0$), for the flat nozzle, filler alignment in Y direction is decreased as Y value is decreased due to two major changes. First, velocity Y (on average) decreases as the Y is decreased from positive to negative value. (The flat nozzle case shows steeper decreasing slope compared to the circular nozzle case). At the nozzle exit, the average of velocity Y of flat nozzle case is about 1.3 times higher than the average velocity Y of circular case (7.7 & 5.8) Second, the absolute value of velocity Z and velocity X show the highest value near the nozzle exit. Fillers will be more likely moving along Z and X axis direction (Expansion flow) [60] instead of aligning along extrusion direction.

On the other hand, a circular nozzle case shows lower absolute value of average velocity Z and average velocity X compared to flat nozzle at the nozzle exit. At the nozzle exit, the average of velocity Z of flat nozzle is about 17.1 times faster than the average of velocity Z of circular nozzle (1.025 & 0.06). The average of velocity X of flat nozzle is about 1.8 times faster than the average velocity X of circular nozzle (7.7 & 4.2). Over all, velocity graphs along 10 lines of the flat nozzle shows larger deviation (the difference between values of each graph from the average graph) compared to velocity graphs along 10 lines of the circular nozzle. This also explains the reason why flat nozzle samples show random distribution of AgNWs while the circular nozzle samples show aligned distribution of AgNWs.

3.4.2. Filler Distribution Morphology

Microscopic images in Figure 3.3 a, b show aligned and random distribution of AgNWs in P&C resin matrix depending on nozzle shapes. The sample printed with a circular nozzle shows aligned distribution of AgNWs (Figure 3.3 a). The sample printed with a flat nozzle shows random distribution of AgNWs (Figure 3.3 b). This was observed similarly in many areas of each sample. And this matches with the simulation result.

Scanning Electron Microscope (SEM) images of the cross section of samples at in Figure 3.3 c, d show the difference between random and aligned AgNW orientation. In the aligned AgNWs sample printed with a circular nozzle, the cross section is showing many dots and smaller number of lines. This happens because AgNWs are aligned along the printing direction, and the cross section is perpendicular to this printing direction. AgNWs aligned to the printing direction will show dot images in cross section, while AgNWs randomly distributed will show line images. Only clear white dots or lines were counted, blurry larger dots or thicker lines were not counted. Thus, majority of AgNWs (~75%) are showing their cross section as dots at the cross section of the sample printed from a circular nozzle. On the other hand, the sample printed with a flat nozzle shows many lines (~75%) and smaller number of dots (~25%) because majority of AgNWs are lying with different angles at the cross section of the sample as a random distribution and are showing their surface of side as lines.

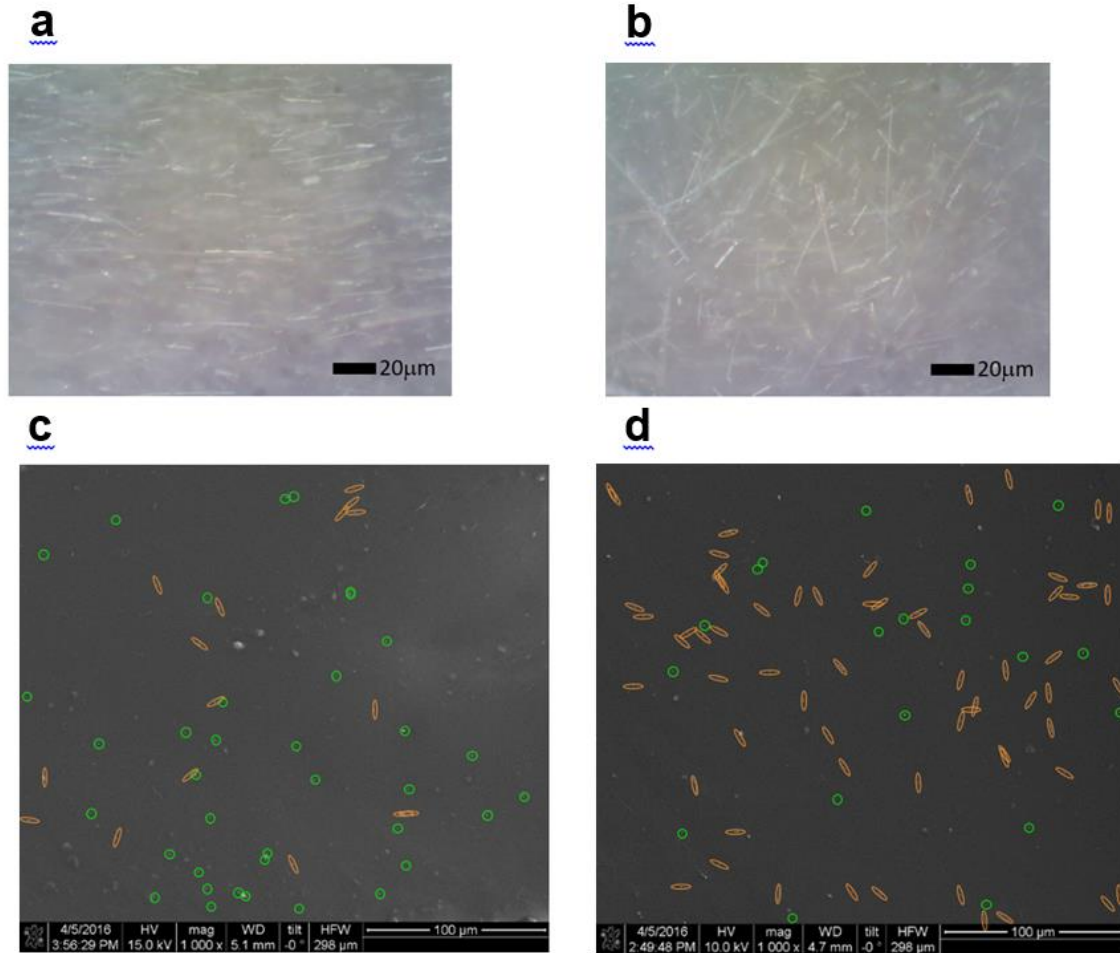


Figure 3.3. Filler distribution morphology. Optical microscope images of Print & Cure samples printed through a circular nozzle (a) and a flat nozzle (b) and SEM images of cross sections of samples printed through a circular nozzle (c) and a flat nozzle (d).

3.4.3. Dielectric Permittivity

Dielectric permittivity was measured by R&S® ZND Vector Network Analyzer (VNA), connected with DAK-12 dielectric measurement system. Figure 3.4 compares the compensated permittivity which is the measured permittivity divided by the weight of each sample in order to compensate the difference of thickness of each sample. The area of each sample is the same. The thickness of a sample is proportional to the volume of a sample. Thus, we assumed there is

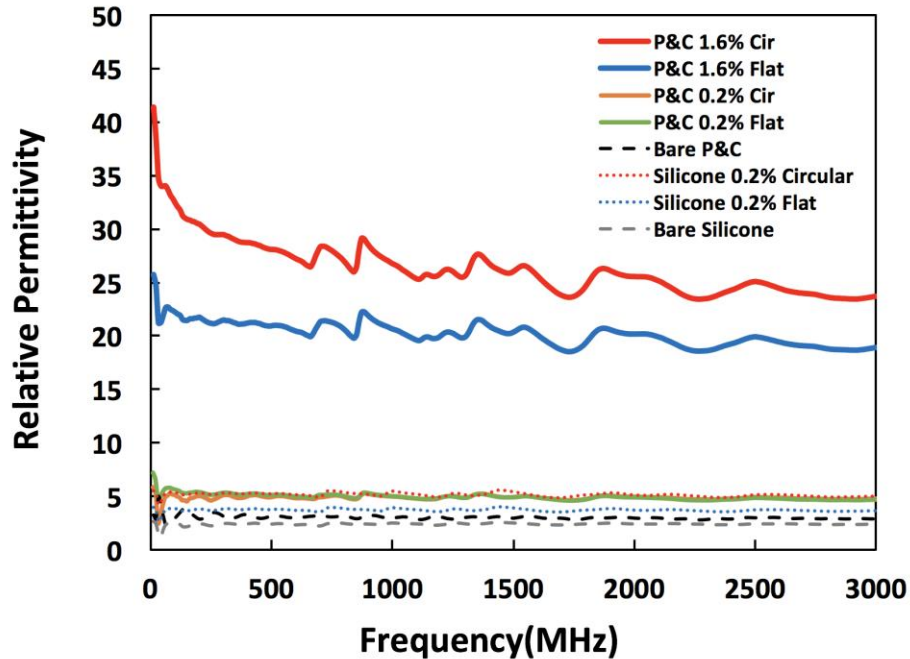


Figure 3.4. Permittivity of Print & Cure (AgNW vol. fraction: 0, 0.2, 1.6 %) and Silicone (AgNW vol. fraction: 0, 0.2 %) samples printed with a circular or a flat nozzle.

a linear relationship between the thickness of samples and permittivity as the linear relationship between AgNW volume fraction and permittivity. [65] The compensated permittivity of each samples was obtained by calculating permittivity of 1 gram sample using measured permittivity, sample weight, and the permittivity of perfect vacuum which is 1 as shown in the following Equation 3.2.

$$\text{Compensated permittivity} = (\text{Measured permittivity} - 1)/(\text{sample weight}) + 1 \quad (\text{Eq.3.2})$$

where, measured permittivity is a relative permittivity ($\epsilon_r = \epsilon/\epsilon_0$). For P&C 0.2% Flat and P&C 0.2% Circular (Cir) cases, there is not so much difference in permittivity. However, P&C 1.6% Cir case has about 30% higher permittivity compared to P&C 1.6% Flat case. This is because Cir has more alignment of AgNWs. These aligned AgNWs will make a lot of couples of two parallel AgNWs which will work like micro capacitors. The permittivity is the amount of charge required to apply 1 unit of electric flux in a medium. Higher dielectric permittivity means higher performance to resist an applied electric field and enables storing more electrical energy in a limited volume, which will be useful for energy storage devices. [42]

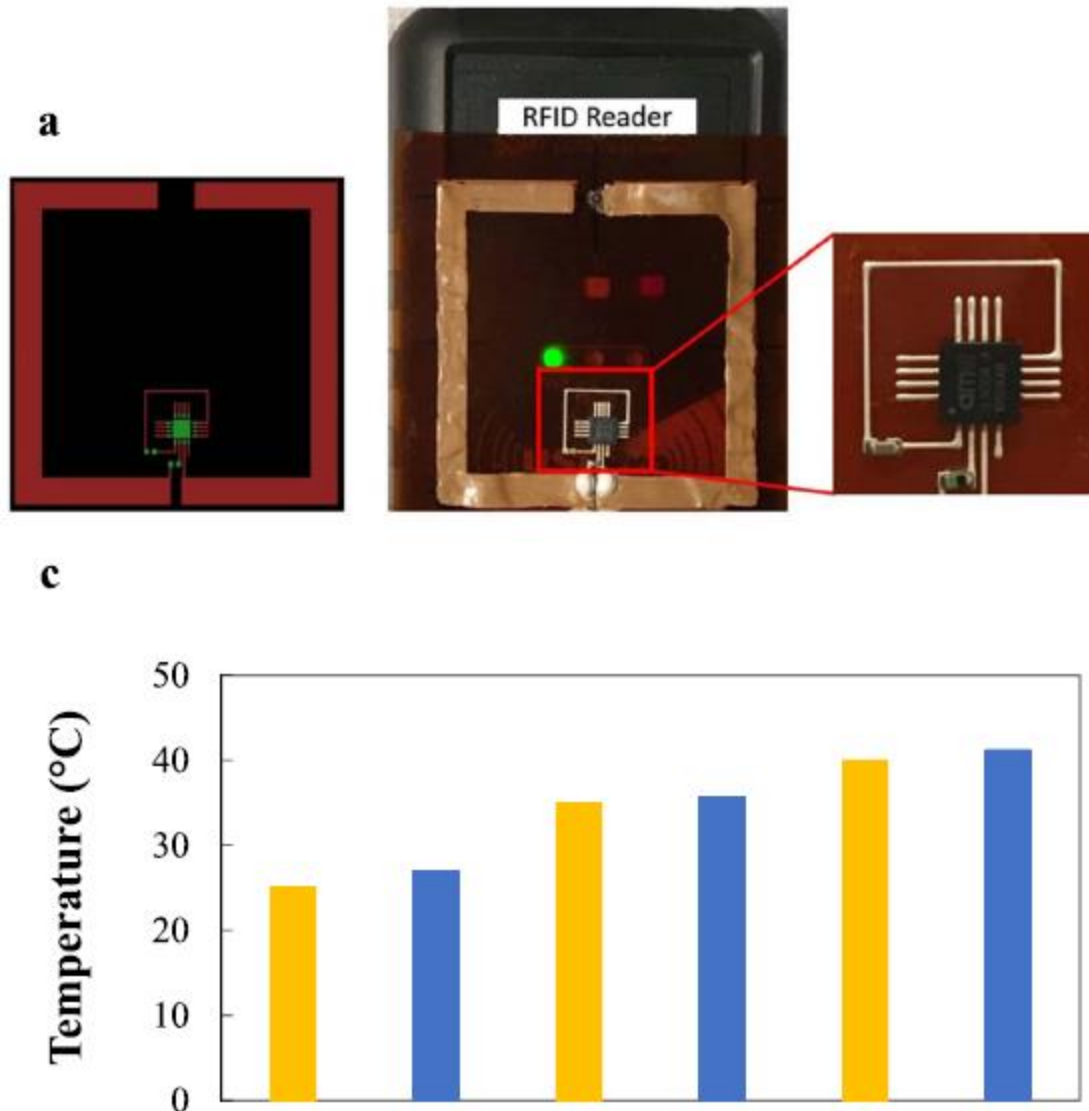


Figure 3.5. The RFID tag design and the detection of a fabricated RFID tag by an RFID reader. a) Design of antenna and circuit layout; b) Detection of the RFID tag consisted of an antenna printed with AgNW (1.5% vol. fraction) and P&C resin composite through a flat nozzle and interconnected with an RFID chip; c) Temperature sensing result from 25 to 40 °C: yellow bars show heater's temperature (25, 35, and 40 °C) and, blue bars show corresponding temperature detected by the RFID tag (26, 35, and 41 °C).

As a demonstration, a passive radio frequency identification (RFID) tag with temperature sensibility was designed to have a circuit and an antenna with a resonant frequency as 910 MHz which is compatible with the RFID reader (Figure 3.5 a). This RFID Antenna was printed by P&C system on a piece of 127 μm Polyimide (PI) film, Kapton® HPP film as shown in Figure 3.5 b. The antenna was printed with the P&C resin with 1.5

vol. % AgNWs through a flat nozzle so that the randomly distributed AgNWs in printed antenna form a conductive network. This antenna was put into an oven for annealing AgNWs at 200 °C for 10 minutes after printing to attain enhanced conductivity. The circuit part of the RFID tag was manufactured by printing an interconnection and soldering components on it. The interconnection was printed by a Printed Circuit Board (PCB) printer, Voltera V1, with an appropriate dimension for 0603 footprint electronic components and an RFID chip because the resolution of V1 printer met the printing requirement. SL900A as an RFID chip, 47 nH SMD inductor, and 2.2 μ F SMD capacitor were soldered on the interconnection. The inductor placed between the RFID chip and antenna makes a large reading range, and the capacitor makes the signal smooth. This RFID tag was well identified by the RFID reader which is compatible with the North American UHF RFID band (902–928 MHz) within the distance up to 1 cm. And the temperature sensing information in the RFID chip was read successfully by the reader at three different temperature levels (Figure 3.5 c).

3.5. Conclusion

In this report, photo-curable 3D printing system has been designed to optimize the printing of a photo-curable nanocomposites composed of photo-curable resin and AgNWs. Specially, the permittivity difference has been observed from 3D printed samples with same concentration of AgNWs when they are 3D printed with different nozzles. The computational study confirms that the extrusion printing with a circular nozzle generates an aligned distribution of fillers, and the extrusion printing with a flat nozzle induces a random distribution of fillers. Utilizing the conductively percolated network realized by printing through a flat nozzle, an RFID antenna is fabricated. The antenna designed to have a resonant frequency as 910 MHz was printed on polyimide substrate for the demonstration of RFID communication and temperature sensing. Therefore, the study on the control of filler orientation in prints ushers the way to control composite material's electrical properties by nozzle shape dependent 3D printing. This can open a new platform of extrusion printing for controlling material's property by design of 3D printing parameters. The effect of nozzle diameters on overall properties will be investigated in future publications by additional experiment and parametric simulation. We expect that nozzle's larger diameter will generate enhanced alignment of AgNWs in case of a circular nozzle and more random distribution of AgNWs with a flat nozzle compared to smaller diameter

nozzles because a larger diameter nozzle will allow more variation of local velocity across the cross section of the nozzle compared to a smaller diameter nozzle.

Chapter 4.

Matrix-dependent Extrusion-based 3D Printing

This chapter is dedicated to the study on the matrix-dependent extrusion-based 3D printing.

The chapter includes sections derived from the journal paper: **T. Kim, and W. S. Kim. 3D Printed Disposable Wireless Ion Sensors with Biocompatible Cellulose Composites. Advanced Electronic Materials 5 (2018) 1800778.**

4.1. Abstract

As the wireless communication technologies are becoming more crucial for internet-of-things (IoT) electronic devices, sensors have also been equipped with wireless data collection. A conventional way to make wireless sensor systems is to develop active sensor devices with silicon-based chip technologies integrated with an amplifier, a battery, a converter, among others. However, it is difficult to generate disposable inexpensive flexible sensors with all these rigid components. Here, 3D printed disposable wireless ion selective sensor systems with unique form factors, high sensitivity, and flexibility are reported. A 3D printable conductive ink is designed and optimized with cellulose nanofibers by addition of silver nanowires for sustainable and eco-friendly sensor applications. Polyimide film which has high surface hydrophobicity is used as a substrate for better resolution of printing. The 3D printed wireless sensor system includes inductor–capacitor circuits, and ion selective membrane electrodes, which can detect quantitative ion concentrations selectively. The change of ion concentrations is detected by measuring the magnitude of S_{11} , reflective coefficient at the resonant frequency of 2.36 GHz using a vector network analyzer. The demonstrated sensitivity is 3.4%/M for ammonium ion (NH_4^+).

4.2. Introduction

Recently, wood-derived cellulose materials which are flexible, recyclable, eco-friendly, and low-cost gain significant attention for sustainable and eco-friendly manufacturing of electronic devices. [66-68] Representative sustainable nanocellulose

materials like cellulose nanofibers (CNFs) and cellulose nanocrystals (CNCs) have been used as primary constituent materials for additive manufacturing. [69-71] Both CNCs and CNFs are mainly utilized as 3D printable ink materials for direct ink writing (DIW) based 3D printing technologies. [72, 73] Specially, conductive cellulose inks which include conductive fillers such as graphene and carbon nanotubes have been also demonstrated as conductive inks for 3D printed electronic devices. [74, 75] Cellulose has been used as substrates as well as the matrix of conductive inks. [76, 77] Some cellulose inks have been investigated for biomedical applications thanks to their biocompatibility. [78]

Recent development for cellulose inks have provided methods to deal with important volume shrinkage resulting from the drying and evaporation of the dispersing solvent. [79] In order to make a reliable 3D printable ink, the relevance of understanding parameters such as the rheological properties (controlling the printability) [80] and the conductivity was evidenced by previous research. [81] Rheological aspects involve a shear-thinning behavior and the existence of a yield stress to enable a proper extrusion and shape fidelity of prior and after 3D printing. [82] The conductivity of the ink can be controlled by the addition of conductive fillers such as silver flakes, silver nanowires (AgNWs) as earlier research suggested. [40, 83]

Among other electrochemical sensor platforms, ion selective membrane sensors have been reported as efficient tools to detect ion analytes selectively from ion mixed solutions such as pH, [84–87] glucose, [88] or urea. [89] Furthermore, by integrating with Field Effect Transistors (FETs), the analyte information is quantitatively analyzed using Ion Selective Field Effect Transistors (ISFETs). [90–92] Recyclable ISFETs based on oxide semiconductors were also studied for sustainability. [93] High selectivity and stability enable ISFETs to be investigated for potential applications in biomedical and environmental fields.

ISFETs are mainly controlled by the generated potential from ion selective electrodes and the generated potential influences the electrical performance of FETs. Therefore, variation of ion concentration is reflected by the fluctuation of drain current, drain voltage, or output voltage. Specially, wireless ion selective sensors are demonstrated to extract remotely ion concentration signals out of analyte solution. Consequently, a great interest was demonstrated over the past years in the fields of real-time monitoring and internet-of-things (IoT) applications. Research was conducted in

integrating novel wireless technologies, such as RFID, [94–98] Bluetooth, [99, 100] Zigbee, [101] or NFC [102] together with electrochemical sensors for wireless analytes information recovery. A conventional approach for wireless sensing with silicon-based chip technology has been already developed. [95]

Here, we report different properties of nanocellulose-based inks composed of AgNWs as conductive fillers and CNFs or CNCs as matrix materials. If the weight ratio of AgNWs in the conductive ink is higher than the percolation threshold, AgNWs make a conductive 3D network. These conductive inks can be used for 3D printing of sensing devices. Also, different 3D printing behaviors of CNF-AgNW ink and CNC-AgNW ink are discussed. 3D printing capability of CNF-AgNW ink on 3D objects is confirmed. This platform will be useful for the analysis of remotely detectable ions. Furthermore, the 3D printed sensor systems developed in this study are light-weight, flexible, disposable, and eco-friendly with highly 3D curvilinear form factors.

4.3. Comparison of Filler Alignment Depending on Matrix Materials

The conductivity of 3D printable inks is strongly dependent on mixing condition between matrix and fillers. To investigate the contribution of matrix material to the percolation of AgNWs and to the formation of a conductive network, CNF-AgNW and CNC-AgNW inks with different AgNW weight ratio are printed on glass slides. The glass slides are considered as appropriate substrates for printing flat and straight lines to access the conductivity by measuring the resistivity of printed inks. Our results demonstrate that AgNWs are randomly distributed in the printed CNF-AgNW ink but aligned in the printed CNC-AgNW ink, as observed in Figure 4.1. The main reason for the different arrangement of AgNWs is attributed to different interaction between nanocellulose materials and AgNWs during the extrusion processes, so the inks can experience different shear stresses within the nozzles. This difference in interaction comes from the differences in dimension, morphology, and entanglement of CNFs and CNCs. Figure 4.1 a describes randomly distributed AgNWs in 3D printed CNFs which maintain the original random distribution after the extrusion

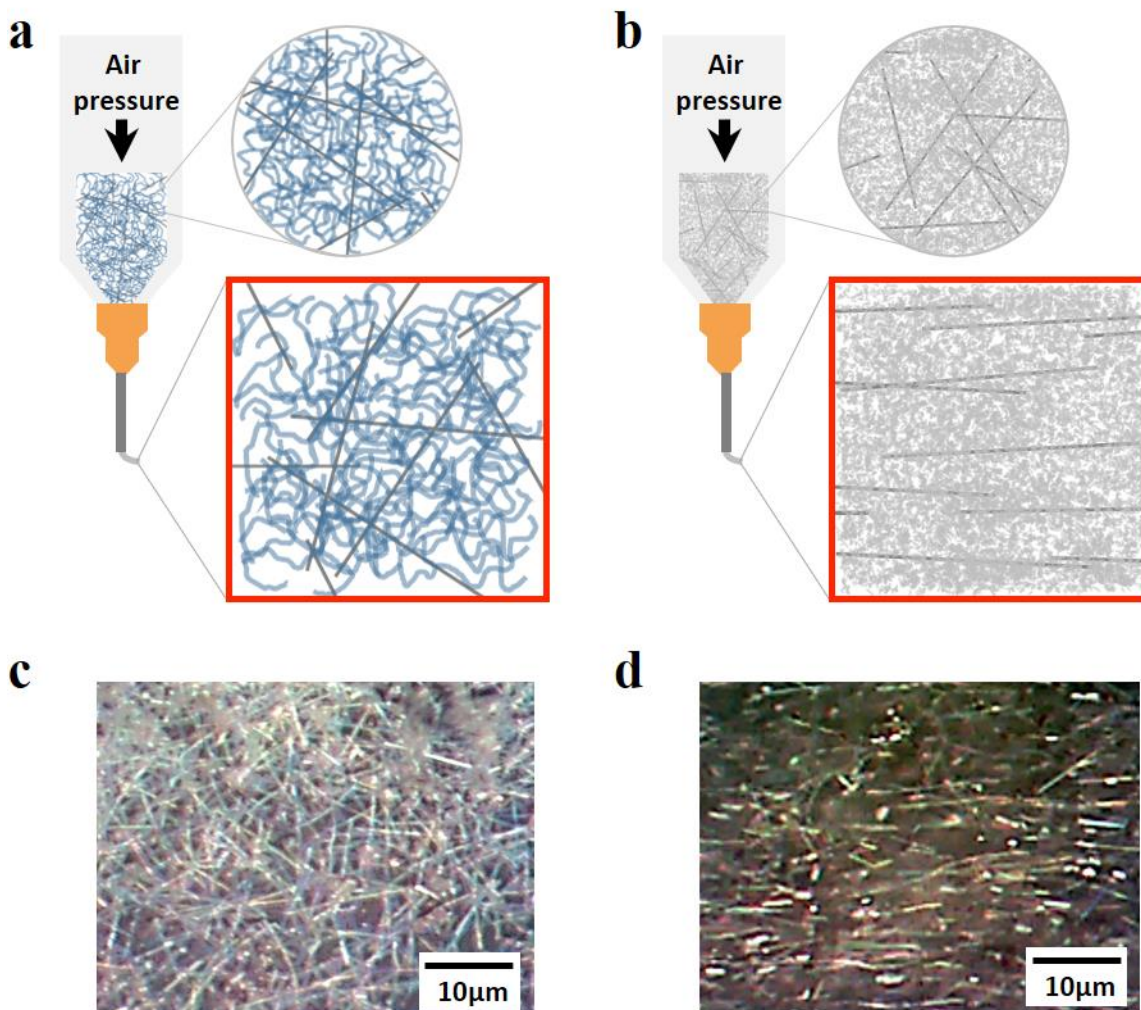


Figure 4.1. Comparison of printed CNF-AgNW ink and CNC-AgNW ink. a) Schematic of printed CNF-AgNW ink; b) Schematic of printed CNC-AgNW ink; c) Microscopic images of printed ink of 36 wt% AgNW in CNF; d) Microscopic images of printed ink of 30 wt% AgNW in CNC.

through a nozzle. The same randomly distributed AgNWs are observed by optical microscopy analysis as shown in Figure 4.1 c. An atomic force microscopy (AFM) image (Figure 4.2 a) also show a rough surface of CNF matrix which was captured from the entangled structure of CNFs. The entangled CNF structure helps AgNWs maintain the random distribution after extrusion for better percolation. On the other hand, Figure 4.1 b shows how randomly distributed AgNWs in CNCs are aligned along the printing direction after the extrusion

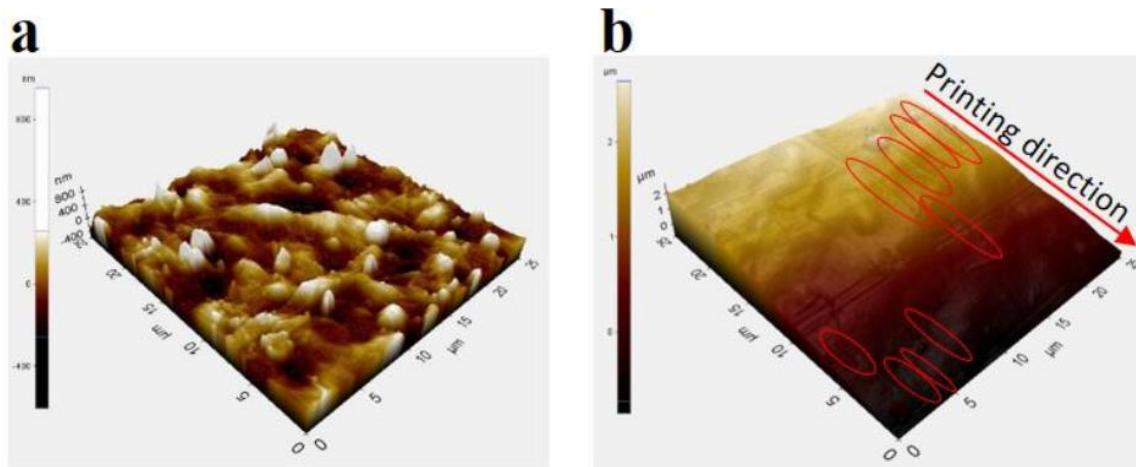


Figure 4.2. Comparison of AFM images of printed cellulose-AgNW inks. a) shows AFM image of printed nanofibril (CNF)-AgNW ink; b) shows AFM image of printed CNC-AgNW ink.

from a nozzle. Figure 4.1 d confirms that CNCs do not contribute to the percolation of AgNWs but induces the alignment of AgNWs along the printing direction. AgNWs prepared for this study have a rod-like shape with a diameter of 55 nm and length of 10 μm on average. [103] CNCs used in this study also have a rodlike shape with a diameter of 6 nm and length of 120 nm. However, the aspect ratio of AgNW (181.8) is 6 times higher than that of CNC (20). [71] On the other hand, the CNFs have a flexible fiber shape like spaghetti noodles with a diameter of 100 nm and a length in the order of 2 μm . In case of 30 wt% AgNWs inks, there are about 15 AgNWs and 1611812 CNCs per 5 picograms of CNC-AgNW ink and about 15 AgNWs and 350 CNFs per 5 picograms of CNF-AgNW ink. It has been reported that the fillers in the shape of rigid rods are aligned along the streamlines of the flow of the polymer matrix. [104] Figure 4.3 shows the central plane of a polymer filament where two-dimensional flow of a fiber take place. It is assumed that the fiber rotates with the center O as the center of rotation. L is the length of the fiber which has two ends marked as A and B. The angle of the fiber with respect to the axis of symmetry is θ as in the Figure 4.3.

The changing velocities of matrix across the cross section of a printing nozzle generate the axial and radial driving force for fiber rotation along the length of the fiber. [104] If it is assumed that the potential for rotation is based on the different values of velocity at both ends of a fiber, the rate of rotation is given as the following equation. [104]

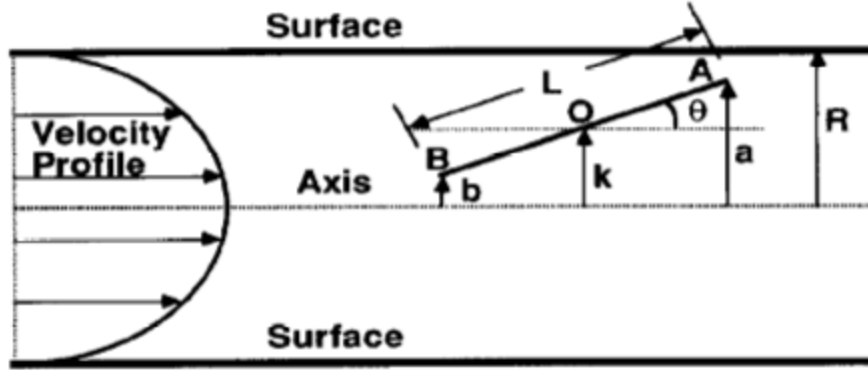


Figure 4.3. Coordinate system in the computation of fiber's radial motion and rotation. [104]

$$\frac{d\theta}{dt} = \beta \frac{\Psi(\theta, t)}{L} \quad (\text{Eq.4.1})$$

where $\Psi(\theta, t)$ is the difference between values of velocity at both ends of a fiber. β is a correction factor for the nonlinear variation of velocities along the length of the fiber and is given as the following equation. β is important only if the aspect ratio L/D of fiber is large. [104]

$$\beta = \frac{1}{2} \ln \left[\left(\frac{L}{D} \right) - 1 \right] \quad (\text{Eq.4.2})$$

A concentrated suspension of rigid fibers in viscous fluid can be aligned by a simple shear flow. [105] As CNCs are in a rodlike shape, a given shear stress aligns CNCs and results in a nematic phase. [106] In concentrated suspensions, CNCs form a liquid crystalline phase with a chiral nematic order. CNCs are reported to be aligned in a similar parallel way. [107, 108] AgNWs, typical anisotropic fillers with high aspect ratio, can be aligned according to the printing direction during the extrusion printing process. [109] The alignment of CNCs along the printing direction in extrusion is also reported. [72] Lots of researches on aligning CNC nanocomposites were done to improve mechanical properties of polymer matrices. AgNWs in CNC matrix can be aligned along the printing direction when the matrix material experiences the shear stress during the extrusion through a nozzle. CNF-AgNW ink and CNC-AgNW ink are subjected to the same shear

stress while they are passing through printing nozzles. However, because of the flexibility of CNFs, the matrix forms an entangled web-like network structure with a higher aspect ratio, acting like a net, restricting the free rotation or movement of AgNWs inside. In contrast, CNCs present a rodlike shape similar to whiskers with a lower aspect ratio, which works like a media where AgNWs rotate and move easily. As shear stress induces CNCs to be aligned along the printing direction, AgNWs are dragged along and tend to align with the flow.

4.4. Resistivity and Printable Properties of CNF-AgNW Ink

The resistivity of 3D printed CNF-AgNW has been demonstrated in Figure 4.4 a. CNF-AgNW ink shows reliable conductivity after 3D printing through nozzle due to its percolation of randomly distributed AgNWs. The resistivity of the optimized CNF-AgNW ink is $9.13 \times 10^{-5} \Omega\text{m}$, which results in conductivity of $1.10 \times 10^4 \text{ S m}^{-1}$ of conductivity as shown in Figure 4.4 a, which is similar to the reported value. [110] Contrarily, the printed ink of 30–36 wt% AgNW in CNC-AgNW did not show any conductivity. For the demonstration of 3D printability of CNF-AgNW ink, a 3D shaped spiral antenna on the surface of a hemisphere is designed as shown in Figure 4.4 b. Figure 4.4 c shows the printed 3D antenna on a 3D hemisphere which has a diameter of 42.5 mm. Figure 4.4 d shows the resonant frequency of the 3D antenna at 2.48 GHz where the magnitude of S_{11} shows the minimum, and the real part of impedance, $\text{Re}(Z)$ shows the maximum. [111] The printability of CNF-AgNW ink is confirmed by measurement of storage modulus (G'), loss modulus (G''), and viscosity. The measurement of G' and G'' shows high G' and elastic behavior at low shear stress ($G' > G''$) (Figure 4.5 a). This condition enables better printability through a rapid solidification after printing. [72, 112] A shear-thinning behavior is observed from Figure 4.5 b where the viscosity decreases by several orders of magnitude as the shear rate increases from 9.93×10^{-4} to 1000 s^{-1} .

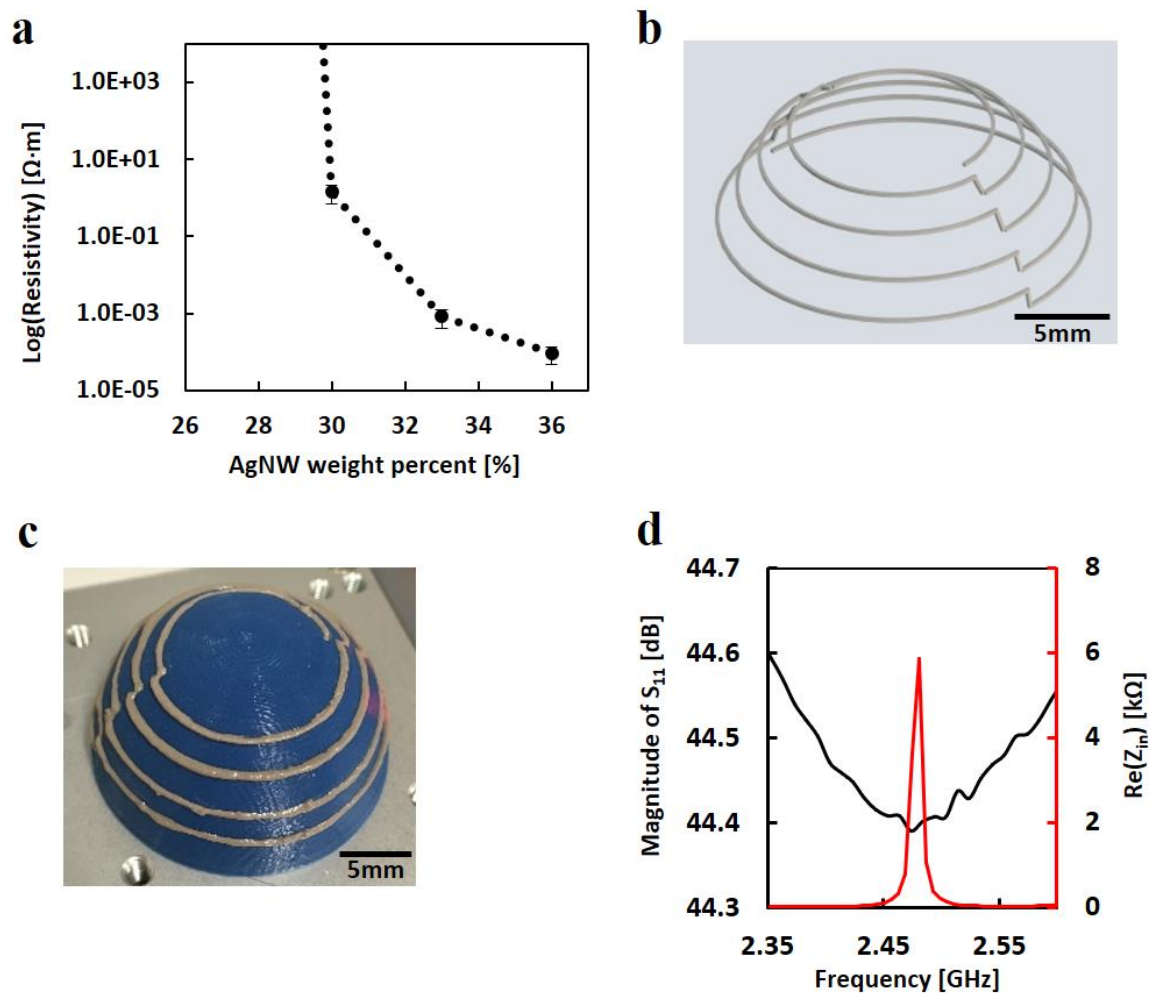


Figure 4.4. Resistivity and printable properties of CNF-AgNW ink. a) Resistivity of CNF-AgNW ink; b) 3D printing schematics of an antenna; c) 3D printed antenna on a hemisphere; d) Corresponding graphs of magnitude of reflection coefficient S_{11} (black) and the real part of input impedance depending on frequency (red).

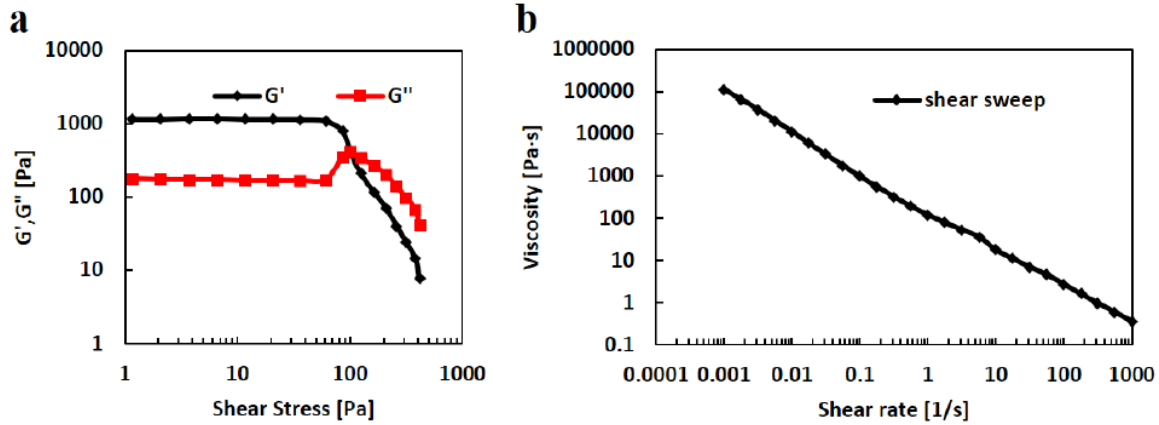


Figure 4.5. The rheological properties of CNF-AgNW ink. a) shows how storage modulus (G') and loss modulus (G'') of CNF-AgNW ink change when the shear stress changes; b) depicts the relationship between viscosity and shear rate which shows a typical shear thinning behavior.

4.5. Conclusion

The present work reports optimizing and 3D printing of conductive eco-friendly ink where the cellulose materials play an important role as a constituent material which affects the distribution and arrangement of AgNWs a lot. Although both CNC-AgNW and CNF-AgNW based inks show sufficient 3D printability with shear-thinning behavior, 3D printed CNF-AgNW ink shows significantly better conductivity compared to 3D printed CNC-AgNW ink for the same wt% of AgNWs. The main cause of this difference in conductivity is that AgNWs are aligned in 3D printed CNC-AgNW ink and randomly distributed to make a conductive network in 3D printed CNF-AgNW ink, which was confirmed by optical microscopy and AFM results. To develop an LC sensor with a higher sensitivity, improving Q factor is required. Q factor depends on inductance and capacitance of LC which are usually determined by the dimensions and material properties of inductor and capacitor. Even though the modeling of spiral inductors and inter-digitated capacitors (IDCs) are well established, and the inductance and the capacitance may be calculated from established equations using dimensions and material properties of the LC, [35] LC circuits printed with CNF-AgNW ink of this study have very thin layers of inductor and IDC which have thickness in the order of 10 μm . Therefore, a parametric study on the thickness of LC circuits was simulated and investigated by the experiment to understand how to obtain the best performance from 3D printed CNF-AgNW LC sensor. The resistivity of the optimized CNF-AgNW ink is $9.13 \times 10^{-5} \Omega\text{m}$ ($1.10 \times 10^4 \text{ S m}^{-1}$ of conductivity).

Chapter 5.

Wireless Chemical Sensing and Sensing Robot

This chapter describes the wireless chemical sensing and sensing robot manufactured by 3D printing. It includes the design of chemical sensor embedded in a humanoid robot finger and its fabrication, the optimization of the Q factor as well as LC, the wireless ion detection system, and the characterization of ISME-LC sensor.

The chapter includes sections derived from the journal paper: **T. Kim, and W. S. Kim. *3D Printed Disposable Wireless Ion Sensors with Biocompatible Cellulose Composites*. *Advanced Electronic Materials* 5 (2018) 1800778.** and **T. Kim, M. Kaur, W. S. Kim, *Humanoid Robot Actuation Through Precise Chemical Sensing Signals*. *Advanced Materials Technology* accepted (2019).**

5.1. Abstract

As the need for assistive robots is increasing in aging societies, various assistive robot systems including humanoid robots are developed. Humanoid robotic hands are one of the most useful parts to assist humans efficiently. While sensing pressure or temperature from the robotic hands is extensively studied, sensing chemicals is less widely studied despite of the significant importance. Here, we report a unique platform of smartly moving humanoid fingers triggered by chemical sensing. The actuation triggered by chemical sensing from the 3D printed ion selective membrane electrodes (ISME) plus inductor capacitor (LC) sensor is mimicking the process of a human body reaction to external stimulus. The LC part is printed with disposable and eco-friendly cellulose ink material composed of cellulose nanofiber (CNF) and AgNWs dispersed in an eco-friendly solvent, deionized water. R_f intensity change of the LC with ISME of NH_4^+ membrane depends on NH_4^+ ion concentration where R^2 is 0.9576. The smart bending movement of a finger is accomplished by logically programmed actuation through detecting the change of interested ion concentration from 0.01 to 1 M at the ISME sensor and controlling bending angle from 10 to 67 degrees accordingly by utilizing a micro-controller. The overall signal-to-noise (SNR) ratio is over 10. This process may be expanded to applications such as

micro robot systems which receive external stimulus, judge, and execute the actuation to carry out programmed tasks.

5.2. Introduction

As the world population of older adults increases toward 24% by 2030, the need for assistive robots in aging societies is increasing. [114] Assistive robots are developed in various forms such as fixed-based robots, mobile robots like wheelchair robot, prosthetic, exoskeleton, and humanoid robots. [115] These robot systems can assist humans with difficult tasks or work in a dangerous environment autonomously. [116, 117] Robotic systems can also support rehabilitation, [118] assist patients with injuries or paralysis, [119, 120] and help daily life work. [121] These robots will serve people more effectively as their sensing, judging, and performing action become more accurate and reliable. Humanoid robots or robotic hands are used in various fields like service industries, military, agriculture, and medical applications. [122] In an assistive humanoid robot system, a hand is one of the most important parts which can do multiple tasks by holding, pushing, and pulling using multiple fingers. These fingers of a humanoid robot are terminal parts of a robot system where sensors can be applied and utilized in the most efficient way. Usually, human fingers sense physical stimulus like pressure and temperature. And it is not possible to detect chemical materials on human skin. Humans sense taste through the contact of the chemical stimulus on the taste buds of tongues and receptors in noses. Touching chemical materials may be harmful. On the other hand, humanoid robot hands can be designed to detect not only physical stimulus but also chemical stimulus. Humanoid fingers are more appropriate for an assistive humanoid robot to detect chemical stimulus. It is easier for robots to use fingertips to detect chemical ingredients in solutions when they handle these samples with hands because they don't have to move joints a lot to examine samples. Human fingers can do tasks like holding with different patterns of grip [123] and sensing pressure and temperature. Recently, humanoid robot fingers are reported with capabilities to sense various inputs such as tactile pressure [124] and temperature [125] as well as taste [126] to secure necessary information in order to support humans and carry out assigned tasks. A lot of research demonstrated robot fingers which can detect tactile pressure [127-129] and enable grasping objects. However, robot fingers incorporated with chemical sensors have been less widely investigated. Here, we report humanoid fingers with electrochemical sensors which can sense ion concentrations and

move according to the programmed logic. A platform is made for ion sensing on a robotic hand that combines chemical, material, and electronic efforts to detect physiological information and give feedback both by visual motion and wirelessly through an inductor-capacitor (LC) sensor. This platform will be helpful for detecting the ions visually on a real time basis and receiving the data wirelessly for analysis at the same time.

3D printed inductor–capacitor (LC) circuits with CNF-AgNW ink are demonstrated. Finally, we report a wireless sensing solution using the ion-selective inductor–capacitor circuits (IS-LC). This novel technology opens a new platform technology for wireless ion detection quantitatively. This is the first demonstration to develop a wirelessly detectable ion sensor consisted of an ion selective membrane electrode (ISME) [130] integrated with an LC circuit. This is much simpler compared to a battery powered wireless ion sensing system. This LC + ISME circuit is designed to work as an LC sensor, which can be detected at its resonant frequency by the loop antenna connected to the port of vector network analyzer (VNA). [131] The fabricated sensor demonstrated detection of different concentration of ammonium (NH_4^+) ion which is among the most important indicators for the metabolism of human body.

Robot hands can be assembled with several parts such as fingers, palm, skin, and parts for actuation. The more complicated this fabrication process becomes, the more time and cost it takes, which makes robot hand systems expensive, and challenging to realize lots of practical applications. One of the main barriers to the widespread adoption of assistive robots is high cost. [132] The 3D printing method is useful for the incorporation of sensors into a robot system. It is also a beneficial technology to reduce time and cost for fabrication. In this report, we demonstrated a functional robot hand with all structural parts as well as sensors printed using two additive manufacturing methods; 1) Fused Filament Fabrication (FFF), and 2) Direct Ink Writing (DIW). Various materials like flexible, rigid, and conductive filaments as well as conductive pastes were utilized according to the design requirements of each parts of the robotic hand.

This study shows mechanical actuation depending on the result of detecting ion solution concentration selectively and sensitively. A robot with this type of sensing system can detect certain ions from patients' sweat for health monitoring or control sodium level in liquid type of food. Wearable chemical sensors applicable on human skins have been developed. [133-135] However, applications with printed ISME sensors on humanoid

robot fingers have been less studied. The robotic hand we developed has ISME sensors to detect chemical ions and LC circuits for wireless detection. [103, 136] One of the merits of detecting from printed sensors is the on-site real time detection instead of waiting for the experiment result from the lab. The wireless detection of electrochemical sensing is beneficial because of its easier communication and convenience. However, the real time wireless detection of a target material is challenging. We adopted a passive LC sensors for the simple and efficient wireless detection of ions. The advantage of LC sensors is that it enables wireless efficient detection of signals wirelessly without using additional power sources like batteries. [137, 138] Cellulose-based materials were developed and utilized to make eco-friendly flexible sensors. [139, 140] The LC printed with the cellulose-based conductive ink of this study has its merits of being disposable, and eco-friendly. Even the solvent used for both cellulose nanofiber (CNF) and AgNWs to formulate this cellulose AgNW ink is the deionized water which does not generate any harmful byproduct during the drying process after printing. In order to develop optimized LCs for this sensing system, the optimization of inductor was executed based on the study about the inductance of inductors with different shapes. [141] Based on the optimized sensor designs, we prepared three bendable fingers which have ISMEs and LC circuits at the fingertips. The finger body and the fingertip were prepared by dual FFF printing with a rigid and a conductive filaments. An ISME sensor and an LC circuits were printed on two sides of a fingertip. Each of three fingers has different PVC membranes for 3 different target ions such as potassium, calcium, and ammonium ions. These three bendable fingers were assembled on a robot palm which has two fixed fingers. Three fingers were assembled with nylon wires passed through its cores, and the wires were connected to motors for bending. The ISME and 2nd electrodes at the fingertips were wired to a circuit with an Arduino to utilize the change of resistance in the sensor for the actuation of a finger. The novelty of this research is the development of 3D printed ISME LC sensor which enables wireless detection of ion concentration as well as the real time actuation depending on the concentration with simple passive circuit.

We designed a feedback system of a robot hand which includes sensing and bending functions as well as a circuit with a logic. This system is capable to transform the result of chemical sensing into electrical signal and use the signal to trigger mechanical movement accordingly. This robotic hand may be applied to a robot system for monitoring ions in plants where various ion solutions are used. The same system can be expanded

to soft robotics to make robot which determines the direction to move depending on the environmental situation or a micro robot that will travel inside a human body and make a programmed movement to do assigned tasks such as drug releasing at a set condition. [142, 143]

5.3. Results and Discussion

5.3.1. Humanoid Robot Finger's Sensor Design and Fabrication

This study shows smartly moving fingers triggered by chemical sensing. The chemical sensing at the ISME sensor on the bottom side of fingertip will create different levels of resistance in the closed LC circuit depending on applied ion concentrations on ISME. The LC circuit on top of the fingertip will function for wireless detection of different ion concentrations by measuring variation of resonant frequency (R_f) output's intensity from the LC circuits. Figure 5.1 a shows the schematics of overview of experimental wireless sensing setup. When the robot finger is touching the ion solution, the primary ring connected to the VNA port for S_{11} reflection method is communicating with the LC circuit printed on the fingertip. [4] While the radio frequency signal travels through the primary ring, ISME-LC circuit resonates the most and shows a peak of the returned signal at its resonant frequency. The Figure 5.1 b shows two types of 3D printing technologies; 1) DIW extrusion 3D printing, and 2) FFF used to prepare humanoid robot fingers. The detailed fabrication is described in the MATERIALS AND METHODS section.

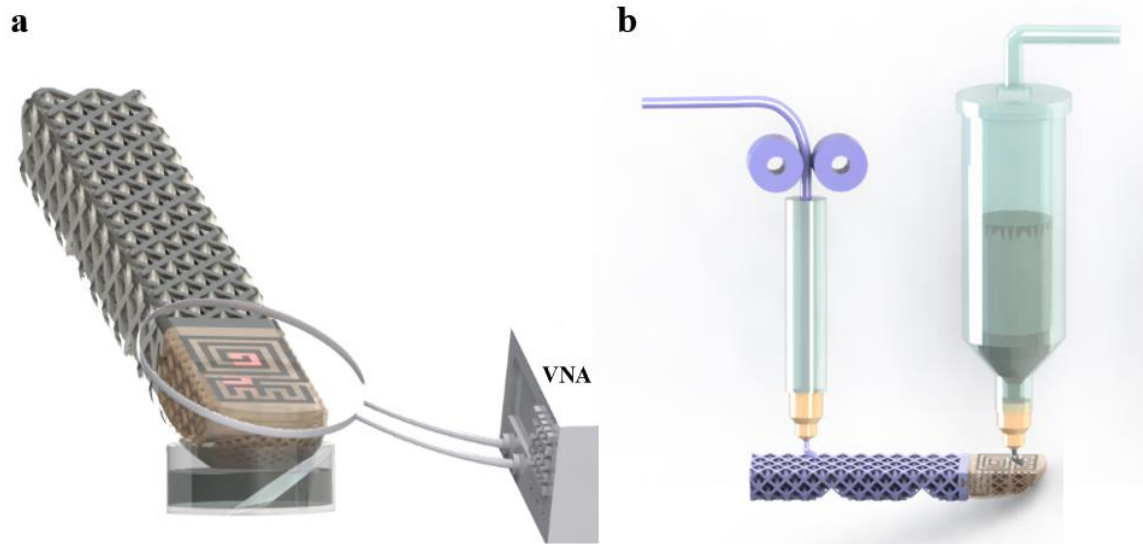


Figure 5.1. Schematics of wireless sensing overview and 3D printing. a) Experimental setup for wireless chemical sensing; b) 3D printing sequence of humanoid finger body by FFF, followed by DIW printing.

5.3.2. The Selection of Optimal LC Circuits

The design of the inductor in the LC circuit was simulated to secure the best performance. Higher inductance value of the inductor enhances the quality (Q) factor of LC and improve the readout distance for the wireless communication as the Q factor of LC sensor is given as the following equation.

$$Q = \frac{1}{R_s} \sqrt{\frac{L_s}{C_s}} \quad (\text{Eq.5.1})$$

where R_s is the resistance, L_s is the inductance, C_s is the capacitance of LC sensor. [37] Figure 5.2 describes the characterization of different inductor design and the simulation result of the chosen ISME-LC circuit when its conductivity between 2 electrodes of the ISME-LC sensor is changed. This is mimicking the resistance changing situation from different ion concentrations applied on the ISME-LC circuits. Figure 5.2 a shows four distinctive 3D LC circuit designs having different 3D inductors with 3 turns, while the design of the IDC is the same. The alphabets assigned to LC designs in Figure 5.2 a mean the shape of inductors (S: Square, O: Octagonal, H:

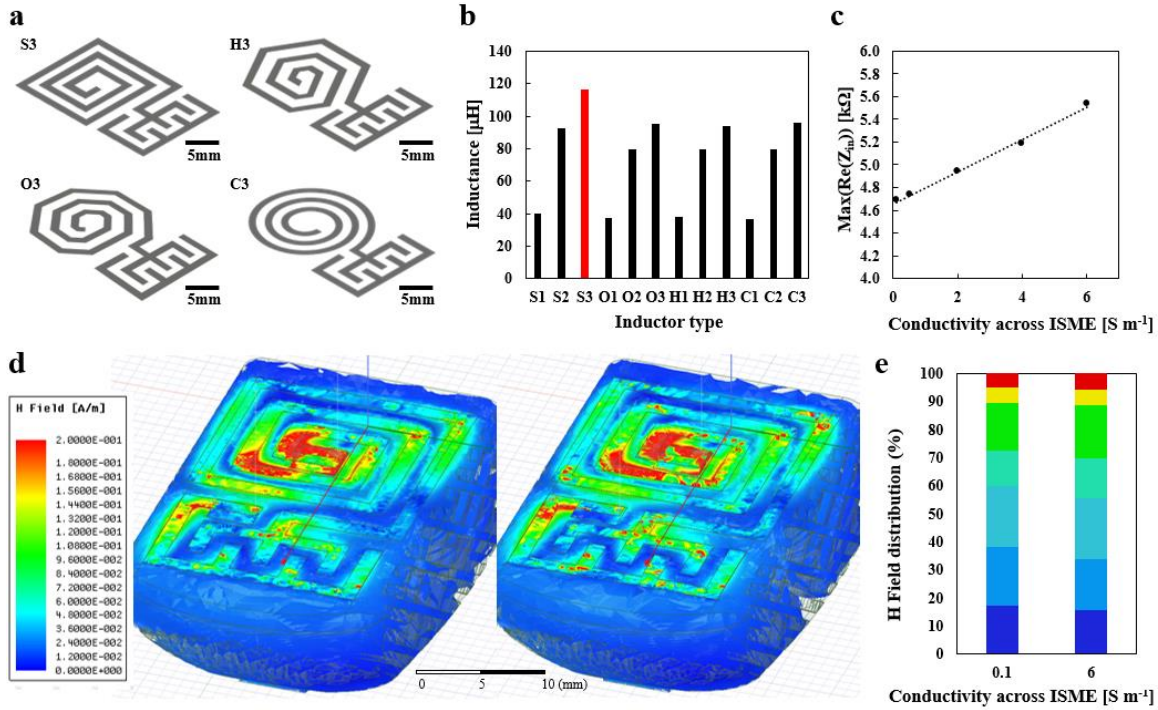


Figure 5.2. Characterization of wireless LC circuits. a) Designs for 3D printing/Wireless characterization of LCs with different inductor shapes (Square, Hexagonal, Octagonal, Circular) with 3 turns; b) Calculated inductance values for 12 types of designs (The alphabet shows the shape of inductors. (S: Square, O: Octagonal, H: Hexagonal, C: Circular) The number means the number of turns.); c) Simulated relation between the conductivity across ISME and maximum real part of input impedance; d) Simulated distribution of H field around the chosen square type LC for the conductivity of 0.1 and 6 S/m across ISME; e) H field distribution comparison of simulation results for the conductivity of 0.1 and 6 S/m across ISME.

Hexagonal, C: Circular). The number next to the alphabet means the number of turns of inductors. For example, S3 means square inductor with 3 turns. The square inductor has the largest inductance value as shown in Figure 5.2 b which shows calculated inductance values for total 12 types of designs, 4 kinds of inductors with 1 to 3 turns of inductors. The calculation of inductance was based on the modified formula [25] which was originally presented for planar spiral inductors. [144] A simple modified version of the original formula is given in the following equation. [137]

$$L_{mw} = K_1 \mu_0 \frac{n^2 d_{avg}}{1 + K_2 \rho} \quad (\text{Eq.5.2})$$

where $d_{avg} = 0.5(d_{out} + d_{in})$, d_{out} is the outer diameter, d_{in} is the inner diameter, ρ is the fill ratio, and $\rho = (d_{out} - d_{in})/(d_{out} + d_{in})$. The coefficients K_1 and K_2 are layout dependent as given in Table 1. μ_0 is the vacuum permeability which is approximately 1.257×10^{-6} N/A².

Table 1. Coefficients for modified wheeler expression.

Layout	K_1	K_2
Square	2.34	2.75
Hexagonal	2.33	3.82
Octagonal	2.25	3.55

Another formula based on current sheet approximation is given as following equation and also gives the same result that the square inductor has the highest inductance value. [145]

$$L_{gmd} = \frac{\mu n^2 d_{avg} c_1}{2} \left(\ln \left(\frac{c_2}{\rho} \right) + c_3 \rho + c_4 \rho^2 \right) \quad (\text{Eq.5.3})$$

where the coefficients c_1 , c_2 , c_3 , and c_4 are layout dependent as given in Table 2.

The Q factor of LC is expected to be around 0.1-0.2 from the equation (1) assuming that the inductance is about 120 μ H, the capacitance is around 4 pF, and the resistance is about 30-50 k Ω for the LC. If the inductance is higher, or the resistance or the capacitance is lower, the Q factor of LC will be higher, and the sensitivity of LC sensor will be also improved.

Table 2. Coefficients for current sheet expression.

Layout	C_1	C_2	C_3	C_4
Square	1.27	2.07	0.18	0.13
Hexagonal	1.09	2.23	0.00	0.17
Octagonal	1.07	2.29	0.00	0.19
Circle	1.00	2.46	0.00	0.20

5.3.3. Simulation of Input Impedance with Different Quality Factor

Figure 5.2 d shows the simulated H field distribution with a fingertip for the conductivity of 0.1 and 6 S/m across two electrodes of the ISME-LC sensor. The H field is stronger around LC for the case of higher conductivity which also shows higher Q factor. Figure 5.2 e shows the image analysis result of H field distribution around LC (Figure 5.2 d), where larger percentage of higher H field is observed for the case of higher conductivity, 6 S m⁻¹ across two electrodes of the ISME-LC sensor. The same fingertip model was used to find the relation between Q factor and conductivity across electrodes of the ISME sensor. It is known that ISME-LC's electrical conductivity is changed, when different ion concentration is detected in the ISME-LC. And the Q factor is related to the maximum of the real part of input impedance, Max(Re(Z_{in})) of an LC sensor as shown in the following equation. [37]

$$Z_{max} = Re(Z_{in})_{max} / f=f_s = 2\pi R_f L_0 k^2 Q \quad (\text{Eq.5.4})$$

where the resonant frequency R_f can be determined by the Max(Re(Z_{in})). The simulation result in Figure 5.2 c shows the linear relationship between Max(Re(Z_{in})) and conductivity across electrodes of the ISME-LC sensor. When the conductivity between two electrodes of ISME-LC sensor is increased, Max(Re(Z_{in})) is also increased. Thus, the increasing conductivity between two electrodes of ISME-LC sensor increases Q factor. ISME-LC sensor with high Q factor shows a sharper peak, and a larger R_f intensity. Q factor is inversely proportional to the resistance of LC sensor as shown in Equation 5.1. There are some reports on the reduction of the bulk resistance of ISME when the primary ion concentration is increased. [113, 114] If the conductivity between two electrodes of ISME-LC sensor increases, the resistance in the closed LC circuit decreases, and the input impedance increases. As a result, the Q factor is increased like the discussion in our previous study. [4] This linear relationship between input impedance and conductivity of ISME electrodes shows that it is possible to detect ion concentration change by monitoring the input impedance change.

5.3.4. Quality Factor Depending on the Thickness of Printed LC

As the sensitivity of a sensor is closely related to the Q factor, a parametric study of LC design to improve the Q factor was done through a simulation and also studied by

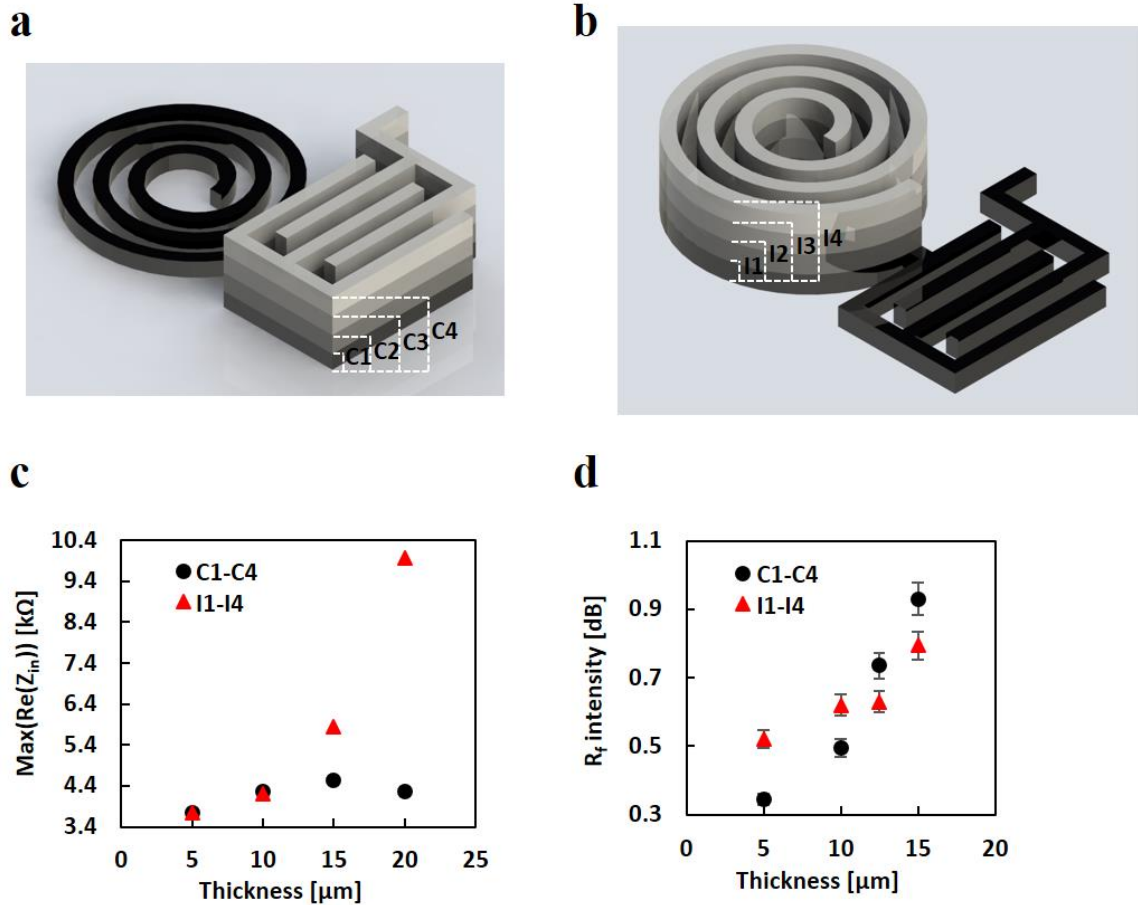


Figure 5.3. Q factor depending on LC thickness. a) Design of LC circuit with different height of IDC; b) Design of LC circuit with different height of inductor; c) Simulation result for the max(re(Z_{in})) depending on the thickness of IDC or inductor; d) Experiment result of resonant frequency intensity depending on the thickness of IDC or inductor.

experiment. Figure 5.3 a, b illustrates the design of LC circuits in series where inductor (I) and capacitor (C) have different heights. The difference of height was obtained by increasing the number of printed layers by 2 from 2 to 8. C₁, C₂, C₃, and C₄ contain IDCs with 2, 4, 6, and 8 printed layers, respectively and contain an inductor of 2 printed layers in common. I₁, I₂, I₃, and I₄ contain inductors with 2, 4, 6, and 8 layers, respectively and contain an IDC of 2 printed layers in common. A total of eight combinations were prepared (Figure 5.4 a). The thickness of layers is exaggerated for better understanding of the structure in Figure 5.3 a, b. Figure 5.3 c is obtained from the simulation on how thickness change the maximum of the real part of input impedance (max(re(Z_{in}))). Here the thickness of LC shows a positive correlation with the max(re(Z_{in}))). Especially, the thickness of spiral inductor shows stronger effect to max(re(Z_{in}))) compared to that of IDC

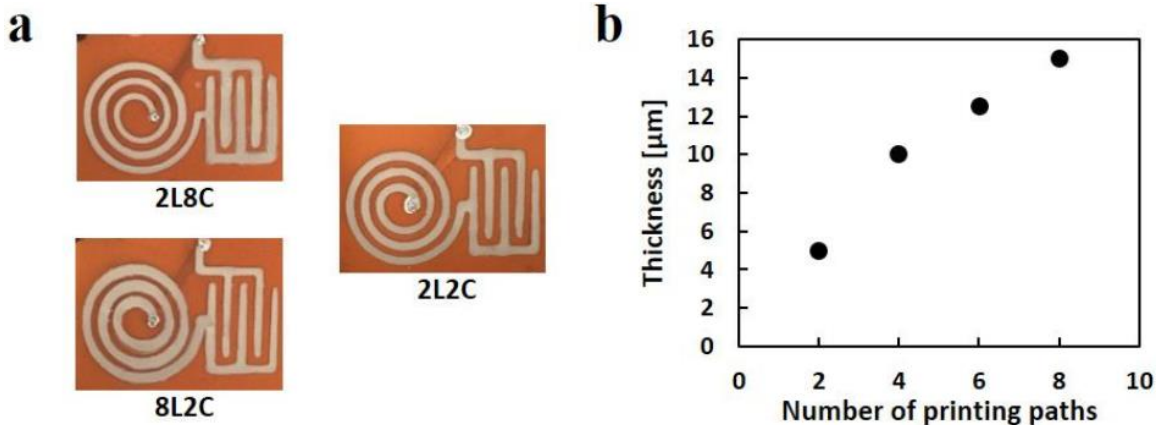


Figure 5.4. 3D printed inductor-capacitor (LC) circuits with different thickness. a) shows three LC samples with different printing paths. For example, 2L8C contains doublelayered inductor and 8-layered capacitor (C4 in Figure 5.3 a). Eight different samples were measured for R_f change in Figure 5.3 d; b) shows the thickness of CNF-AgNW ink depends on the number of printing paths.

at a higher thickness range. The graph in Figure 5.3 d is the experimental result that shows how thickness change the resonant frequency (R_f) intensity at the resonant frequency of LC circuits. R_f intensity is defined as the difference between the magnitude of reflection coefficient S_{11} and a reference value, 45.1 dB at the resonant frequency. As shown in Figure 5.4 b, the thickness of LC was proportional to the number of printing layers up to four layers. However, the thickness of LC was not linearly proportional to the number of printing layers over six layers because the ink is not fully stacking in vertical direction but also expended in horizontal direction. However, this result shows a positive correlation between the thickness of the I or C and R_f intensity. This shows that Q factor of this LC circuit printed with CNF-AgNW ink can be improved by increasing the number of printing layers of either the inductor or the capacitor. Adding layers on top of the previously printed layer increases the probability of making a better conductive percolation network in the final structure. Thus, multilayers of LCs can be applied to IS-LC to improve the sensitivity of electrochemical sensing. The Q factor, Q of LC sensor is given as Equation 5.1.

If the real part of the input impedance, $\text{Re}(Z_{in})$ of an LC sensor has a sharper peak, its Q factor is improved. The maximum of the real part of Z_{in} of an LC sensor can be described as the Equation 5.4.

The resonant frequency R_f can be found from the maximum of $\text{Re}(Z_{in})$ as shown in Equation 5.4. In normal circumstances, $f_{\max}(\text{Re})$ is approximately considered as R_f . [37]

5.3.5. Wireless Ion Detection System

The Q factor of LC sensor depends on the resistance of LC sensor as shown in Equation 5.1. In general, higher Q factor is obtained from a sharper peak which comes with a larger R_f intensity. Thus, the Q factor as well as the R_f intensity will be changed if the resistance of the IS-LC circuit is changed due to the change of ion concentration applied to the ISME. The primary ion of an ion selective membrane is the ion which is targeted to be selectively detected by the membrane, while nonprimary ions are all other interference ions different from the primary ion. An ISME will have a lower resistance if the relevant primary ions are dropped on top of it compared to the cases of nonprimary ions because primary ions can move through the relevant selective membrane while nonprimary ions cannot. Studies on the dependence of resistance of ion selective electrodes on the solution concentration show the bulk resistance of the membranes decreases over the increase of ion concentrations. [112, 113] If the concentration of dropped primary ions on ISME increases, the resistance of ISME decreases. This reduced resistance of ISME decreases the total resistance of IS-LC sensor as the resistance of ISME and LC circuit are in series as shown in the equivalent circuit of Figure 5.5. Then, Q factor which is inversely proportional to the resistance of IS-LC (Equation 5.1) is increased. And eventually, R_f intensity is increased, too. Thus, wireless sensing of the different ion concentrations is possible by measuring R_f intensity change of IS-LC sensor at the resonant frequency. The change of ion concentrations on IS-LC sensor was detected by measuring the magnitude of S_{11} , the reflective coefficient of S_{11} reflection method, at the resonant frequency of ISME + LC circuit (2.36 GHz) using a VNA. While the radio frequency (RF) power from VNA travels through the loop antenna connected to VNA port as shown in Figure 5.7 a, ISME + LC circuit resonates the most at its resonant frequency, and the returned signal of VNA shows a dip at the resonant frequency.

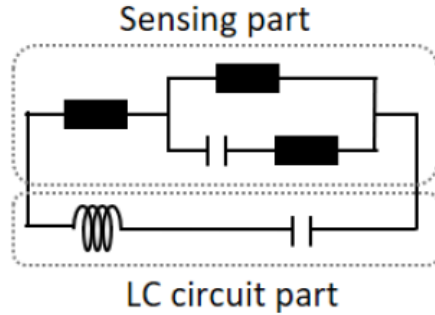


Figure 5.5. The equivalent circuit of sensor system - shows an equivalent circuit of the sensor system consisted of an ion selective membrane electrode (ISME) (sensing part) and inductor-capacitor (LC) circuit part.

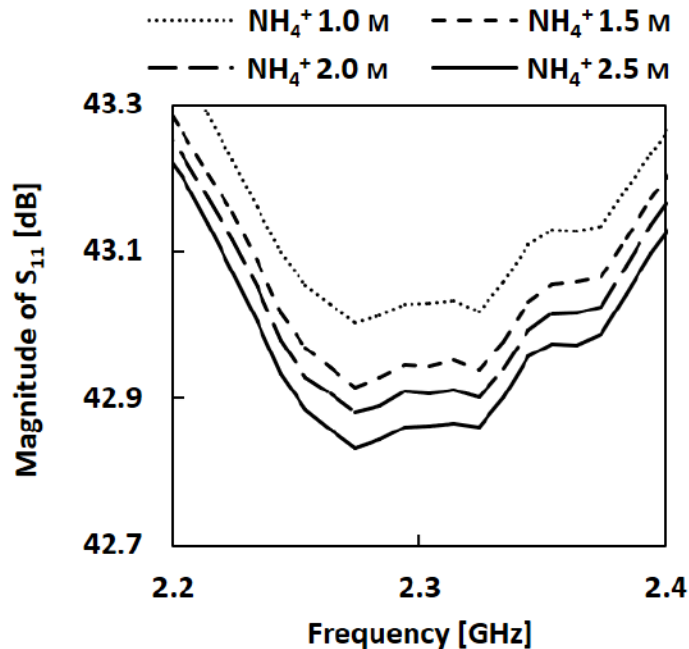


Figure 5.6. Raw data for selectivity of ISME with NH_4^+ membrane - shows the change of magnitude of S_{11} in ISME with NH_4^+ membrane depending on the frequency change for 4 different concentrations of NH_4Cl solution. This graph is the raw data of the selectivity of ISME with NH_4^+ membrane (Figure 5.7).

Figure 5.7 a describes the experimental set up for the wireless detection of ions through the 3D printed IS-LC sensor. The sensor is composed of a 10 μm thick series LC circuit and a sensor of 0.3 mm thick ISME as shown in Figure 5.7 b. For the LC circuit, same layers of LC pattern were printed vertically 4 times, resulting in 10 μm in thickness. This is the maximum printable thickness without lateral margins. Regarding IS part, the thickness was chosen as the single printed layer's thickness of 0.3 mm of 3D printer which

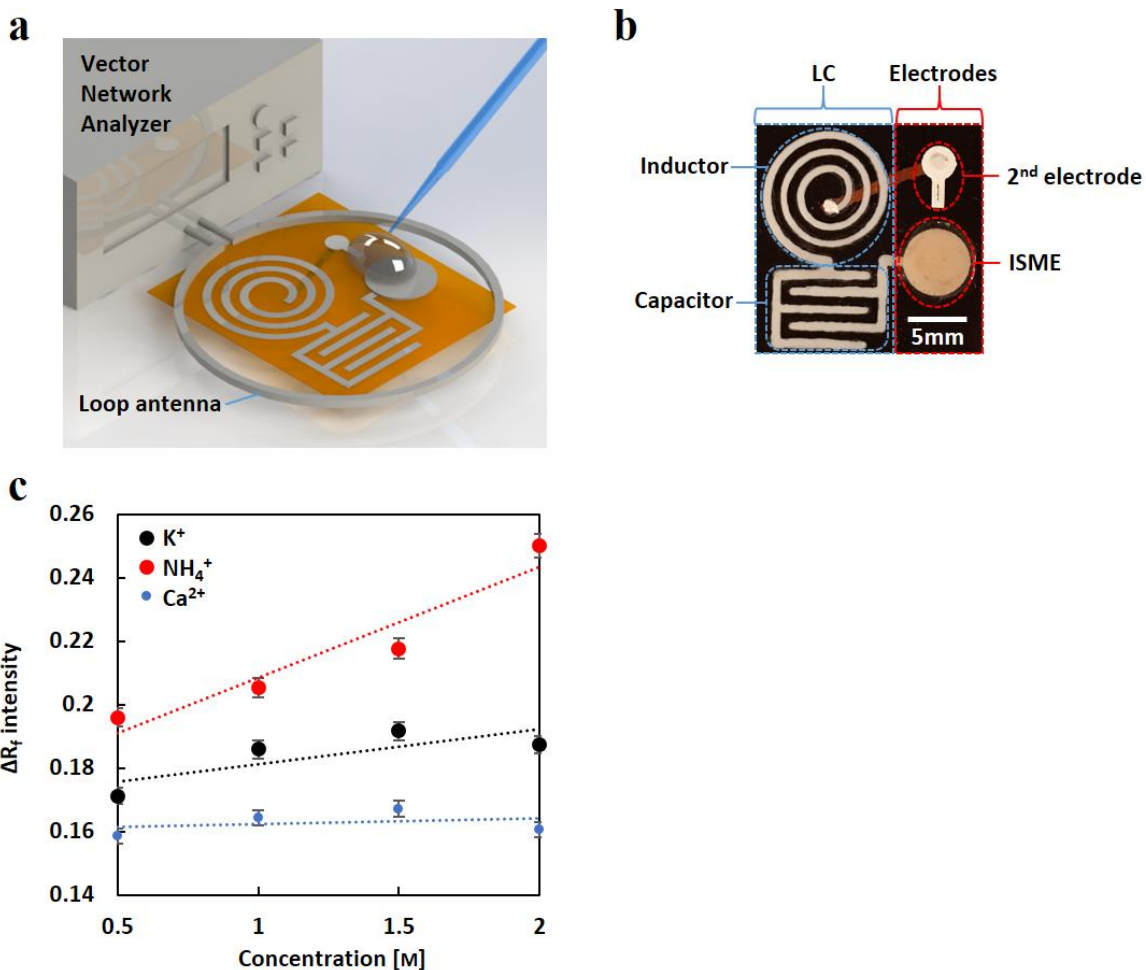


Figure 5.7. Wireless ion detection system. a) Schematic of IS-LC sensor design and loop antenna with VNA; b) Printed sample of IS-LC sensor; c) Experimental result of IS-LC sensor with NH₄⁺ membrane.

showed acceptable conductivity. A VNA was used to find the R_f intensity change depending on different ion concentrations. As the concentration of NH₄⁺, K⁺, and Ca²⁺ ions increases from 0.5 to 2 M, the R_f intensity at the resonant frequency also changes. However, there was no shift of the resonant frequency. The graph of NH₄⁺ in Figure 5.7 c shows the sensitivity of IS-LC sensor. Here ΔR_f intensity is defined as $(R_f \text{ intensity} - \text{initial } R_f \text{ intensity}) / (\text{initial } R_f \text{ intensity})$. A strong linear relationship between NH₄⁺ ion concentration and ΔR_f intensity with a slope of 0.0349 and R^2 value greater than 0.91 demonstrates well the sensitivity of the NH₄⁺ membrane. In other words, if we know the ΔR_f intensity value, we can estimate the concentration of primary ion through a calibration. When the concentration of primary ion changes by 1 M, NH₄⁺ sensor shows 3.4% change in ΔR_f intensity. Furthermore, graphs for three different ions in Figure 5.7 c demonstrate

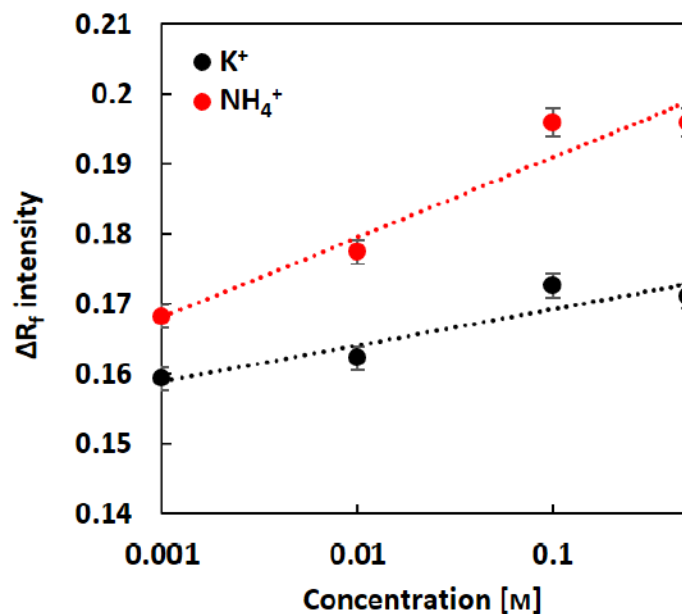


Figure 5.8. Experimental result of IS-LC sensor with NH_4^+ membrane – shows ΔR_f intensity of ISME with NH_4^+ membrane depending on 4 different concentrations of NH_4^+ and K^+ ion.

the selectivity of this IS- LC sensor. The ΔR_f intensity shows a strong linear relationship only with the concentration of NH_4^+ ion. Linear regressions of ΔR_f intensity depending on K^+ or Ca^{2+} ion concentration show lower slope values (-0.0109 and 0.0019 , respectively) and smaller R^2 values (0.6181 and 0.0997 , respectively) compared to the NH_4^+ case.

The NH_4^+ selective membrane has pores for NH_4^+ ions. Thus, the NH_4^+ membrane become charged with NH_4^+ ions when the solution with NH_4^+ ions is placed on top of it. If the concentration of NH_4^+ ion is increased, more pores are charged with NH_4^+ ions, and the R_f intensity is increased showing a strong linear relationship. However, the R_f intensity does not have a strong linear relationship with the concentration of nonprimary ions such as K^+ or Ca^{2+} . Thus, the NH_4^+ selective membrane shows the selectivity of NH_4^+ as a primary ion. Figure 5.8 shows relation between ΔR_f intensity and ion concentration in lower ion concentrations from 0.001 to 0.5 m. It shows a stronger linear relationship in case of NH_4^+ ion with higher slope value: 0.0049 and higher R^2 value as 0.93 , compared to the case of K^+ ion with lower slope 0.0022 and lower R^2 value as 0.86 with the logarithmic scale on the x-axis.

5.3.6. Characterization of ISME-LC Sensors on Humanoid Fingers

Fingertips of humanoid robotic hand were designed to have LC side and ISME side as shown in Figure 5.9 a. The LC was placed on top of the fingertip for the efficient wireless transmission. And the ISME sensor was placed at the bottom of the fingertip for the convenient contact between the fingertip and the chemical solution. This ISME-LC sensor are designed to make a closed circuit when two electrodes of the ISME sensor are connected electronically. The actual printed sample images of both sides of a fingertip is shown in Figure 5.9 b. The detailed fabrication process is explained in the 5.4 Materials and Methods section. An ISME shows a lower resistance value if the primary ion solution is applied between two electrodes compared to the case of nonprimary ion solution because the membrane allows only primary ions to pass through it. The primary ion means

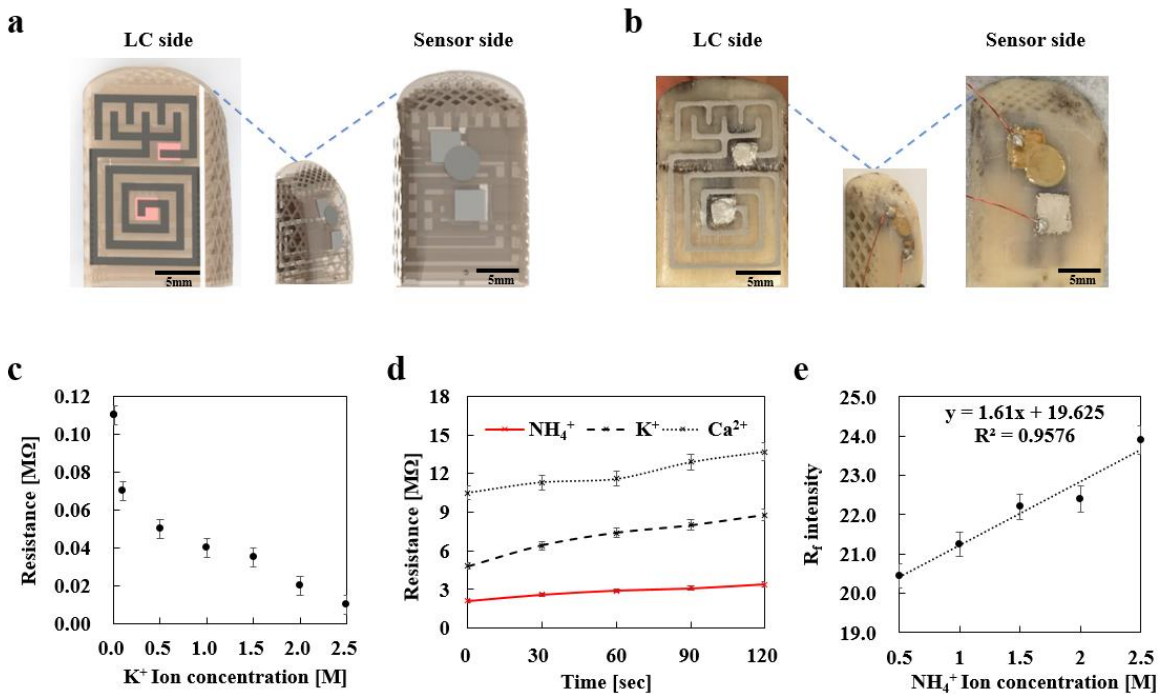


Figure 5.9. Qualification of wireless sensing of LC circuit connected with embedded ISME sensors. a) Design images of both sides (LC side and Sensor side) of a fingertip; b) Actual sample images of both sides of a fingertip; c) Electrical resistance change across K^+ ISME with application of different K^+ ion concentration; d) Electrical resistance change of NH_4^+ ISME applied with different ions such as 1 M NH_4^+ , 1 M K^+ , and 1 M Ca^{2+} ion solutions depending on time; e) R_f intensity change of the LC on a fingertip with the NH_4^+ ISME depending on NH_4^+ ion concentration.

the targeted ion which can be detected by the membrane selectively while nonprimary ions mean all other interference ions. The graph in Figure 5.9 c shows resistance change across the ISME of K^+ membrane with a drop (150 μ l) of K^+ ion solution of different concentration on top of the membrane and 2nd electrode. As the ion concentration is increased the resistance across ISME is reduced. This ISME sensor is also capable to detect primary ion (K^+) selectively among nonprimary ions. Figure 5.9 d shows the time-dependent resistance change between two electrodes of ISME sensor with NH_4^+ membrane when the two electrodes were connected with ion solutions of 1 M NH_4^+ , 1 M K^+ , and 1 M Ca^{2+} . Even though the resistance is slightly changed during the course of 2 minutes, the resistance values are remaining at three different ranges for different ions. Primary ion demonstrated the lowest resistance, which shows the selectivity of the membrane. Also, these fingers work wirelessly to detect different ion concentrations. Figure 5.9 e shows R_f intensity change of the LC on a fingertip with the ISME of NH_4^+ membrane depending on NH_4^+ ion concentration on top of the membrane. Here the linear regression equation is $y = 1.61x + 19.625$ where R^2 is 0.9576. Thus, the sensitivity of the ISME LC sensor in this case is 1.61 [dB/M]. As the ion concentration is increased, R_f intensity is increased. As the ion concentration increases, the resistance across the ISME is decreased, and the LC circuit shows a higher Q factor which is determined by observing a larger peak at the resonant frequency of the LC circuit. The relative standard error is defined as the standard error divided by the mean. The relative standard error for the resistance depending on different ion concentrations is less than 3.9% for all cases of ion concentrations for NH_4^+ , Ca^{2+} , and K^+ ions. This shows the reliability of the device is very high, and the result data is reproducible.

The stability of the circuit can be identified by the calculation of signal-to-noise (SNR) ratio which can be defined as the ratio of mean to standard deviation of measurement. The SNR ratio for the resistance depending on different ion concentrations of the built circuit is over 10 for all of the 4 cases of ion concentrations (0.1, 0.5, 1, 1.5 M) for NH_4^+ , Ca^{2+} , and K^+ ions, which shows the reliability of the circuit.

5.3.7. Demonstration of Differential Motion of Humanoid Fingers

Both the ISME sensor and LC circuit are designed and built on the fingertip of fingers in a humanoid robotic hand. Figure 5.10 a shows a schematic of full set of hand model with two fixed (a thumb and a pinky), and three movable fingers built with 3D printed

palm. A thumb and a pinky are printed along the palm using PLA by FFF. The rest three movable fingers are printed with a flexible filament and are designed as cellular solid composed of octet truss structure for light weight and mechanical durability. [146] This structure allows the finger to be durable in motion due to their high mechanical strength as compared to a solid structure using less material. The fingertips are printed separately with white ABS material which are later assembled with the finger body through a designed lock. This design makes it easy to replace the sensing fingertips. The fingertip has an LC circuit and an ISME sensor printed on top and bottom of the fingertip respectively by DIW printing. The fabricated index, middle, and ring fingers are equipped with individually targeted ion sensing capability with NH_4^+ , K^+ , and Ca^{2+} membranes respectively. The resistance change from the ISME is measured and utilized as a triggering signal to power motors that are used to actuate fingers. Each finger is connected to the control circuit by a couple of thin copper wires attached to two electrodes of the ISME sensor. A 110 rpm micro gear motor with 6 - 12 voltage capacity is used to actuate the finger by pulling a nylon string passing through the center of the porous finger body. In the circuit image of humanoid robotic hand in Figure 5.10 a, V_{in} indicates the applied input voltage. R_{ISME} is the resistance across the ISME sensor. Known resistor (R_{known}) is the resistance which is set to be in the similar range as the R_{ISME} . When the R_{ISME} and the R_{known} are in a similar range, differentiated output signals depending on different ion concentrations are observed clearly. Thus, the known resistor was chosen to be in the similar range of resistance with the measured R_{ISME} so that the ion concentration change can be detected sensitively. When V_{in} and R_{known} are constant, the voltage applied at R_{known} is determined by R_{ISME} from Ohm's law and Kirchhoff's Current Law. The detailed mechanism is explained in the MATERIALS AND METHODS section. The actual image of selectively moving humanoid fingers triggered by

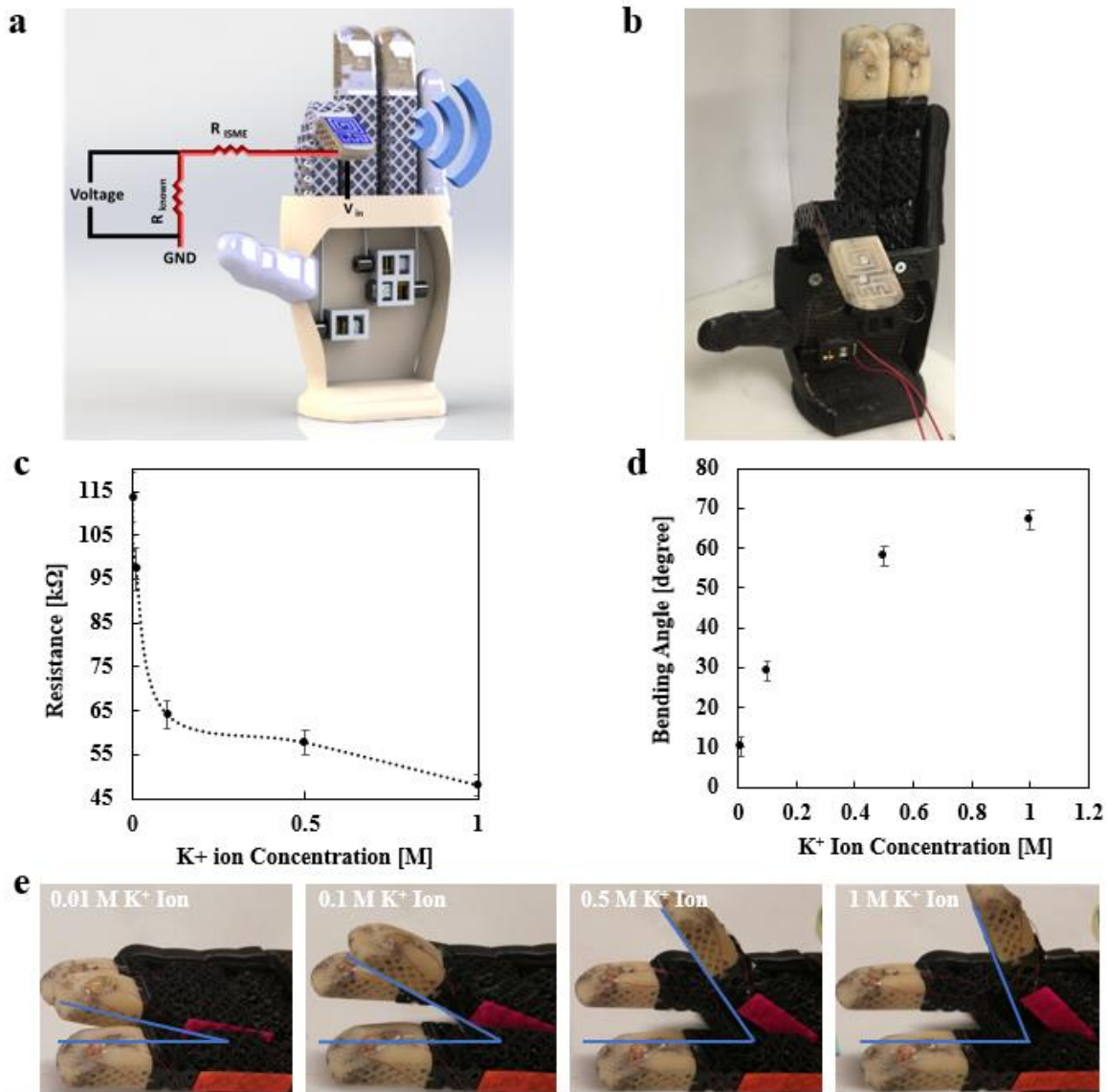


Figure 5.10. Differential bending motion of humanoid fingers with quantitative chemical sensing. a) The schematic of humanoid robotic hand with a voltage divider circuit diagram; b) The actual image of fabricated humanoid robotic hand with three movable fingers for detecting primary ions; c) The resistance change depending on the K⁺ ion concentration; d), e) Demonstration of different bending angle of the finger movement actuated by different K⁺ ion concentrations to the extent defined for the voltage thresholds.

chemical sensing is shown in Figure 5.10 b, and the index finger is bent as a demonstration. We further check the detection of sensing signal and mechanical movement of the finger based on the concentration of different ions. The particular ion is dropped on the ISME, and the sensing response is detected by measuring the resistance

change, as well as visually detected by the corresponding movement of the finger based on the resistance value. In Figure 5.10 c, as the concentration of potassium ions is increasing, R_{ISME} , the resistance across the ISME sensor detected by the micro-controller is decreasing. It shows the same trend compared to the experimental result in Figure 5.9 c. Smart bending of the finger where bending angle indicates the ion concentration is also demonstrated for the case of K^+ ions. Figure 5.10 e shows sequential images of a finger with the potassium ion membrane which bends up to a smaller angle when a drop of potassium ion solution with a lower concentration is applied, and bends up to a larger angle when a drop of potassium ion solution with a higher concentration is applied. The bending angle is approximated through post image processing. Series of triggered bending motion depending on different ion concentrations are captured in the Movie 1 in the Supplementary Material. If the concentration of potassium ion is increased, the R_{ISME} is decreased, and the voltage across R_{known} is increased. To realize the smart moving, we set up 4 different levels of motor speeds for each levels of voltage. Higher concentration of potassium ion induces higher voltage for R_{known} which triggers higher motor speed and result in a larger bending angle. (Figure 5.10 e) The voltage across the known resistor will be changed when the R_{ISME} is changing. If the input voltage, V_{in} is constant, lower R_{ISME} will make a higher voltage for the R_{known} .

5.4. Materials and Methods

5.4.1. Fabrication of LC Circuits and Electrodes

LC and two electrodes of ISME were three dimensionally connected to make a closed circuit when two electrodes of ISME are connected electronically. The center of the inductor on the LC side is connected to the rectangular 2nd electrode on the sensor side across the finger thickness. The end of IDC on the LC side is connected to the circular electrode of ISME on the sensor side. Then LC was printed with cellulose nanofiber (CNF) composite with silver nanowires (AgNWs) by using 3D printing system (SHOT mini 100Sx and ML-808GX, Musashi Engineering, Inc.). Thin wires were connected to two electrodes by silver epoxy to make connections to the main circuit including micro-controller: Arduino UNO. The membrane for a primary ion was fabricated by dropping a relevant membrane solution on top of the circular electrode and fully drying in a fume hood for about 14 hours. Three primary ions such as potassium, ammonium, and calcium ions were selected, and

membrane solutions prepared for those primary ions were applied to each of the ISME electrodes of three fingers. Each membrane was conditioned by 1M ion solutions of primary ions by applying enough amount of solution to cover the whole membrane and removing it after 30 minutes for more than 7 times.

The LC circuit was printed by the extrusion printing of a conductive CNF-AgNW ink on top of the fingertip. This fingertip was printed using FFF method with 2 kinds of materials. The first material is ABS, and the second material is Electrifi which is a conductive material. ISME sensor parts were printed at the bottom of the fingertip with silver nanoparticle-based ink by Musashi 3D printing system. The robot finger body was printed with a flexible material, Semiflex filament with 2 types of truss structures which show different mechanical properties. The first truss structure is octet cellular structure which is for the stiff parts of fingers. The second truss structure is re-entrant honeycomb auxetic structures for the bending part, joints of fingers.

5.4.2. Fabrication of Humanoid Robotic Finger

Multi-material FFF based 3D printing method is used to make humanoid fingertips and finger bodies. RostockMax SeeMeCNC® printer equipped with 4 nozzle extruder system is used to fabricate the lattice structures of the soft robotic finger body using Semiflex and the fingertip using ABS and Electrifi. Printing speed was 15 – 20 mm/sec on average with printing temperature around 220 °C for nozzle and 30 °C for bed. A 0.4 mm aluminum nozzle for metal printing and 0.25 mm brass nozzle for thermoplastic filaments are used with 100 µm printed layer resolution. The dimensions of the printed finger had a length of 120 mm and 15 mm in width. Lastly, the palm is printed using PLA filament for the integration with the motor. A hole with 0.1 mm diameter was designed in the finger to insert a nylon string by being fixed at the top of the finger, which allows the finger to bend when it is pulled.

5.4.3. Actuating Mechanism of Humanoid Finger

The movement of a finger is based on the actuation through a string that is pulled with a micro gear motor. The resistance across the ISME is measured through an ohm meter made from Arduino to actuate the finger depending on the ion sensing. The change in resistance is seen with respect to a reference resistance when the ion concentration or

ion type changes. The resistance threshold for each ion sensor is used to trigger the motor's movement. To make the ohm meter with Arduino, a known resistor and the resistance that need to be measured are set up as a voltage divider to measure the voltage. An algorithm is made to calculate the resistance from Ohm's law. The program sets up analog pin A₀ to read this voltage. To check the accuracy of this circuit, test runs were made by a placing a known value resistor. The values were accurate with less than 1% error. This is also when the known resistor has closer value to the unknown resistor. For controlling the motor, L293D motor driver IC is used, programmed with Arduino. The L293D is a 16 pin IC, with eight pins on each side dedicated to control a motor. It consists of 2 H-Bridge which allows to control low current rated motor and enable them to move in both clockwise and anti-clockwise directions. The output pins 3 and 4 are connected to the two terminals of the motor. All the connections between L293D and Arduino are mentioned in table S1.

5.5. Conclusion

Using the optimized CNF-AgNW ink, a wirelessly detectable ion sensor was fabricated with 3D printed LC circuit and ISME. This ISME-LC sensor was designed to show the selectivity of NH₄⁺ ion. The change of ion concentrations on ISME-LC sensor was wirelessly detected through VNA by measuring the magnitude of reflection coefficient S₁₁ and obtaining R_f intensity at the resonant frequency of the sensor; 2.36 GHz. We found that this ISME-LC sensor shows high selectivity of NH₄⁺ ion. This ISME-LC sensor with NH₄⁺ ion membrane also shows high sensitivity of 3.4%/ m change in R_f intensity with the NH₄⁺ ion concentration. ISME-LC sensor with NH₄⁺ membrane showed a linear response to concentration levels between 9,019 ppm and 45,096 ppm. As a comparison, MEMS-based sensor shows linear response at a lower range. For example, a miniature polymer-based chemical gas sensor array demonstrated a linear response to concentration levels between 2,000 and 10,000 ppm. [147]

The resistivity of printed inductor and IDC part is measured to be $7.58 \times 10^{-4} \Omega\text{m}$ ($1.32 \times 10^3 \text{ S m}^{-1}$ of conductivity). This IS-LC sensor shows the potential as a disposable and flexible application since it has only 1.2 mg of printed CNF-AgNW ink for an LC circuit on a flexible polyimide (PI) film. To our best knowledge, this is the first report on wireless detection of selective ions from an ISME integrated with an LC circuit. This 3D printed

light-weighted, flexible, disposable, and eco-friendly sensor with high sensitivity and selectivity will open a path to realize wearable ion sensors for IoT and wireless monitoring.

A chemical sensing humanoid robot which can trigger its motion differentially is essential for self-protecting and assisting humans in various chemical environments. If the robot detects a hazardous chemical, it can move away from the risk of possible damage caused by contact with the chemical or help human to remain in a safe place. The robot can also help human by checking the quality of water and primary ion levels in food or soil. Then it can give information or adjust the purity or primary ion levels. In this smartly moving humanoid robot system, ISME sensors detect different ion concentration and give different signals to the circuit through a micro-controller. The circuit gives feedback signal to the motor which actuates fingers in different ways. To achieve this goal, the optimized design and fabrication process of a smartly moving humanoid robotic hand based on ISME-LC sensors and metamaterials is presented in this paper. The ISME-LC sensors are embedded at the fingertips of the humanoid robotic hand through optimal 3D printing technologies. ISME-LC sensor functions based on the fact that the resistance across the ISME changes when the concentration of target ion changes. One of the advantages of ISME-LC sensor is its cost-efficient wireless communication without additional power source such as batteries. Thus, simple and easy fabrication is possible with minimum cost using the demonstrated 3D printing technologies. The chemical sensing humanoid robot hand can detect ion concentrations with minimum amount of sample solution. The demonstrated humanoid robot system equipped with eco-friendly, cost-efficient, and sensitive ISME-LC sensor will benefit the field of smart robotics. Our study demonstrates the motion actuation of humanoid robot hand from the chemical sensing. This topic can be extended for further study to detect different inputs. The ISME-LC sensor system can be used in assistive robots for household or in the medical field.

Chapter 6.

Conclusions and Future Work

In this chapter, an overview of the major achievements from this study is described. In the conclusions section, the contribution of this study to the 3D printed sensor field is summarized. Then the journal publications based on this PhD thesis research is listed. Finally, the future works which may be developed further are discussed.

6.1. Conclusions

This thesis focuses on developing 3D printable conductive materials for extrusion-based 3D printing, which can be used to print electrical components such as antenna, inductors, capacitors, as well as sensors. Photo-curable composite resin and nanocellulose composite inks are investigated and optimized to print conductive parts for wireless communication and chemical sensing, where conductive fillers such as AgNWs were added to constituent materials such as photo-curable resin or nanocellulose materials like CNC and CNF. The ratio of AgNWs was optimized to secure conductivity which is obtained from the percolated networks of AgNWs with a high aspect ratio. Two main variations regarding nozzle shapes and matrix materials in extrusion-based 3D printing were studied. First, the shapes of cross sections of nozzles were varied to understand the effect to the orientation of high aspect ratio fillers in printed objects. Second, CNC and CNF were used to understand the different behavior of high aspect ratio fillers in these matrix materials and the resultant electrical properties of printed parts when the shear stress is given in nozzles during the extrusion. An RFID antenna was printed with an ink formulated with a photo-curable resin and AgNWs to demonstrate conductive 3D printing. An LC resonator was printed using AgNW CNF ink to demonstrate that it's possible to print designed parts with conductivity and flexibility as well as the sustainability which is attributed to using biodegradable nanocellulose materials.

Overall, it is concluded that the composite ink materials which includes conductive high aspect ratio fillers show great potential to be used in extrusion-based 3D printing efficiently and applied in flexible and sustainable printed electronics which are demanded for its effectiveness in advanced manufacturing of various fields. Nanocellulose AgNW

inks can be used with DIW method through extrusion-based 3D printing for a wide range of printed electronics. Material properties of these inks such as viscosity and resistivity can be controlled by changing the types and ratio of solvents, conductive fillers, and matrix materials. It is a novel approach to make ISME LC sensor system for wireless chemical sensing and try to measure the change of intensity of the peak instead of resonant frequency change. To our best knowledge, this is the first thesis which report on wireless detection of selective ions from an ISME integrated with an LC circuit. Finally, this ISME LC sensing system showed the sensitivity and selectivity for the primary ion, which can be utilized in basic chemical detection and applied in assistant humanoid robot systems.

The following are the conclusions of this research, described in three research areas:

1. Nozzle-dependent extrusion-based 3D printing

- A photo-curable 3D printing system which is named as Print&Cure has been designed to realize a 3D printing system where the printing of a photo-curable ink composed of photo-curable resin and AgNWs is done by extrusion printing and the curing of printed parts is carried out by using UV light.
- The relationship between the shapes of cross section of extrusion nozzles such as circular and flat and the orientation of fillers with a high aspect ratio in printed parts was thoroughly studied.
- When the same ink composed of photo-curable resin and AgNWs is printed through two types of nozzles, samples printed through a circular nozzle showed aligned distribution of AgNWs, and samples printed through a flat nozzle showed random distribution of AgNWs, which made a percolated network that provides conductivity to the printed parts.
- The permittivity difference has also been observed from 3D printed samples with same concentration of AgNWs when they are 3D printed with different nozzles. Samples printed with circular nozzle have AgNWs aligned in the printing direction, which work like micro capacitors. On the other hand, samples printed through a flat nozzle have randomly distributed AgNWs and show lower permittivity compared to samples printed with a circular nozzle.

- The computational study confirms that the extrusion printing with a circular nozzle generates an aligned distribution of high aspect ratio fillers, and the extrusion printing with a flat nozzle induces a random distribution of high aspect ratio fillers.

2. Matrix-dependent extrusion-based 3D printing

- Optimizing and 3D printing of eco-friendly conductive ink based on nanocellulose material and AgNWs were studied. The different shapes and characteristics of nanocellulose materials such as CNF and CNC play an important role as a constituent material and affect the distribution and arrangement of AgNWs a lot. CNFs are like spaghetti noodles and form a web-like network easily which stop AgNWs from moving or rotating freely. CNCs have rod-like shapes which work like a media where AgNWs can move comparatively freely.
- Although both CNC-AgNW and CNF-AgNW based inks show sufficient 3D printability with shear-thinning behavior, 3D printed objects using CNF-AgNW ink show significantly better conductivity compared to 3D printed objects using CNC-AgNW ink for the same wt% of AgNWs.
- A parametric study on the thickness of LC circuits was simulated and also investigated by experiments to understand how to obtain the best performance from 3D printed CNF-AgNW LC sensors. 8 combinations of LC circuits with different thickness for L and C were designed. Increased thickness of L and C showed increased input impedance which corresponds to increased quality factor.
- Using the optimized CNF-AgNW ink, a wirelessly detectable ion sensor was fabricated with 3D printed LC circuit and ISME. This IS-LC sensor was designed to show the selectivity of NH_4^+ ion. The change of ion concentrations on IS-LC sensor was wirelessly detected through VNA by measuring the magnitude of reflection coefficient S_{11} and obtaining R_f intensity at the resonant frequency of the sensor; 2.36 GHz. This IS-LC sensor shows high selectivity of NH_4^+ ion. This IS-LC sensor with NH_4^+ ion membrane also shows high sensitivity of 3.4%/M change in R_f intensity with the NH_4^+ ion concentration.

- The resistivity of the optimized CNF-AgNW ink is $9.13 \times 10^{-5} \Omega\text{m}$. The resistivity of printed inductor and IDC part is measured to be $7.58 \times 10^{-4} \Omega\text{m}$ ($1.32 \times 10^3 \text{ S m}^{-1}$ of conductivity).
- This IS-LC sensor shows the potential as a disposable and flexible application since it has only 1.2 mg of printed CNF-AgNW ink for an LC circuit on a flexible polyimide (PI) film.

3. *Wireless chemical sensing & sensing robot*

- This study demonstrates the motion actuation of humanoid robot hand triggered by chemical sensing. The optimized design and fabrication process of a smartly moving humanoid robotic hand based on ISME-LC sensors and metamaterials is studied. LC resonator was optimized by comparing the inductance of inductors with 4 different shapes and different number of turns and choosing the shape and number of turns for the highest inductance. Two types of truss structures, octet cellular structure and re-entrant honeycomb auxetic structure were applied at finger body and finger joints respectively to make a flexible finger which can be printed at once and be bendable preferably at joints.
- The ISME-LC sensors are embedded at the fingertips of the humanoid robotic hand through optimal 3D printing technologies. The ISME-LC sensor of this study functions based on the fact that the resistance across the ISME changes when the concentration of target ion on electrodes of ISME changes. A simple and easy fabrication of sensors and robot arms is possible with minimum cost using the demonstrated 3D printing technologies such as FFF and DIW.
- The smartly moving humanoid robot system of this study mimics the process that humans sense stimulus, and the signal from the stimulus is sent to the brain, where the signal is processed and returned as a feedback signal to body parts that react accordingly. ISME sensors of the smartly moving humanoid robot system can detect different ion concentrations and give relevant signals to a circuit with a micro-controller. The micro-controller gives feedback signals to the motor which actuates a finger according to the programmed logic.

- The chemical sensing humanoid robot hand has a merit that it can detect ion concentrations with a minimum amount of sample solution.

6.2. Contributions

The work of this thesis contributes to the area of 3D printed electronics where 3D printed antenna, LC resonators, and chemical sensors are introduced based on conductive ink material and extrusion-based 3D printing technologies. An antenna with a resonant frequency for RFID communication, flexible disposable LC resonator as well as chemical sensors with sensitivity and selectivity can be achieved by using printable ink materials which can be formulated according to fabrication processes and the required electrical properties.

This thesis focuses on an ISME-LC sensor which can be applied into the field of flexible chemical sensors. It shows the performance of sensors through the study of sensitivity and selectivity for the primary ions and the demonstration of smartly moving robot fingers triggered by chemical sensing. The principal contributions of this thesis are:

- The study on the control of filler orientation in prints ushers the way to control composite material's electrical properties by nozzle shape dependent 3D printing.
- This can open a new platform of extrusion printing for controlling material's property by design of 3D printing parameters.
- To our best knowledge, this is the first report on wireless detection of selective ions from an ISME integrated with an LC circuit. This ISME LC sensor will contribute to the field of real time wireless chemical monitoring systems.
- This 3D printed light-weighted, flexible, disposable, and eco-friendly sensor with high sensitivity and selectivity will open a path to realize wearable ion sensors for IoT and wireless monitoring.
- One of the advantages of ISME-LC sensor is its cost-efficient wireless communication without additional power source such as batteries.
- The demonstrated humanoid robot system equipped with eco-friendly, cost-efficient, and sensitive ISME-LC sensor will benefit the field of smart robotics.

6.3. Publications

The following list of journals and conference papers were published during the PhD thesis duration in the AML lab.

Journal Publications

- T. Kim**, M. Kaur, and W. S. Kim, "Humanoid Robot Actuation through Precise Chemical Sensing Signals.", (accepted, *Advanced Materials Technology*, 2019)
- T. Kim**, C. Bao, M. Hausmann, G. Siqueira, T. Zimmermann, and W. S. Kim, "Electrochemical Sensors: 3D Printed Disposable Wireless Ion Sensors with Biocompatible Cellulose Composites." *Advanced Electronic Materials*, vol. 5, no. 2, pp. 1800778, 2019.
- T. Kim**, R. Trangkanukulkij, and W. S. Kim, "Nozzle Shape Guided Filler Orientation in 3D Printed Photo-Curable Nanocomposites." *Scientific Reports*, vol. 8, no. 1, pp. 3805, 2018.
- J. Park, **T. Kim** and W. S. Kim, "Conductive Cellulose Composites with Low Percolation Threshold for 3D Printed Electronics." *Scientific Reports*, vol. 7, no. 1, pp. 3246, 2017.
- L. Jian, **T. Kim**, J. Park, J. Wang, and W. S. Kim, "High Performance 3D Printed Electronics Using Electroless Plated Copper" *AIP Advances*, vol. 7, no. 3, pp. 035314, 2017.

Conference Publication

- T. Kim**, and W. S. Kim, "3D Printed Disposable Wireless Ion Selective Sensing Platform", *Proceeding of IEEE IFETC*, 1570547217, August 2019.
- T. Kim**, K. Andrews, and W. S. Kim, "3D Printed Flexible Coreless Transformers", *Proceeding of IEEE IFETC*, 8584017, August 2018.
- R. Trankanukulkij, **T. Kim**, and W. S. Kim, "A 3D printed Flexible Passive RFID for Temperature Sensing", *Proceeding of IEEE IFETC*, 8583913, August 2018.

6.4. Opportunities for Future Work

This research work focused on developing ink materials for DIW and understand the relationship between the nozzle shape and matrix material and orientation of high aspect ratio fillers. The following research directions can be considered as the extended research of this study:

1. The effect of dimension of nozzle such as the diameter of cross section of nozzle on overall properties may be investigated by additional experiment and parametric simulation. We expect that larger diameter of nozzles will generate enhanced alignment of AgNWs in case of a circular nozzle and more random distribution of AgNWs with a flat nozzle compared to nozzles of smaller diameter because a larger diameter nozzle will allow more variation of local velocity across the cross section of the nozzle compared to a smaller diameter nozzle.
2. Development of ink material with other types of nanocellulose such as modified cellulose nanocrystal and conductive fillers such as silver nanowires with different dimension and carbon nanotubes may be studied to enhance electrical properties or printability.
3. ISME-LC sensor may be further optimized by changing design and dimension of electrode and the fabrication process of membranes.
4. The ISME-LC sensor system can be extended for further study to detect different inputs and be used in assistive robots for household or in the medical field.
5. The same concept of triggering system may be miniaturized and applied to a system of a capsule robot which can navigate in human organs where the feedback from the chemical sensing may be an input signal to find the direction or trigger a movement of a part of the capsule robot, for example, releasing medicine.
6. Actuation of chemical sensing robot may be further investigated for self-protecting and assisting robots in various chemical environments. If the robot detects a hazardous chemical, it can move away from the risk of possible damage caused by contact with the chemical or help human to remain in a safe place.

7. The passive RF wireless sensing part in ISME-LC sensor system may be improved into an active RF wireless sensing part in order to utilize a longer communication distance as well as a wider range of operation.

References

- [1] Gibson, I. (2014). *Additive Manufacturing Technologies*. New York: Springer.
- [2] Most used 3D printing technologies worldwide 2018 | Statista. (n.d.). Retrieved from <http://www.statista.com/statistics/756690/worldwide-most-used-3d-printing-technologies>.
- [3] Lewis, J. (2006). Direct Ink Writing of 3D Functional Materials. *Advanced Functional Materials*, 16(17), 2193-2204. doi:10.1002/adfm.200600434.
- [4] Kim, T., Bao, C., Hausmann, M., Siqueira, G., Zimmermann, T., & Kim, W. S. (2019). Electrochemical Sensors: 3D Printed Disposable Wireless Ion Sensors with Biocompatible Cellulose Composites (Adv. Electron. Mater. 2/2019). *Advanced Electronic Materials*, 5(2), 1970007. doi:10.1002/aelm.201970007.
- [5] Ngo, T. D., Kashani, A., Imbalzano, G., Nguyen, K. T., & Hui, D. (2018). Additive manufacturing (3D printing): A review of materials, methods, applications and challenges. *Composites Part B: Engineering*, 143, 172-196. doi:10.1016/j.compositesb.2018.02.012
- [6] Kuo, C., Liu, L., Teng, W., Chang, H., Chien, F., Liao, S., . . . Chen, C. (2016). Preparation of starch/acrylonitrile-butadiene-styrene copolymers (ABS) biomass alloys and their feasible evaluation for 3D printing applications. *Composites Part B: Engineering*, 86, 36-39. doi:10.1016/j.compositesb.2015.10.005.
- [7] Song, Y., Li, Y., Song, W., Yee, K., Lee, K., & Tagarielli, V. (2017). Measurements of the mechanical response of unidirectional 3D-printed PLA. *Materials & Design*, 123, 154-164. doi:10.1016/j.matdes.2017.03.051.
- [8] Ferreira, R. T., Amatte, I. C., Dutra, T. A., & Bürger, D. (2017). Experimental characterization and micrography of 3D printed PLA and PLA reinforced with short carbon fibers. *Composites Part B: Engineering*, 124, 88-100. doi:10.1016/j.compositesb.2017.05.013.
- [9] Hou, Z., Tian, X., Zhang, J., & Li, D. (2018). 3D printed continuous fibre reinforced composite corrugated structure. *Composite Structures*, 184, 1005-1010. doi:10.1016/j.compstruct.2017.10.080.
- [10] Alzarrug, F. A., Dimitrijević, M. M., Heinemann, R. M., Radojević, V., Stojanović, D. B., Uskoković, P. S., & Aleksić, R. (2015). The use of different alumina fillers for improvement of the mechanical properties of hybrid PMMA composites. *Materials & Design*, 86, 575-581. doi:10.1016/j.matdes.2015.07.069

- [11] Singh, R., Singh, N., Amendola, A., & Fraternali, F. (2017). On the wear properties of Nylon6-SiC-Al₂O₃ based fused deposition modelling feed stock filament. *Composites Part B: Engineering*, 119, 125-131. doi:10.1016/j.compositesb.2017.03.042.
- [12] Decker, C. (1998). The use of UV irradiation in polymerization. *Polymer International*, 45(2), 133-141. doi:10.1002/(sici)1097-0126(199802)45:23.0.co;2-f.
- [13] Postiglione, G., Natale, G., Griffini, G., Levi, M., & Turri, S. (2015). Conductive 3D microstructures by direct 3D printing of polymer/carbon nanotube nanocomposites via liquid deposition modeling. *Composites Part A: Applied Science and Manufacturing*, 76, 110-114. doi:10.1016/j.compositesa.2015.05.014
- [14] Sofla, M. R., Brown, R. J., Tsuzuki, T., & Rainey, T. J. (2016). A comparison of cellulose nanocrystals and cellulose nanofibres extracted from bagasse using acid and ball milling methods. *Advances in Natural Sciences: Nanoscience and Nanotechnology*, 7(3), 035004. Licensed under CC BY 3.0. doi:10.1088/2043-6262/7/3/035004
- [15] Withell, A., Diegel, O., Grupp, I., Reay, S., Beer, D. D., & Potgieter, J. (2011). Porous ceramic filters through 3D printing. *Innovative Developments in Virtual and Physical Prototyping*, 313-318. doi:10.1201/b11341-50
- [16] Yang, G., Mo, J., Kang, Z., Dohrmann, Y., List, F. A., Green, J. B., . . . Zhang, F. (2018). Fully printed and integrated electrolyzer cells with additive manufacturing for high-efficiency water splitting. *Applied Energy*, 215, 202-210. doi:10.1016/j.apenergy.2018.02.001
- [17] Eckel, Z. C., Zhou, C., Martin, J. H., Jacobsen, A. J., Carter, W. B., & Schaedler, T. A. (2015). Additive manufacturing of polymer-derived ceramics. *Science*, 351(6268), 58-62. doi:10.1126/science.aad2688
- [18] Wang, X., Jiang, M., Zhou, Z., Gou, J., & Hui, D. (2017). 3D printing of polymer matrix composites: A review and prospective. *Composites Part B: Engineering*, 110, 442-458. doi:10.1016/j.compositesb.2016.11.034
- [19] Mohamed, O. A., Masood, S. H., & Bhowmik, J. L. (2015). Optimization of fused deposition modeling process parameters: A review of current research and future prospects. *Advances in Manufacturing*, 3(1), 42-53. doi:10.1007/s40436-014-0097-7
- [20] Chohan, J. S., Singh, R., Boparai, K. S., Penna, R., & Fraternali, F. (2017). Dimensional accuracy analysis of coupled fused deposition modeling and vapour smoothing operations for biomedical applications. *Composites Part B: Engineering*, 117, 138-149. doi:10.1016/j.compositesb.2017.02.045

- [21] Vaezi, M., Seitz, H., & Yang, S. (2012). A review on 3D micro-additive manufacturing technologies. *The International Journal of Advanced Manufacturing Technology*, 67(5-8), 1721-1754. doi:10.1007/s00170-012-4605-2
- [22] Boley, J. W., Chaudhary, K., Ober, T. J., Khorasaninejad, M., Chen, W. T., Hanson, E., . . . Lewis, J. A. (2016). High-Operating-Temperature Direct Ink Writing of Mesoscale Eutectic Architectures. *Advanced Materials*, 29(7), 1604778. doi:10.1002/adma.201604778
- [23] Skylar-Scott, M. A., Gunasekaran, S., & Lewis, J. A. (2016). Laser-assisted direct ink writing of planar and 3D metal architectures. *Proceedings of the National Academy of Sciences*, 113(22), 6137-6142. doi:10.1073/pnas.1525131113
- [24] Utela, B., Storti, D., Anderson, R., & Ganter, M. (2008). A review of process development steps for new material systems in three dimensional printing (3DP). *Journal of Manufacturing Processes*, 10(2), 96-104. doi:10.1016/j.jmapro.2009.03.002
- [25] Gul, J. Z., Sajid, M., Rehman, M. M., Siddiqui, G. U., Shah, I., Kim, K., . . . Choi, K. H. (2018). 3D printing for soft robotics – a review. *Science and Technology of Advanced Materials*, 19(1), 243-262. doi:10.1080/14686996.2018.1431862
- [26] Manapat, J. Z., Chen, Q., Ye, P., & Advincula, R. C. (2017). 3D Printing of Polymer Nanocomposites via Stereolithography. *Macromolecular Materials and Engineering*, 302(9), 1600553. doi:10.1002/mame.201600553
- [27] Gibson, I., Rosen, D., & Stucker, B. (2015). Directed Energy Deposition Processes. *Additive Manufacturing Technologies*, 245-268. doi:10.1007/978-1-4939-2113-3_10
- [28] LENS 850-R system - repair and fabrication of large metal parts. (n.d.). Retrieved from <https://www.multistation.com/en/product/lens-850-r-system-repair-and-fabrication-of-large-metal-parts/>
- [29] Williams, S. W., Martina, F., Addison, A. C., Ding, J., Pardal, G., & Colegrove, P. (2016). Wire Arc Additive Manufacturing. *Materials Science and Technology*, 32(7), 641-647. doi:10.1179/1743284715y.0000000073
- [30] The EBAM™ 300 Series. (n.d.). Retrieved from <https://www.sciaky.com/largest-metal-3d-printer-available>
- [31] Kong, Y. L., Tamargo, I. A., Kim, H., Johnson, B. N., Gupta, M. K., Koh, T., . . . Mcalpine, M. C. (2019). Correction to 3D Printed Quantum Dot Light-Emitting Diodes. *Nano Letters*, 19(3), 2187-2187. doi:10.1021/acs.nanolett.9b00598
- [32] Shemelya, C., Cedillos, F., Aguilera, E., Maestas, E., Ramos, J., Espalin, D., . . . Macdonald, E. (2013). 3D printed capacitive sensors. *2013 IEEE Sensors*. doi:10.1109/icsens.2013.6688247

- [33] Guth, U., Vonau, W., & Zosel, J. (2009). Recent developments in electrochemical sensor application and technology—a review. *Measurement Science and Technology*, 20(4), 042002. doi:10.1088/0957-0233/20/4/042002
- [34] Bakker, E., & Qin, Y. (2006). Electrochemical Sensors. *Analytical Chemistry*, 78(12), 3965-3984. doi:10.1021/ac060637m
- [35] Arnold, M. A., & Solsky, R. L. (1986). Ion-selective electrodes. *Analytical Chemistry*, 58(5), 84-101. doi:10.1021/ac00296a009
- [36] Ghosh, T., Chung, H., & Rieger, J. (2017). All-Solid-State Sodium-Selective Electrode with a Solid Contact of Chitosan/Prussian Blue Nanocomposite. *Sensors*, 17(11), 2536. Licensed under CC BY 4.0. doi:10.3390/s17112536
- [37] Huang, Q., Dong, L., & Wang, L. (2016). LC Passive Wireless Sensors Toward a Wireless Sensing Platform: Status, Prospects, and Challenges. *Journal of Microelectromechanical Systems*, 25(5), 822-841. doi:10.1109/jmems.2016.2602298
- [38] Chawla, V., & Ha, D. (2007). An overview of passive RFID. *IEEE Communications Magazine*, 45(9), 11-17. doi:10.1109/mcom.2007.4342873
- [39] Cho, H., Jang, H., & Baek, Y. (2011). Large scale active RFID system utilizing ZigBee networks. *2011 IEEE International Conference on Consumer Electronics (ICCE)*. doi:10.1109/icce.2011.5722666
- [40] Zhang, X., Wei, S., Haldolaarachchige, N., Colorado, H. A., Luo, Z., Young, D. P., & Guo, Z. (2012). Magnetoresistive Conductive Polyaniline–Barium Titanate Nanocomposites with Negative Permittivity. *The Journal of Physical Chemistry C*, 116(29), 15731-15740. doi:10.1021/jp303226u
- [41] Park, J. S., Kim, T., & Kim, W. S. (2017). Conductive Cellulose Composites with Low Percolation Threshold for 3D Printed Electronics. *Scientific Reports*, 7(1). doi:10.1038/s41598-017-03365-w
- [42] Gao, J., Liu, Y., Wang, Y., Hu, X., Yan, W., Ke, X., . . . Ren, X. (2017). Designing High Dielectric Permittivity Material in Barium Titanate. *The Journal of Physical Chemistry C*, 121(24), 13106-13113. doi:10.1021/acs.jpcc.7b04636
- [43] Prateek, Thakur, V. K., & Gupta, R. K. (2016). Recent Progress on Ferroelectric Polymer-Based Nanocomposites for High Energy Density Capacitors: Synthesis, Dielectric Properties, and Future Aspects. *Chemical Reviews*, 116(7), 4260-4317. doi:10.1021/acs.chemrev.5b00495
- [44] Wang, G., Huang, Y., Wang, Y., Jiang, P., & Huang, X. (2017). Substantial enhancement of energy storage capability in polymer nanocomposites by encapsulation of BaTiO₃ NWs with variable shell thickness. *Physical Chemistry Chemical Physics*, 19(31), 21058-21068. doi:10.1039/c7cp04096b

- [45] Patton, S. T., Frasca, A. J., Hu, J., Varshney, V., Phillips, B. S., Roy, A. K., & Voevodin, A. A. (2016). Multiphysics characterization of multi-walled carbon nanotube thermoplastic polyurethane polymer nanocomposites during compression. *Carbon*, *98*, 638-648. doi:10.1016/j.carbon.2015.11.051
- [46] Kim, P., Jones, S., Hotchkiss, P., Haddock, J., Kippelen, B., Marder, S., & Perry, J. (2007). Phosphonic Acid-Modified Barium Titanate Polymer Nanocomposites with High Permittivity and Dielectric Strength. *Advanced Materials*, *19*(7), 1001-1005. doi:10.1002/adma.200602422
- [47] Zhang, X., He, Q., Gu, H., Wei, S., & Guo, Z. (2013). Polyaniline stabilized barium titanate nanoparticles reinforced epoxy nanocomposites with high dielectric permittivity and reduced flammability. *Journal of Materials Chemistry C*, *1*(16), 2886. doi:10.1039/c3tc30129j
- [48] Madusanka, N., Shivareddy, S. G., Hiralal, P., Eddleston, M. D., Choi, Y., Oliver, R. A., & Amaratunga, G. A. (2016). Nanocomposites of TiO₂/cyanoethylated cellulose with ultra high dielectric constants. *Nanotechnology*, *27*(19), 195402. doi:10.1088/0957-4484/27/19/195402
- [49] Kumar, G. S., Vishnupriya, D., Chary, K. S., & Patro, T. U. (2016). High dielectric permittivity and improved mechanical and thermal properties of poly(vinylidene fluoride) composites with low carbon nanotube content: Effect of composite processing on phase behavior and dielectric properties. *Nanotechnology*, *27*(38), 385702. doi:10.1088/0957-4484/27/38/385702
- [50] Zeraati, A. S., Arjmand, M., & Sundararaj, U. (2017). Correction to "Silver Nanowire/MnO₂ Nanowire Hybrid Polymer Nanocomposites: Materials with High Dielectric Permittivity and Low Dielectric Loss". *ACS Applied Materials & Interfaces*, *9*(37), 32412-32412. doi:10.1021/acsami.7b13012
- [51] Arbatti, M., Shan, X., & Cheng, Z. (2007). Ceramic-Polymer Composites with High Dielectric Constant. *Advanced Materials*, *19*(10), 1369-1372. doi:10.1002/adma.200601996
- [52] Hu, N., Karube, Y., Yan, C., Masuda, Z., & Fukunaga, H. (2008). Tunneling effect in a polymer/carbon nanotube nanocomposite strain sensor. *Acta Materialia*, *56*(13), 2929-2936. doi:10.1016/j.actamat.2008.02.030
- [53] Sun, Y., Mayers, B., Herricks, T., & Xia, Y. (2003). Polyol Synthesis of Uniform Silver Nanowires: A Plausible Growth Mechanism and the Supporting Evidence. *Nano Letters*, *3*(7), 955-960. doi:10.1021/nl034312m
- [54] Arjmand, M., Moud, A. A., Li, Y., & Sundararaj, U. (2015). Outstanding electromagnetic interference shielding of silver nanowires: Comparison with carbon nanotubes. *RSC Advances*, *5*(70), 56590-56598. doi:10.1039/c5ra08118a

- [55] Compton, B. G., & Lewis, J. A. (2014). 3D Printing: 3D-Printing of Lightweight Cellular Composites (Adv. Mater. 34/2014). *Advanced Materials*, 26(34), 6043-6043. doi:10.1002/adma.201470235
- [56] Tjong, S. C. (2011). Polymer nanocomposite bipolar plates reinforced with carbon nanotubes and graphite nanosheets. *Energy & Environmental Science*, 4(3), 605. doi:10.1039/c0ee00689k
- [57] Du, F., Fischer, J. E., & Winey, K. I. (2005). Effect of nanotube alignment on percolation conductivity in carbon nanotube/polymer composites. *Physical Review B*, 72(12). doi:10.1103/physrevb.72.121404
- [58] Tang, H., Malakooti, M. H., & Sodano, H. A. (2013). Relationship between orientation factor of lead zirconate titanate nanowires and dielectric permittivity of nanocomposites. *Applied Physics Letters*, 103(22), 222901. doi:10.1063/1.4833416
- [59] Heller, B. P., Smith, D. E., & Jack, D. A. (2016). Effects of extrudate swell and nozzle geometry on fiber orientation in Fused Filament Fabrication nozzle flow. *Additive Manufacturing*, 12, 252-264. doi:10.1016/j.addma.2016.06.005
- [60] Martin-Gallego, M., Lopez-Manchado, M. A., Calza, P., Roppolo, I., & Sangermano, M. (2014). Gold-functionalized graphene as conductive filler in UV-curable epoxy resin. *Journal of Materials Science*, 50(2), 605-610. doi:10.1007/s10853-014-8619-z
- [61] Lebel, L. L., Aissa, B., Khakani, M. A., & Therriault, D. (2010). Ultraviolet-Assisted Direct-Write Fabrication of Carbon Nanotube/Polymer Nanocomposite Microcoils. *Advanced Materials*, 22(5), 592-596. doi:10.1002/adma.200902192
- [62] Cooperstein, I., Layani, M., & Magdassi, S. (2015). 3D printing of porous structures by UV-curable O/W emulsion for fabrication of conductive objects. *Journal of Materials Chemistry C*, 3(9), 2040-2044. doi:10.1039/c4tc02215g
- [63] Verweyst, B. E., & Tucker, C. L. (2002). Fiber Suspensions in Complex Geometries: Flow/Orientation Coupling. *The Canadian Journal of Chemical Engineering*, 80(6), 1093-1106. doi:10.1002/cjce.5450800611
- [64] Cross, M. M. (1965). Rheology of non-Newtonian fluids: A new flow equation for pseudoplastic systems. *Journal of Colloid Science*, 20(5), 417-437. doi:10.1016/0095-8522(65)90022-x
- [65] Mi, H., Li, Z., Turng, L., Sun, Y., & Gong, S. (2014). Silver nanowire/thermoplastic polyurethane elastomer nanocomposites: Thermal, mechanical, and dielectric properties. *Materials & Design (1980-2015)*, 56, 398-404. doi:10.1016/j.matdes.2013.11.029

- [66] Martins, R., Ferreira, I., & Fortunato, E. (2011). Electronics with and on paper. *Physica Status Solidi (RRL) - Rapid Research Letters*, 5(9), 332-335. doi:10.1002/pssr.201105247
- [67] Vicente, A. T., Araújo, A., Mendes, M. J., Nunes, D., Oliveira, M. J., Sanchez-Sobrado, O., . . . Martins, R. (2018). Multifunctional cellulose-paper for light harvesting and smart sensing applications. *Journal of Materials Chemistry C*, 6(13), 3143-3181. doi:10.1039/c7tc05271e
- [68] Gaspar, D., Fernandes, S. N., Oliveira, A. G., Fernandes, J. G., Grey, P., Pontes, R. V., . . . Fortunato, E. (2014). Nanocrystalline cellulose applied simultaneously as the gate dielectric and the substrate in flexible field effect transistors. *Nanotechnology*, 25(9), 094008. doi:10.1088/0957-4484/25/9/094008
- [69] Lee, K., Aitomäki, Y., Berglund, L. A., Oksman, K., & Bismarck, A. (2014). On the use of nanocellulose as reinforcement in polymer matrix composites. *Composites Science and Technology*, 105, 15-27. doi:10.1016/j.compscitech.2014.08.032
- [70] Zhang, Y., Song, P., Liu, H., Li, Q., & Fu, S. (2016). Morphology, healing and mechanical performance of nanofibrillated cellulose reinforced poly(ϵ -caprolactone)/epoxy composites. *Composites Science and Technology*, 125, 62-70. doi:10.1016/j.compscitech.2016.01.008
- [71] Hoeng, F., Denneulin, A., & Bras, J. (2016). Use of nanocellulose in printed electronics: A review. *Nanoscale*, 8(27), 13131-13154. doi:10.1039/c6nr03054h
- [72] Siqueira, G., Kokkinis, D., Libanori, R., Hausmann, M. K., Gladman, A. S., Neels, A., . . . Studart, A. R. (2017). Cellulose Nanocrystal Inks for 3D Printing of Textured Cellular Architectures. *Advanced Functional Materials*, 27(12), 1604619. doi:10.1002/adfm.201604619.
- [73] Li, Y., Zhu, H., Wang, Y., Ray, U., Zhu, S., Dai, J., . . . Hu, L. (2017). Cellulose-Nanofiber-Enabled 3D Printing of a Carbon-Nanotube Microfiber Network. *Small Methods*, 1(10), 1700222. doi:10.1002/smt.201700222
- [74] Jakus, A. E., Secor, E. B., Rutz, A. L., Jordan, S. W., Hersam, M. C., & Shah, R. N. (2015). Three-Dimensional Printing of High-Content Graphene Scaffolds for Electronic and Biomedical Applications. *ACS Nano*, 9(4), 4636-4648. doi:10.1021/acsnano.5b01179
- [75] Koga, H., Saito, T., Kitaoka, T., Nogi, M., Suganuma, K., & Isogai, A. (2013). Transparent, Conductive, and Printable Composites Consisting of TEMPO-Oxidized Nanocellulose and Carbon Nanotube. *Biomacromolecules*, 14(4), 1160-1165. doi:10.1021/bm400075f
- [76] Martins, R., Gaspar, D., Mendes, M. J., Pereira, L., Martins, J., Bahubalindrani, P., . . . Fortunato, E. (2018). Papertronics: Multigate paper transistor for multifunction applications. *Applied Materials Today*, 12, 402-414. doi:10.1016/j.apmt.2018.07.002

- [77] Barras, R., Cunha, I., Gaspar, D., Fortunato, E., Martins, R., & Pereira, L. (2017). Printable cellulose-based electroconductive composites for sensing elements in paper electronics. *Flexible and Printed Electronics*, 2(1), 014006. doi:10.1088/2058-8585/aa5ef9
- [78] Sultan, S., Siqueira, G., Zimmermann, T., & Mathew, A. P. (2017). 3D printing of nano-cellulosic biomaterials for medical applications. *Current Opinion in Biomedical Engineering*, 2, 29-34. doi:10.1016/j.cobme.2017.06.002
- [79] Håkansson, K. M., Henriksson, I. C., Vázquez, C. D., Kuzmenko, V., Markstedt, K., Enoksson, P., & Gatenholm, P. (2016). Solidification of 3D Printed Nanofibril Hydrogels into Functional 3D Cellulose Structures. *Advanced Materials Technologies*, 1(7), 1600096. doi:10.1002/admt.201600096
- [80] Hölzl, K., Lin, S., Tytgat, L., Vlierberghe, S. V., Gu, L., & Ovsianikov, A. (2016). Bioink properties before, during and after 3D bioprinting. *Biofabrication*, 8(3), 032002. doi:10.1088/1758-5090/8/3/032002
- [81] Espalin, D., Muse, D. W., Macdonald, E., & Wicker, R. B. (2014). 3D Printing multifunctionality: Structures with electronics. *The International Journal of Advanced Manufacturing Technology*, 72(5-8), 963-978. doi:10.1007/s00170-014-5717-7
- [82] Fu, K., Wang, Y., Yan, C., Yao, Y., Chen, Y., Dai, J., . . . Hu, L. (2016). Graphene Oxide-Based Electrode Inks for 3D-Printed Lithium-Ion Batteries. *Advanced Materials*, 28(13), 2587-2594. doi:10.1002/adma.201505391
- [83] Yang, C., Wong, C. P., & Yuen, M. M. (2013). Printed electrically conductive composites: Conductive filler designs and surface engineering. *Journal of Materials Chemistry C*, 1(26), 4052. doi:10.1039/c3tc00572k
- [84] Michalska, A. J., Appaih-Kusi, C., Heng, L. Y., Walkiewicz, S., & Hall, E. A. (2004). An Experimental Study of Membrane Materials and Inner Contacting Layers for Ion-Selective K Electrodes with a Stable Response and Good Dynamic Range. *Analytical Chemistry*, 76(7), 2031-2039. doi:10.1021/ac0353132
- [85] Zhang, T., Lai, C., Fierke, M. A., Stein, A., & Bühlmann, P. (2012). Advantages and Limitations of Reference Electrodes with an Ionic Liquid Junction and Three-Dimensionally Ordered Macroporous Carbon as Solid Contact. *Analytical Chemistry*, 84(18), 7771-7778. doi:10.1021/ac3011507
- [86] Kim, H. J., Hummel, J. W., & Birrell, S. J. (2006). Evaluation Of Nitrate And Potassium Ion-Selective Membranes For Soil Macronutrient Sensing. *Transactions of the ASABE*, 49(3), 597-606. doi:10.13031/2013.20476
- [87] Lutov, V., & Mikhelson, K. (1994). A new pH sensor with a PVC membrane: Analytical evaluation and mechanistic aspects. *Sensors and Actuators B: Chemical*, 19(1-3), 400-403. doi:10.1016/0925-4005(93)01010-2

- [88] Tian, K., Prestgard, M., & Tiwari, A. (2014). A review of recent advances in nonenzymatic glucose sensors. *Materials Science and Engineering: C*, 41, 100-118. doi:10.1016/j.msec.2014.04.013
- [89] Ahmad, R., Tripathy, N., Park, J., & Hahn, Y. (2015). A comprehensive biosensor integrated with a ZnO nanorod FET array for selective detection of glucose, cholesterol and urea. *Chemical Communications*, 51(60), 11968-11971. doi:10.1039/c5cc03656a
- [90] Nakata, S., Arie, T., Akita, S., & Takei, K. (2017). Wearable, Flexible, and Multifunctional Healthcare Device with an ISFET Chemical Sensor for Simultaneous Sweat pH and Skin Temperature Monitoring. *ACS Sensors*, 2(3), 443-448. doi:10.1021/acssensors.7b00047
- [91] Chen, Y., Sarangadharan, I., Sukesan, R., Hseih, C., Lee, G., Chyi, J., & Wang, Y. (2018). High-field modulated ion-selective field-effect-transistor (FET) sensors with sensitivity higher than the ideal Nernst sensitivity. *Scientific Reports*, 8(1). doi:10.1038/s41598-018-26792-9
- [92] Machida, S., Shimada, H., & Motoyama, Y. (2018). Multiple-channel detection of cellular activities by ion-sensitive transistors. *Japanese Journal of Applied Physics*, 57(4S). doi:10.7567/jjap.57.04fm03
- [93] Pinto, J. V., Branquinho, R., Barquinha, P., Alves, E., Martins, R., & Fortunato, E. (2013). Extended-Gate ISFETs Based on Sputtered Amorphous Oxides. *Journal of Display Technology*, 9(9), 729-734. doi:10.1109/jdt.2012.2227298
- [94] Rose, D. P., Ratterman, M. E., Griffin, D. K., Hou, L., Kelley-Loughnane, N., Naik, R. R., . . . Heikenfeld, J. C. (2015). Adhesive RFID Sensor Patch for Monitoring of Sweat Electrolytes. *IEEE Transactions on Biomedical Engineering*, 62(6), 1457-1465. doi:10.1109/tbme.2014.2369991
- [95] Wang, H., Wang, X., Barfidokht, A., Park, J., Wang, J., & Mercier, P. P. (2018). A Battery-Powered Wireless Ion Sensing System Consuming 5.5 nW of Average Power. *IEEE Journal of Solid-State Circuits*, 53(7), 2043-2053. doi:10.1109/jssc.2018.2815657
- [96] Martínez-Olmos, A., Fernández-Salmerón, J., Lopez-Ruiz, N., Torres, A. R., Capitan-Vallvey, L. F., & Palma, A. J. (2013). Screen Printed Flexible Radiofrequency Identification Tag for Oxygen Monitoring. *Analytical Chemistry*, 85(22), 11098-11105. doi:10.1021/ac4028802
- [97] Potyrailo, R. A., & Morris, W. G. (2007). Multianalyte Chemical Identification and Quantitation Using a Single Radio Frequency Identification Sensor. *Analytical Chemistry*, 79(1), 45-51. doi:10.1021/ac061748o

- [98] Potyrailo, R. A., Surman, C., Morris, W. G., & Go, S. (2009). Selective detection of chemical species in liquids and gases using radio-frequency identification (RFID) sensors. *TRANSDUCERS 2009 - 2009 International Solid-State Sensors, Actuators and Microsystems Conference*. doi:10.1109/sensor.2009.5285777
- [99] Kim, J., Imani, S., Araujo, W. R., Warchall, J., Valdés-Ramírez, G., Paixão, T. R., . . . Wang, J. (2015). Wearable salivary uric acid mouthguard biosensor with integrated wireless electronics. *Biosensors and Bioelectronics*, *74*, 1061-1068. doi:10.1016/j.bios.2015.07.039
- [100] Kim, J., Jeerapan, I., Imani, S., Cho, T. N., Bandodkar, A., Cinti, S., . . . Wang, J. (2016). Noninvasive Alcohol Monitoring Using a Wearable Tattoo-Based Iontophoretic-Biosensing System. *ACS Sensors*, *1*(8), 1011-1019. doi:10.1021/acssensors.6b00356
- [101] Matzeu, G., Oquigley, C., Mcnamara, E., Zuliani, C., Fay, C., Glennon, T., & Diamond, D. (2016). An integrated sensing and wireless communications platform for sensing sodium in sweat. *Analytical Methods*, *8*(1), 64-71. doi:10.1039/c5ay02254a
- [102] Abrar, M. A., Dong, Y., Lee, P. K., & Kim, W. S. (2016). Bendable Electrochemical Lactate Sensor Printed with Silver Nano-particles. *Scientific Reports*, *6*(1). doi:10.1038/srep30565
- [103] Liang, X., Zhao, T., Hu, Y., & Sun, R. (2014). Dielectric properties of silver nanowires-filled polyvinylidene fluoride composite with low percolation threshold. *Journal of Nanoparticle Research*, *16*(9). doi:10.1007/s11051-014-2578-9
- [104] Becraft, M. L., & Metzner, A. B. (1992). The rheology, fiber orientation, and processing behavior of fiber-filled fluids. *Journal of Rheology*, *36*(1), 143-174. doi:10.1122/1.550359
- [105] Folgar, F., & Tucker, C. L. (1984). Orientation Behavior of Fibers in Concentrated Suspensions. *Journal of Reinforced Plastics and Composites*, *3*(2), 98-119. doi:10.1177/073168448400300201
- [106] Sanchez-Botero, L., Dimov, A. V., Li, R., Smilgies, D., & Hinstroza, J. P. (2018). In Situ and Real-Time Studies, via Synchrotron X-ray Scattering, of the Orientational Order of Cellulose Nanocrystals during Solution Shearing. *Langmuir*, *34*(18), 5263-5272. doi:10.1021/acs.langmuir.7b04403
- [107] Querejeta-Fernandez, A., Chauve, G., Methot, M., Gourevich, I., Bouchard, J., & Kumacheva, E. (2014). Chiral plasmonic activity of cholesteric films formed by gold nanorods and cellulose nanocrystals. *14th IEEE International Conference on Nanotechnology*. doi:10.1109/nano.2014.6968002

- [108] Hausmann, M. K., Rühls, P. A., Siqueira, G., Läuger, J., Libanori, R., Zimmermann, T., & Studart, A. R. (2018). Dynamics of Cellulose Nanocrystal Alignment during 3D Printing. *ACS Nano*, *12*(7), 6926-6937. doi:10.1021/acsnano.8b02366
- [109] Kim, T., Trangkanukulkij, R., & Kim, W. S. (2018). Nozzle Shape Guided Filler Orientation in 3D Printed Photo-curable Nanocomposites. *Scientific Reports*, *8*(1). doi:10.1038/s41598-018-22107-0
- [110] Wang, J., Huang, S., Lu, X., Xu, Z., Zhao, Y., Li, J., & Wang, X. (2017). Wet-spinning of highly conductive nanocellulose–silver fibers. *Journal of Materials Chemistry C*, *5*(37), 9673-9679. doi:10.1039/c7tc03217j
- [111] Kuzmenko, V., Karabulut, E., Pernevik, E., Enoksson, P., & Gatenholm, P. (2018). Tailor-made conductive inks from cellulose nanofibrils for 3D printing of neural guidelines. *Carbohydrate Polymers*, *189*, 22-30. doi:10.1016/j.carbpol.2018.01.097
- [112] Peshkova, M. A., Koltashova, E. S., Khripoun, G. A., & Mikhelson, K. N. (2015). Improvement of the upper limit of the ISE Nernstian response by tuned galvanostatic polarization. *Electrochimica Acta*, *167*, 187-193. doi:10.1016/j.electacta.2015.03.139
- [113] Ivanova, A., & Mikhelson, K. (2018). Electrochemical Properties of Nitrate-Selective Electrodes: The Dependence of Resistance on the Solution Concentration. *Sensors*, *18*(7), 2062. doi:10.3390/s18072062
- [114] Shishehgar, M., Kerr, D., & Blake, J. (2018). A systematic review of research into how robotic technology can help older people. *Smart Health*, *7-8*, 1-18. doi:10.1016/j.smhl.2018.03.002
- [115] Feil-Seifer, D., & Mataric, M. (n.d.). Socially Assistive Robotics. *9th International Conference on Rehabilitation Robotics, 2005. ICORR 2005*. doi:10.1109/icorr.2005.1501143
- [116] Penders, J., Alboul, L., Witkowski, U., Naghsh, A., Saez-Pons, J., Herbrechtsmeier, S., & El-Habbal, M. (2011). A Robot Swarm Assisting a Human Fire-Fighter. *Advanced Robotics*, *25*(1-2), 93-117. doi:10.1163/016918610x538507
- [117] Lee, W., Lee, Y., Park, G., Hong, S., & Kang, Y. (2016). A whole-body rescue motion control with task-priority strategy for a rescue robot. *Autonomous Robots*, *41*(1), 243-258. doi:10.1007/s10514-016-9562-4
- [118] Chang, W. H., & Kim, Y. (2013). Robot-assisted Therapy in Stroke Rehabilitation. *Journal of Stroke*, *15*(3), 174. doi:10.5853/jos.2013.15.3.174

- [119] Naotunna, I., Perera, C. J., Sandaruwan, C., Gopura, R., & Lalitharatne, T. D. (2015). Meal assistance robots: A review on current status, challenges and future directions. *2015 IEEE/SICE International Symposium on System Integration (SII)*. doi:10.1109/sii.2015.7404980
- [120] Takashima, R., Kawamoto, H., & Sankai, Y. (2017). An ultra-multijointed assistive robot finger. *2017 IEEE International Conference on Robotics and Biomimetics (ROBIO)*. doi:10.1109/robio.2017.8324472
- [121] Fukaya, N., & Ogasawara, Y. (2017). Development of humanoid hand with cover integrated link mechanism for daily life work. *2017 IEEE 6th Global Conference on Consumer Electronics (GCCE)*. doi:10.1109/gcce.2017.8229384
- [122] Ting, C., Yeo, W., King, Y., Chuah, Y., Lee, J., & Khaw, W. (2014). Humanoid Robot: A Review of the Architecture, Applications and Future Trend. *Research Journal of Applied Sciences, Engineering and Technology*, 7(7), 1364-1369. doi:10.19026/rjaset.7.402
- [123] Kamakura, N., Ohmura, M., Ishii, H., Mitsuboshi, F., & Miura, Y. (1978). Positional Patterns For Prehension In Normal Hands. *The Japanese Journal of Rehabilitation Medicine*, 15(2), 65-82. doi:10.2490/jjrm1963.15.65
- [124] Kappassov, Z., Corrales, J., & Perdereau, V. (2015). Tactile sensing in dexterous robot hands — Review. *Robotics and Autonomous Systems*, 74, 195-220. doi:10.1016/j.robot.2015.07.015
- [125] Han, D., Nie, H., Chen, M., & Wang, X. (2016). Temperature prediction with humanoid finger sensor based on Fourier's law. *Measurement Science and Technology*, 27(2), 025105. doi:10.1088/0957-0233/27/2/025105
- [126] Ciui, B., Martin, A., Mishra, R. K., Nakagawa, T., Dawkins, T. J., Lyu, M., . . . Wang, J. (2018). Chemical Sensing at the Robot Fingertips: Toward Automated Taste Discrimination in Food Samples. *ACS Sensors*, 3(11), 2375-2384. doi:10.1021/acssensors.8b00778
- [127] Ramalingame, R., Lakshmanan, A., Müller, F., Thomas, U., & Kanoun, O. (2019). Highly sensitive capacitive pressure sensors for robotic applications based on carbon nanotubes and PDMS polymer nanocomposite. *Journal of Sensors and Sensor Systems*, 8(1), 87-94. doi:10.5194/jsss-8-87-2019
- [128] Bu, T., Xiao, T., Yang, Z., Liu, G., Fu, X., Nie, J., . . . Wang, Z. L. (2018). Stretchable Triboelectric-Photonic Smart Skin for Tactile and Gesture Sensing. *Advanced Materials*, 30(16), 1800066. doi:10.1002/adma.201800066
- [129] Núñez, C. G., Navaraj, W. T., Polat, E. O., & Dahiya, R. (2017). Energy-Autonomous, Flexible, and Transparent Tactile Skin. *Advanced Functional Materials*, 27(18), 1606287. doi:10.1002/adfm.201606287

- [130] Craggs, A., Moody, G. J., & Thomas, J. D. (1974). PVC matrix membrane ion-selective electrodes. Construction and laboratory experiments. *Journal of Chemical Education*, 51(8), 541. doi:10.1021/ed051p541
- [131] Feng, Y., Xie, L., Chen, Q., & Zheng, L. (2015). Low-Cost Printed Chipless RFID Humidity Sensor Tag for Intelligent Packaging. *IEEE Sensors Journal*, 15(6), 3201-3208. doi:10.1109/jsen.2014.2385154
- [132] Tanaka, H., Yoshikawa, M., Oyama, E., Wakita, Y., & Matsumoto, Y. (2013). Development of Assistive Robots Using International Classification of Functioning, Disability, and Health: Concept, Applications, and Issues. *Journal of Robotics*, 2013, 1-12. doi:10.1155/2013/608191
- [133] Singh, E., Meyyappan, M., & Nalwa, H. S. (2017). Flexible Graphene-Based Wearable Gas and Chemical Sensors. *ACS Applied Materials & Interfaces*, 9(40), 34544-34586. doi:10.1021/acsami.7b07063
- [134] Lee, M. Y., Lee, H. R., Park, C. H., Han, S. G., & Oh, J. H. (2018). Organic Transistor-Based Chemical Sensors for Wearable Bioelectronics. *Accounts of Chemical Research*, 51(11), 2829-2838. doi:10.1021/acs.accounts.8b00465
- [135] Bandodkar, A. J., Jeerapan, I., & Wang, J. (2016). Wearable Chemical Sensors: Present Challenges and Future Prospects. *ACS Sensors*, 1(5), 464-482. doi:10.1021/acssensors.6b00250
- [136] Armstrong, R. D., & Horvai, G. (1990). ChemInform Abstract: Properties of PVC Based Membranes Used in Ion-Selective Electrodes. *ChemInform*, 21(15). doi:10.1002/chin.199015343
- [137] Dong, L., Wang, L., & Huang, Q. (2016). An LC Passive Wireless Multifunctional Sensor Using a Relay Switch. *IEEE Sensors Journal*, 16(12), 4968-4973. doi:10.1109/jsen.2016.2550537
- [138] Qin, L., Shen, D., Wei, T., Tan, Q., Luo, T., Zhou, Z., & Xiong, J. (2015). A Wireless Passive LC Resonant Sensor Based on LTCC under High-Temperature/Pressure Environments. *Sensors*, 15(7), 16729-16739. doi:10.3390/s150716729
- [139] Barras, R., Cunha, I., Gaspar, D., Fortunato, E., Martins, R., & Pereira, L. (2017). Printable cellulose-based electroconductive composites for sensing elements in paper electronics. *Flexible and Printed Electronics*, 2(1), 014006. doi:10.1088/2058-8585/aa5ef9
- [140] Baptista, A., Martins, J., Fortunato, E., Martins, R., Borges, J., & Ferreira, I. (2011). Thin and flexible bio-batteries made of electrospun cellulose-based membranes. *Biosensors and Bioelectronics*, 26(5), 2742-2745. doi:10.1016/j.bios.2010.09.055

- [141] Mohan, S., Hershenson, M. D., Boyd, S., & Lee, T. (1999). Simple accurate expressions for planar spiral inductances. *IEEE Journal of Solid-State Circuits*, 34(10), 1419-1424. doi:10.1109/4.792620
- [142] Filipski, K. J., Varma, M. V., El-Kattan, A. F., Ambler, C. M., Ruggeri, R. B., Goosen, T. C., & Cameron, K. O. (2013). Intestinal Targeting of Drugs: Rational Design Approaches and Challenges. *Current Topics in Medicinal Chemistry*, 13(7), 776-802. doi:10.2174/1568026611313070002
- [143] Mapara, S. S., & Patravale, V. B. (2017). Medical capsule robots: A renaissance for diagnostics, drug delivery and surgical treatment. *Journal of Controlled Release*, 261, 337-351. doi:10.1016/j.jconrel.2017.07.005
- [144] Wheeler, H. (1928). Simple Inductance Formulas for Radio Coils. *Proceedings of the IRE*, 16(10), 1398-1400. doi:10.1109/jrproc.1928.221309
- [145] Rosa, E. B. (1906). *Calculation of the self-inductance of single-layer coils*. Govt. Print. Off.
- [146] M. Kaur, W.S. Kim. (2019). Toward a Smart Compliant Robotic Gripper Equipped with 3D-Designed Cellular Fingers. *Advanced Intelligent Systems* 1900019.
- [147] Zee, F., & Judy, J. W. (2001). Micromachined polymer-based chemical gas sensor array. *Sensors and Actuators B: Chemical*, 72(2), 120–128. doi: 10.1016/s0925-4005(00)00638-9

Appendix A.

Journal paper discussed in Chapter 3


Nozzle Shape Guided Filler Orientation in 3D Printed Photo-curable Nanocomposites

Note: Used with permission from Nature Publishing Group. This article was published in [Kim, T., Trangkanukulkij, R., & Kim, W. S. (2018). Nozzle Shape Guided Filler Orientation in 3D Printed Photo-curable Nanocomposites. *Scientific Reports*, 8(1). doi:10.1038/s41598-018-22107-0]

SCIENTIFIC REPORTS

OPEN

Nozzle Shape Guided Filler Orientation in 3D Printed Photo-curable Nanocomposites

Taeil Kim, Ramita Trangkanukulkij & Woo Soo Kim 

Received: 31 October 2017

Accepted: 16 February 2018

Published online: 28 February 2018

Here, we report guided orientation of silver nanowires (AgNWs) in extruded patterns with photo-curable 3D printing technology. A printable conductive composite material composed of polymer matrix and silver nanowires shows significantly varied electrical properties depending on the cross-sectional shape of printing nozzles: flat or circular. The composite is designed to have highly conductive AgNWs and a dielectric polymer matrix like photo-curable methacrylate resin. The dielectric permittivity of photo-curable composite resin with 1.6 vol. % of AgNWs printed through a circular nozzle showed 27. However, the same resin showed much lower permittivity with 20 when it is printed with a flat nozzle. The cross-sectional sample morphology shows that AgNWs printed with a circular nozzle are aligned, and AgNWs printed with a flat nozzle are randomly distributed. A computational simulation of paste extrusion with two different nozzle shapes showed clearly different fluidic velocities at the nozzle exit, which contributes to different fiber orientation in printed samples. A radio frequency identification sensor is fabricated with 3D printed composite using a flat nozzle for the demonstration of AgNW based 3D printed conductor.

Polymer nanocomposites (PNCs) became a promising solution of various applications for their flexibility and processability as well as differentiated mechanical, electrical properties compared with pristine polymers¹. Recent development of PNCs demonstrates functional properties as well as easy processability required in current electronic device industry. Especially materials with high conductivity or high dielectric permittivity gained great attention. Materials with high conductivity can be applied to fabricate basic electrical parts such as interconnections, inductors, and electrodes of batteries². PNCs with high conductivity can be utilized for 3D printing of electromagnetic interference (EMI) shielding applications which will contribute to miniaturization of portable electronic devices. Materials with high dielectric permittivity can be applied to parts with high capacitance and improved energy storages³. PNCs with high dielectric permittivity can be applied to flexible and transparent parts of wearable electronic devices^{4–6}.

Various types of PNCs were investigated to prepare a flexible material with high conductivity or high dielectric permittivity^{6–8}. Numerous kinds of different polymers such as epoxy, Polyimides (PI), Poly (methyl methacrylate) (PMMA), and Polydimethylsiloxane (PDMS) were used as a matrix in PNCs. Ferroelectric ceramic fillers such as BaTiO₃, PbTiO₃, and TiO₂ or conductive nano wires such as carbon nanotube (CNT) and AgNW were applied to attain enhanced electrical properties^{8–11}. But high loads of ceramic fillers, which is required for high dielectric constant, sometimes worsen the mechanical property of the material¹². PNCs with conductive fillers may exhibit better mechanical flexibility as well as improved electrical properties with lower volume fraction of fillers compared to PNCs with ceramic fillers. A PNC with conductive fillers like AgNWs can be conductive if these conductive nanoscale fillers form a conductive path called as a percolated network which enables the electrons travel through the material. Electrons can move from one conductive filler to another if they are in contact or jump between conductive fillers if they are close to each other, known as tunneling effect¹³. On the other hand, conductive nanoscale fillers and polymer matrix may be arranged in an ordered structure so that the conductive nanoscale fillers can work as pairs of electrodes of capacitors. And the polymer matrix between nanoscale fillers can work as dielectric to form millions of nanoscale capacitors and exhibit high dielectric properties¹¹.

In this study, we chose AgNW as a nanoscale conductive filler to prepare PNCs in order to utilize the high anisotropic character of AgNWs. AgNW is a rod-like anisotropic structure. So its properties may be controlled more effectively by alignment in a matrix material compared to other isotropic nanoscale fillers with a spherical

Additive Manufacturing Laboratory, School of Mechatronic Systems Engineering, Simon Fraser University, BC, Canada. Correspondence and requests for materials should be addressed to W.S.K. (email: woosook@sfu.ca)

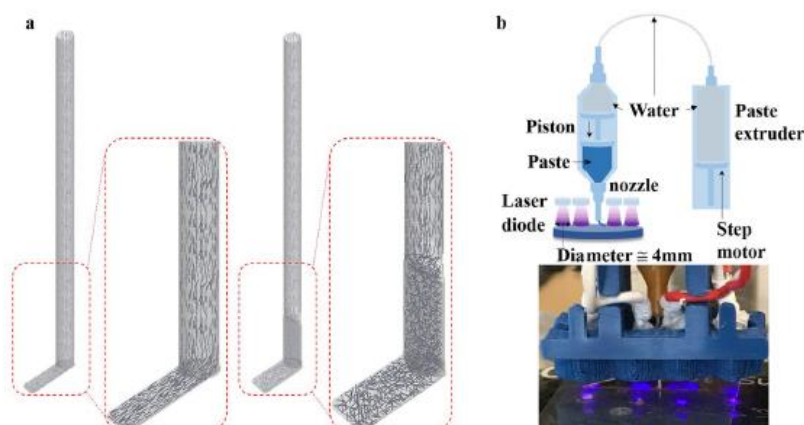


Figure 1. Schematics of the extrusion at nozzles and Print & Cure extrusion 3D printing system. (a) The scheme of print-induced aligned/random distribution of high aspect ratio fillers of a circular nozzle and a flat nozzle, (b) The scheme of Print & Cure extrusion 3D printing system (up) and a close-up image of Print & Cure printing head (bottom).

structure. Also, high aspect ratio (100–500) of AgNW induces lower percolation threshold compared to spherical fillers¹⁴. Therefore, AgNW has higher conductivity compared to other fillers like carbon nanotube for highly conductive or highly dielectric applications^{2,15}. Also, the large surface area of AgNW contributes to the efficient improvement of conductive or dielectric property of polymers.

The orientation of fillers in the matrix of nanocomposites affects conductive or dielectric properties as well as mechanical properties. Research has been focused on enhanced mechanical property of nanocomposites with aligned distribution of fillers^{16,17}. The relation between electrical properties such as conductivity or permittivity and the orientation of fillers has been also investigated^{19,20}. If it is possible to use the same compositional materials with the same volume fraction of AgNWs to differentiate electrical properties, then it makes price competitiveness. And if it is possible to control the alignment and orientation of filler distribution, then composites' electrical properties can be tuned by a small part of manufacturing process. For example, changing the nozzle shape of an extruder can give more efficient processability. In this report, it is demonstrated that the electrical properties of composite materials can be tunable through nozzle dependent extrusion 3D printing.

Controlling the filler orientation of PNCs may improve electrical properties. One of the simple and useful techniques to control filler orientation in extrusion printing is to change nozzles' shapes at the end of the extruder. In an extrusion process through nozzles, the converging parts of nozzles will increase and the diverging parts of nozzles will decrease the level of alignment of fillers along the extruded direction²¹. By applying these converging and diverging nozzles in extrusion printing, we can study the relation between the orientation of nanoscale fillers and composites' electrical properties. It is known that the fabrication process determines material's properties. There are many 3D printing methodologies such as solution casting, filament printing, extrusion printing, and Digital Light Processing (DLP)^{11,18}. The extrusion printing is an adequate printing method for nanocomposite materials because it enables us to control filler orientation more easily than other fabrication methods such as solution casting and DLP. This study mainly demonstrates attaining different electrical properties with the nanocomposite, which has same concentration of AgNWs in polymer composites by controlling the orientation of fillers.

A silicone rubber (Ecoflex[®] 00–30) was utilized as a polymer matrix in a PNC with AgNWs. This PNC was extruded and dried at room temperature. Initially distributed AgNWs inside of polymer sank down to the bottom region of printed sample during the drying process. Because AgNWs are heavier than silicone polymer, they are able to move to the bottom of prints. Therefore, more AgNWs were precipitated at the bottom of a printed sample in case of a PNC with a higher volume fraction of AgNWs. In order to solve this sinking issue, Print & Cure (P&C) system was newly developed to fix AgNWs' distribution inside of polymer matrix using by UV light right after the extrusion. It has been reported with direct writing of carbon nanotube/polymer nanocomposite materials^{22,23}. In P&C system, extruded AgNWs were not sunk down and stayed in the layer where they were printed because methacrylate polymer resin is photo-cured right after printing. Eventually, the cured composite holds AgNWs as printed. Photo-curing is an appropriate technique to keep distribution of AgNWs as printed. The P&C resin, a UV curable resin composed of oligomer (Urethane triacrylate), photo initiator (Phenylbis phosphine oxide), and monomer (Methacrylic acid) is prepared as a matrix which will be cured by UV light with 405 nm in wavelength. The change depending on the extent of alignment of AgNWs was investigated.

Figure 1a shows a schematic of the extrusion of high aspect ratio fillers in a matrix and print-induced distribution of fillers with two kinds of nozzle tips. The left image describes the extrusion from a circular nozzle which has a cylinder shape with a circular cross section. The right image shows the extrusion from a flat nozzle which has a cylinder shape with an ellipse-like flat cross section in the lower part at the end of nozzle. These two images also visualize the assumption that the circular nozzle generates aligned orientation of fillers in a printed sample,

and the flat nozzle generates random distribution of fillers after extrusion. This assumption was investigated and verified by experiments as well as a computational simulation. The actual circular nozzle has a diameter of 840 μm and length of 17 mm. The flat nozzle has the same length as the circular nozzle with tapered end part of the nozzle: 3 mm. The tapered flat part at the end of the nozzle has an ellipsoidal cross section with the wider and the narrower inner diameters of 1.2 mm and 360 μm respectively.

Figure 1b shows the scheme of P&C extrusion 3D printing system and the real image of its printing head. Four laser diodes give UV light with the wavelength of 405 nm to the printed object and cure it. The focal range of UV light from one diode is about 4 mm in diameter. These diodes are arranged on a line which is parallel to the printing direction along X axis for the most effective curing. It is important to keep diodes as close as possible from the printing surface in order to secure best curing performance because the intensity of the light is dramatically decreased when the distance between diodes and the printing surface is increased.

Results and Discussion

In this section, experimental sample morphology is investigated with velocity profile images to prove AgNWs' nozzle dependent extruding distribution in PNCs, then measured dielectric permittivity of printed samples with two types of nozzles are discussed. Finally, randomly extruded AgNWs' conductive printing was demonstrated for the application of RFID tag. The numerical model was solved by ANSYS polyflow using Cross law as the governing equation. The geometry of computational domain was defined and generated as a model composed of two parts which are the fluid in a nozzle and the extrudate for two types of nozzles respectively. Figure 2a,b show the simulation result of extrusion printing with a circular and a flat nozzle. This simulation was designed as a decoupled model²⁴. It is assumed that the nanoscale fillers will orient following the flow of polymer matrix because the volume fraction of nanoscale fillers is very low. The extrusion direction is from positive Y to negative Y along the Y axis. A type of generalized Newtonian fluid, Cross model was used for the calculation of simulation.

$$\eta = \frac{\eta_0}{1 + (\lambda\dot{\gamma})^m} \quad (1)$$

where, η_0 = zero-shear-rate viscosity, λ = natural time (inverse of the shear rate at which the fluid changes from Newtonian to power-law behavior), $\dot{\gamma}$ = shear rate, and m = power-law index. Cross model exhibits shear-thinning behavior, which is dominant viscoelastic behavior of majority of polymers. The degree of dependence of viscosity on shear rate in shear-thinning region can be easily adjusted by changing power-law index. For example, lower power-law index means less dependence of viscosity on shear rate. Zero-shear-rate viscosity was estimated as 1500 cps, because the P&C resin with 1.6 vol. % of AgNWs shows viscosity around 1500 cps. Natural time was set as 0.2 s, which is close to the Newtonian limit where natural time is 0. Though Cross initially proposed that power-law index = 2/3 was satisfactory for large number of cases, power-law index of this study was set as 0.3 to reflect the lower dependence of viscosity on shear rate of the AgNW P&C resin composite of this study²⁵. As it is assumed that there is a uniform velocity profile at the end of extrudate, normal and tangential forces were set to zero.

Since the problem involves a free surface, the domain was divided into two subdomains. Subdomain 1 is the fluid inside of a nozzle. Subdomain 2 is the extrudate outside of a nozzle. Boundaries were defined only at the inlet, nozzle wall, free surface, and outlet (at the end of extrudate). No boundary was defined at the nozzle exit where the fluid in the nozzle interfaces the fluid in the extrudate. Thus, we didn't have to justify the inaccuracy at the boundary at the nozzle exit. Boundary conditions are as following. At the inlet, volumetric flow rate Q is set as $4 \times 10^{-5} \text{ cm}^3/\text{s}$. The boundary between the nozzle wall and the fluid is set as zero velocity because the fluid is assumed to stick to the wall, which is the no-slip condition. Hence the fluid has no velocity relative to the nozzle wall at this solid-fluid interface. At the boundary of the free surface after nozzle exit, velocity profile is not uniform. The velocity field must be tangential to a free surface, which corresponds to the kinematic condition, $v \cdot n = 0$. This condition requires the starting line of the free surface as initial condition. The starting line of the free surface is the intersection of nozzle wall and surface of Extrudate in this study. Lastly, the boundary condition at the flow outlet (the end of extrudate) is zero normal and tangential forces because it is assumed that a uniform velocity profile is reached at the end of the extrudate where no external stress is applied to the extrudate. Whole nozzle and extrudate was simulated without generating symmetry surfaces. Coordinate system is defined as following. Y axis is at the center of nozzles. Negative Y direction is extrusion direction. X axis and Z axis are perpendicular to Y axis. The center of coordinate system is located at the center of the nozzle exit where $X = Y = Z = 0$ for two types of nozzles. While coupled model is with fluid and filler, decoupled model, a model without the filler is applied in order to simplify the simulation process.

Velocity profile images of the fluid (Fig. 2a,b) clearly show higher velocity (red color) at the center of both nozzles. 10 equally spaced lines were defined on XY planes to analyze fluid dynamics more in detail and understand the fiber orientation. In case of the circular nozzle, 10 yellow vertical lines were defined on XY plane which lies on the axis of rotation (a black vertical line) of cylinder shape model of fluid in the nozzle as in Fig. 2a. Because of the symmetric structure of a circular nozzle, 10 lines were placed only on the half of the plane where X is positive. In case of a flat nozzle, 10 equally spaced lines were placed on XY plane which lies on the axis of rotation of cylinder shape part of fluid model and cuts the flat part through the largest diameter of the ellipse-like cross section. Because of the symmetric structure of a flat nozzle, 10 lines were placed only on the half of the plane where X is positive. Fluid velocities were calculated along these 10 lines first. Then the average velocity graphs in Fig. 2c-e were obtained from these velocity graphs along 10 lines. First of all, equally spaced 10 lines were defined to obtain detailed local velocity data as the velocity profile is not uniform. Then, the average flow velocity was calculated from obtained data along equally spaced 10 lines in order to compare the major difference of fluid flow in two types of nozzles.

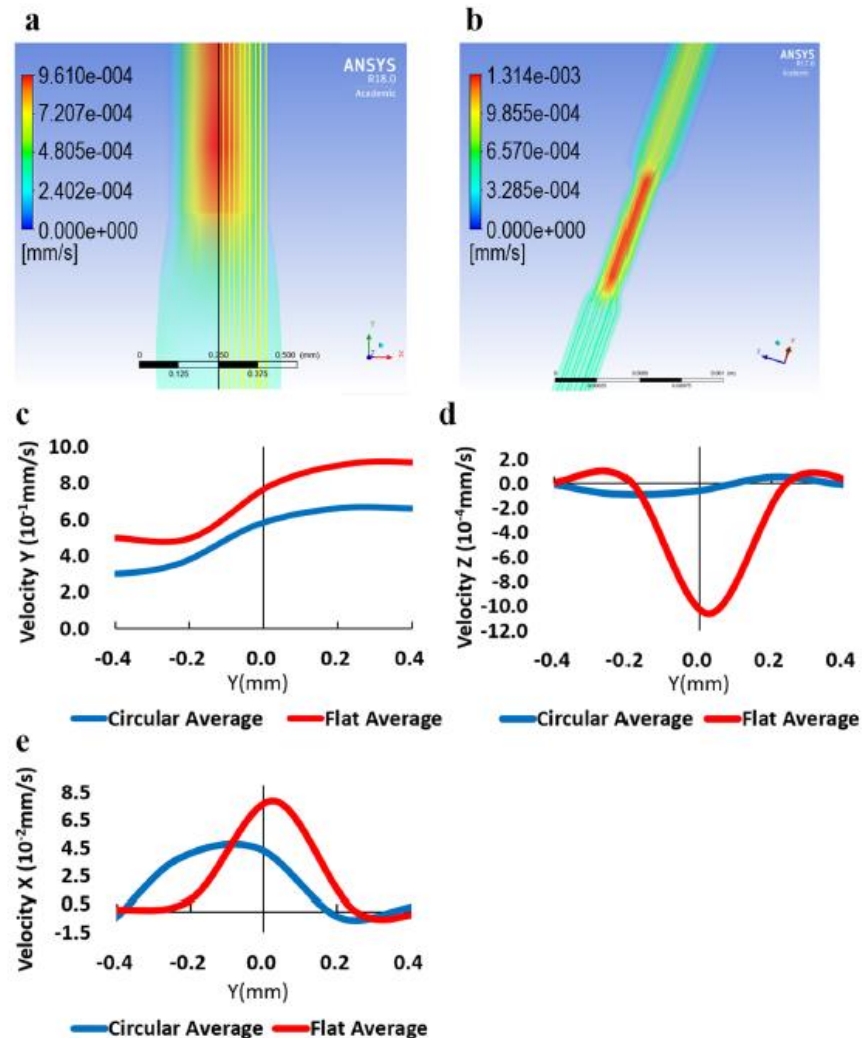


Figure 2. Filler extrusion simulation depending on nozzle shapes. Velocity profile of the fluid extruded at a circular nozzle (a) and a flat nozzle (b), and Average Velocity Y, Z, and X (c, d, and e) of fluid around the exit of a circular nozzle and a flat nozzle.

The fiber orientation is estimated by calculation of the second order orientation tensor, A_{33} by using velocity gradients of fluid. The second order orientation tensor is defined as $A_{ij} = \int p_i p_j \psi(\mathbf{p}) d\mathbf{p}$. Here, \mathbf{p} is the unit vector in the direction of primary axis of the fiber. $p_1 = \sin\theta \cos\varphi$, $p_2 = \sin\theta \sin\varphi$, $p_3 = \cos\theta$, θ and φ are angles between coordinate axis and vector \mathbf{p} . The A_{33} component shows the fiber alignment according to the extrusion direction²¹. The velocities and velocity gradients can be calculated along 10 equally spaced lines from CFD results. If A_{33} is close to 1, it means a nearly uniaxial alignment of fibers along the extrusion direction. After the nozzle exit, A_{33} decreases mainly due to the expansion flow and the negative elongation component²¹. In this simulation, calculated A_{33} component varies from 0.94 to 1.00 for a flat nozzle and from 0.97 to 1.00 for a circular nozzle along 10 equally spaced lines around nozzle exits. The difference in calculated A_{33} component is not so enormous, but the fact that A_{33} component shows higher value in case of a circular nozzle reflects that there is more aligned distribution of fillers in case of a circular nozzle. In addition to that, velocity Y, velocity Z, and velocity X represents different extrusion for a circular and a flat nozzles. The aligned and random distribution of fillers depending on nozzle shapes can be understood by investigation of fluid movement. The fluid velocity graphs along equally spaced lines explain how fluid moves. The focus is especially on the nozzle exit because the movement of fluid at the nozzle exit will determine the orientation of fillers in printed samples.

After the nozzle exit ($Y = 0$), for the flat nozzle, filler alignment in Y direction is decreased as Y value is decreased due to two major changes. First, velocity Y (on average) decreases as the Y is decreased from positive to negative value. (The flat nozzle case shows steeper decreasing slope compared to the circular nozzle case). At the nozzle exit, the average of velocity Y of flat nozzle case is about 1.3 times higher than the average velocity Y

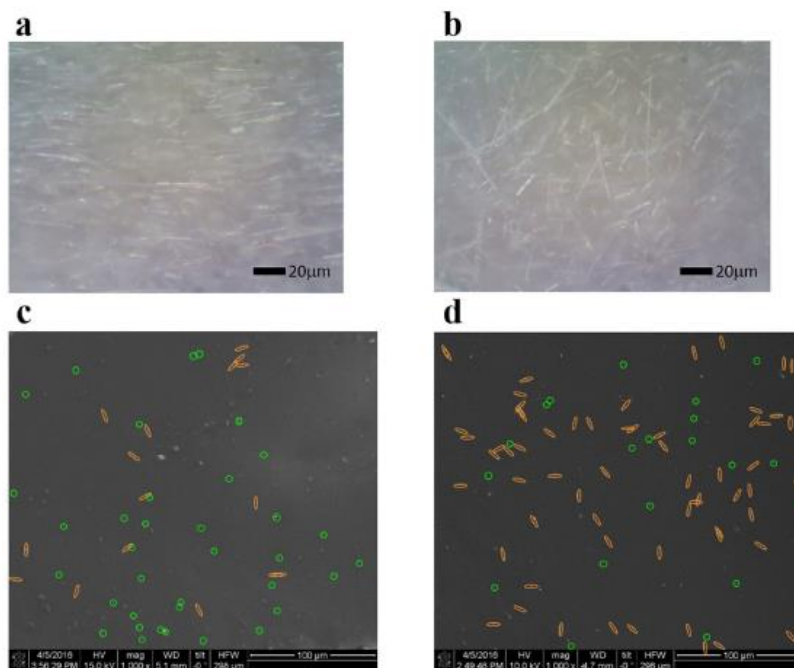


Figure 3. Filler distribution morphology. Optical microscope images of Print & Cure samples printed through a circular nozzle (a) and a flat nozzle (b) and SEM images of cross sections of samples printed through a circular nozzle (c) and a flat nozzle (d).

of circular case (7.7 & 5.8) Second, the absolute value of velocity Z and velocity X show the highest value near the nozzle exit. Fillers will be more likely moving along Z and X axis direction (Expansion flow)²¹ instead of aligning along extrusion direction.

On the other hand, a circular nozzle case shows lower absolute value of average velocity Z and average velocity X compared to flat nozzle at the nozzle exit. At the nozzle exit, the average of velocity Z of flat nozzle is about 17.1 times faster than the average of velocity Z of circular nozzle (1.025 & 0.06). The average of velocity X of flat nozzle is about 1.8 times faster than the average velocity X of circular nozzle (7.7 & 4.2). Over all, velocity graphs along 10 lines of the flat nozzle shows larger deviation (the difference between values of each graph from the average graph) compared to velocity graphs along 10 lines of the circular nozzle. This also explains the reason why flat nozzle samples show random distribution of AgNWs while the circular nozzle samples show aligned distribution of AgNWs.

Microscopic images in Fig. 3a,b show aligned and random distribution of AgNWs in P&C resin matrix depending on nozzle shapes. The sample printed with a circular nozzle shows aligned distribution of AgNWs (Fig. 3a). The sample printed with a flat nozzle shows random distribution of AgNWs (Fig. 3b). This was observed similarly in many areas of each sample. And this matches with the simulation result.

SEM images of the cross section of samples at in Fig. 3c,d show the difference between random and aligned AgNW orientation. In the aligned AgNWs sample printed with a circular nozzle, the cross section is showing many dots and smaller number of lines. This happens because AgNWs are aligned along the printing direction, and the cross section is perpendicular to this printing direction. AgNWs aligned to the printing direction will show dot images in cross section, while AgNWs randomly distributed will show line images. Only clear white dots or lines were counted, blurry larger dots or thicker lines were not counted. Thus, majority of AgNWs (~75%) are showing their cross section as dots at the cross section of the sample printed from a circular nozzle. On the other hand, the sample printed with a flat nozzle shows many lines (~75%) and smaller number of dots (~25%) because majority of AgNWs are lying with different angles at the cross section of the sample as a random distribution and are showing their surface of side as lines.

Dielectric permittivity was measured by R&S® ZND Vector Network Analyzer (VNA), connected with DAK-12 dielectric measurement system. Figure 4 compares the compensated permittivity which is the measured permittivity divided by the weight of each sample in order to compensate the difference of thickness of each sample. The area of each sample is the same. The thickness of a sample is proportional to the volume of a sample. Thus, we assumed there is a linear relationship between the thickness of samples and permittivity as the linear relationship between AgNW volume fraction and permittivity²⁶. The compensated permittivity of each samples was obtained by calculating permittivity of 1 gram sample using measured permittivity, sample weight, and the permittivity of perfect vacuum which is 1 as shown in the following equation (2).

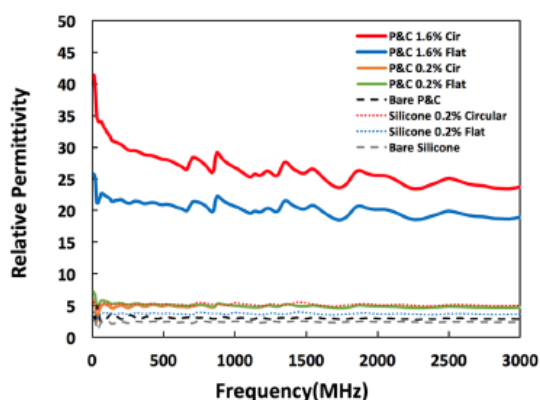


Figure 4. Permittivity of Print & Cure (AgNW vol. fraction: 0, 0.2, 1.6%) and Silicone (AgNW vol. fraction: 0, 0.2%) samples printed with a circular or a flat nozzle.

$$\text{Compensated permittivity} = (\text{Measured permittivity} - 1)/(\text{sample weight}) + 1 \quad (2)$$

where, measured permittivity is a relative permittivity ($\epsilon_r = \epsilon/\epsilon_0$).

For P&C 0.2% Flat and P&C 0.2% Circular (Cir) cases, there is not so much difference in permittivity. However, P&C 1.6% Cir case has about 30% higher permittivity compared to P&C 1.6% Flat case. This is because Cir has more alignment of AgNWs. These aligned AgNWs will make a lot of couples of two parallel AgNWs which will work like micro capacitors. The permittivity is the amount of charge required to apply 1 unit of electric flux in a medium. Higher dielectric permittivity means higher performance to resist an applied electric field and enables storing more electrical energy in a limited volume, which will be useful for energy storage devices³.

As a demonstration, a passive radio frequency identification (RFID) tag with temperature sensibility was designed to have a circuit and an antenna with a resonant frequency as 910 MHz which is compatible with the RFID reader (Fig. 5a). This RFID Antenna was printed by P&C system on a piece of 127 μm Polyimide (PI) film, Kapton[®] HPP film as shown in Fig. 5b. The antenna was printed with the P&C resin with 1.5 vol. % AgNWs through a flat nozzle so that the randomly distributed AgNWs in printed antenna form a conductive network. This antenna was put into an oven for annealing AgNWs at 200 $^{\circ}\text{C}$ for 10 minutes after printing to attain enhanced conductivity. The circuit part of the RFID tag was manufactured by printing an interconnection and soldering components on it. The interconnection was printed by a Printed Circuit Board (PCB) printer, Voltera V1, with an appropriate dimension for 0603 footprint electronic components and an RFID chip because the resolution of V1 printer met the printing requirement. SL900A as an RFID chip, 47 nH SMD inductor, and 2.2 μF SMD capacitor were soldered on the interconnection. The inductor placed between the RFID chip and antenna makes a large reading range, and the capacitor makes the signal smooth. This RFID tag was well identified by the RFID reader which is compatible with the North American UHF RFID band (902–928 MHz) within the distance up to 1 cm. And the temperature sensing information in the RFID chip was read successfully by the reader at three different temperature levels (Fig. 5c).

Conclusion

In this report, photo-curable 3D printing system has been designed to optimize the printing of a photo-curable nanocomposites composed of photo-curable resin and AgNWs. Specially, the permittivity difference has been observed from 3D printed samples with same concentration of AgNWs when they are 3D printed with different nozzles. The computational study confirms that the extrusion printing with a circular nozzle generates an aligned distribution of fillers, and the extrusion printing with a flat nozzle induces a random distribution of fillers. Utilizing the conductively percolated network realized by printing through a flat nozzle, an RFID antenna is fabricated. The antenna designed to have a resonant frequency as 910 MHz was printed on polyimide substrate for the demonstration of RFID communication and temperature sensing. Therefore, the study on the control of filler orientation in prints ushers the way to control composite material's electrical properties by nozzle shape dependent 3D printing. This can open a new platform of extrusion printing for controlling material's property by design of 3D printing parameters. The effect of nozzle diameters on overall properties will be investigated in future publications by additional experiment and parametric simulation. We expect that nozzle's larger diameter will generate enhanced alignment of AgNWs in case of a circular nozzle and more random distribution of AgNWs with a flat nozzle compared to smaller diameter nozzles because a larger diameter nozzle will allow more variation of local velocity across the cross section of the nozzle compared to a smaller diameter nozzle.

Materials and Methods

Photo-curable extrusion printing system - Print & Cure. 4 Laser diodes were mounted right beside the position of the printing nozzle in the printing head of extrusion printing system to conduct photo-curable extrusion printing. The wavelength of UV light of a diode is 405 nm, and the optical power of a diode is 120 mW.

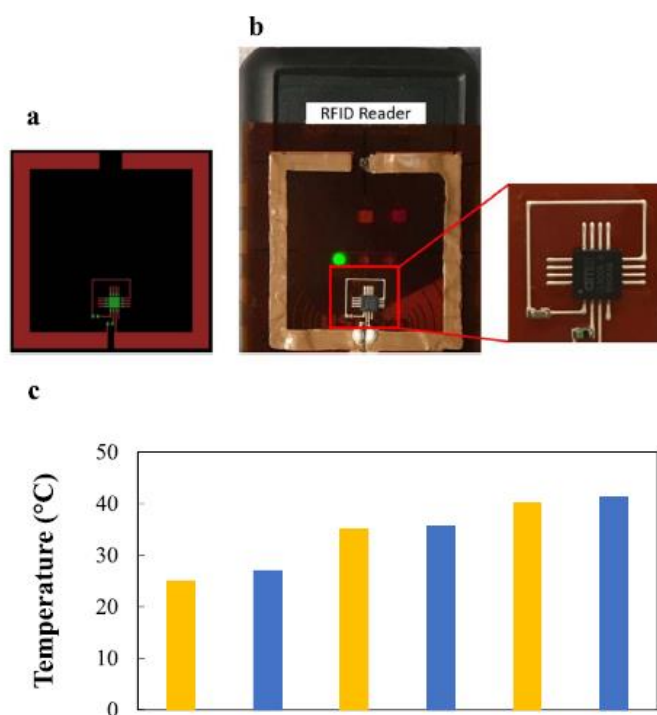


Figure 5. The RFID tag design and the detection of a fabricated RFID tag by an RFID reader. (a) Design of antenna and circuit layout (b) Detection of the RFID tag consisted of an antenna printed with AgNW (1.5% vol. fraction) and P&C resin composite through a flat nozzle and interconnected with an RFID chip (c) Temperature sensing result from 25 to 40 °C: yellow bars show heater's temperature (25, 35, and 40 °C) and, blue bars show corresponding temperature detected by the RFID tag (26, 35, and 41 °C).

To supply a stable 5 V DC voltage for each diode, drivers for diodes were made with a regulator 7805, two capacitors of 0.33 μ F and 10 μ F, and a resistor of 47 Ω . The power was supplied from the RamBo board of a delta FDM 3D printer (Orion, SeeMeCNC). A paste extrusion system (Discov3ry, Structur3d Printing) was modified to save printing material. Two syringes were connected by a tube which is filled with water in order to transfer the pressure from the primary syringe to the syringe at the extrusion side. The motor of Discov3ry extruder gives pressure to the primary syringe, and the pressure is transferred to the smaller syringe at the extrusion side.

Preparation of AgNW/P&C resin printed samples. AgNWs were prepared by polyol process which make AgNWs with high aspect ratio. The aspect ratio is about 200. The diameter and length of AgNWs are 100 nm and 20 μ m respectively. AgNWs are mixed with P&C resin which is made of an oligomer (Urethane triacrylate), a photo initiator (Phenylbis phosphine oxide), and a monomer (Methacrylic acid). Prepared composite material is mixed thoroughly by a vortex mixer and a magnetic stirrer. To study permittivity of AgNW/P&C resin, 4 samples are printed with two different nozzles and two different AgNW vol. fractions of 0.2% and 1.6%. Assuming that the percolation threshold of AgNWs is around 0.7% volume fraction based on our group's previous research with same AgNWs², Concentrations of 0%, 0.2%, and 1.6% volume fraction were chosen in order to compare three different cases such as pristine polymer matrix, PNC with AgNWs of volume fraction under the percolation threshold, and PNC with AgNWs of volume fraction over the percolation threshold.

Simulation of printing composite. Fluid models of composite material in a circular and a flat nozzle tips and extrudates are generated with the Solidworks. After fluid models are made, these geometry files are saved as parasolid format (.x_t). By using these parasolid files, meshes were created in a simulation software, Ansys Workbench (ANSYS, Inc.). After improving mesh quality by CFD (Computational Fluid Dynamics), models are analyzed through polyflow extrusion of the Ansys Workbench to find velocity profile of composite material. According to the mesh quality report, number of total elements of the circular nozzle case is 204222. Among these elements, 96% have quality value greater than 0.8227535. On the other hand, the flat nozzle case has a larger number of total elements, 666816 compared to the circular nozzle case. It's mainly because mesh elements in the shape transition part of the flat nozzle (from cylindrical to flat) should be refined enough to meet the convergence criteria. Among these elements, 86.3% have quality value greater than 0.8177935. 77.0% of elements have skew value less than 0.9295337 which is acceptable.

References

- Zhang, X. *et al.* Magnetoconductive Conductive Polyaniline–Barium Titanate Nanocomposites with Negative Permittivity. *J. Phys. Chem. C* **116**, 15731–15740 (2012).
- Park, J. S., Kim, T. & Kim, W. S. Conductive Cellulose Composites with Low Percolation Threshold for 3D Printed Electronics. *Sci. Rep.* **7**, 3246 (2017).
- Gao, J. *et al.* Designing High Dielectric Permittivity Material in Barium Titanate. *J. Phys. Chem. C* **121**, 13106–13113 (2017).
- Prateek, T. V. K. & Gupta, R. K. Recent Progress on Ferroelectric Polymer-Based Nanocomposites for High Energy Density Capacitors: Synthesis, Dielectric Properties, and Future Aspects. *Chem. Rev.* **116**, 4260–4317 (2016).
- Wang, G., Huang, Y., Wang, Y., Jiang, P. & Huang, X. Substantial enhancement of energy storage capability in polymer nanocomposites by encapsulation of BaTiO₃ NWs with variable shell thickness. *Phys. Chem. Chem. Phys.* **19**, 21058–21068 (2017).
- Patton, S. T. *et al.* Multiphysics characterization of multi-walled carbon nanotube thermoplastic polyurethane polymer nanocomposites during compression. *Carbon* **98**, 638–648 (2016).
- Kim, P. *et al.* Phosphonic Acid-Modified Barium Titanate Polymer Nanocomposites with High Permittivity and Dielectric Strength. *Adv. Mater.* **19**, 1001–1005 (2007).
- Zhang, X., He, Q., Gu, H., Wei, S. & Guo, Z. Polyaniline stabilized barium titanate nanoparticles reinforced epoxy nanocomposites with high dielectric permittivity and reduced flammability. *J. Mater. Chem. C* **1**, 2886–2899 (2013).
- Madusanka, N. *et al.* Nanocomposites of TiO₂/cyanoethylated cellulose with ultra high dielectric constants. *Nanotech.* **27**, 195402 (2016).
- Kumar, G. S., Vishnupriya, D., Chary, K. S. & Patro, T. U. High dielectric permittivity and improved mechanical and thermal properties of poly(vinylidene fluoride) composites with low carbon nanotube content: effect of composite processing on phase behavior and dielectric properties. *Nanotech.* **27**, 385702 (2016).
- Zeraati, A. S., Arjmand, M. & Sundararaj, U. Correction to "Silver Nanowire/MnO₂ Nanowire Hybrid Polymer Nanocomposites: Materials with High Dielectric Permittivity and Low Dielectric Loss". *ACS Appl. Mater. & Inter.* **9**, 32412–32412 (2017).
- Arbatti, M. *et al.* Ceramic-Polymer Composites with High Dielectric Constant. *Adv. Mater.* **19**, 1369–1372 (2007).
- Hu, N., Karube, Y., Yan, C., Masuda, Z. & Fukunaga, H. Tunneling effect in a polymer/carbon nanotube nanocomposite strain sensor. *Acta Mater.* **56**, 2929–2936 (2008).
- Sun, Y., Mayers, B., Herricks, T. & Xia, Y. Polyol Synthesis of Uniform Silver Nanowires: A Plausible Growth Mechanism and the Supporting Evidence. *Nano Lett.* **3**, 955–960 (2003).
- Arjmand, M., Moud, A. A., Li, Y. & Sundararaj, U. Outstanding electromagnetic interference shielding of silver nanowires: comparison with carbon nanotubes. *RSC Adv.* **5**, 56590–56598 (2015).
- Compton, B. G. & Lewis, J. A. 3D Printing: 3D-Printing of Lightweight Cellular Composites (Adv. Mater. 34/2014). *Adv. Mater.* **26**, 6043–6043 (2014).
- Tjong, S. C. Polymer nanocomposite bipolar plates reinforced with carbon nanotubes and graphite nanosheets. *Ener. & Env. Sci.* **4**, 605–626 (2011).
- Martin-Gallego, M., Lopez-Manchado, M. A., Calza, P., Roppolo, I. & Sangermano, M. Gold-functionalized graphene as conductive filler in UV-curable epoxy resin. *J. Mater. Sci.* **50**, 605–610 (2014).
- Du, F., Fischer, J. E. & Winey, K. I. Effect of nanotube alignment on percolation conductivity in carbon nanotube/polymer composites. *Phys. Rev. B* **72**, 121404 (2005).
- Tang, H., Malakooti, M. H. & Sodano, H. A. Relationship between orientation factor of lead zirconate titanate nanowires and dielectric permittivity of nanocomposites. *Appl. Phys. Lett.* **103**, 222901 (2013).
- Heller, B. P., Smith, D. E. & Jack, D. A. Effects of extrudate swell and nozzle geometry on fiber orientation in Fused Filament Fabrication nozzle flow. *Add. Man.* **12**, 252–264 (2016).
- Lebel, L. L., Aissa, B., Khakani, M. A. E. & Theriault, D. Ultraviolet-Assisted Direct-Write Fabrication of Carbon Nanotube/Polymer Nanocomposite Microcoils. *Adv. Mater.* **22**, 592–596 (2010).
- Cooperstein, I., Layani, M. & Magdassi, S. 3D printing of porous structures by UV-curable O/W emulsion for fabrication of conductive objects. *J. Mater. Chem. C* **3**, 2040–2044 (2015).
- Verweyst, B. E. & Tucker, C. L. Fiber Suspensions in Complex Geometries: Flow/Orientation Coupling. *The Canadian J. Chem. Eng.* **80**, 1093–1106 (2002).
- Cross, M. M. Rheology of non-Newtonian fluids: A new flow equation for pseudoplastic systems. *J. Coll. Sci.* **20**, 417–437 (1965).
- Mi, H.-Y., Li, Z., Turng, L.-S., Sun, Y. & Gong, S. Silver nanowire/thermoplastic polyurethane elastomer nanocomposites: Thermal, mechanical, and dielectric properties. *Mater. & Des.* **56**, 398–404 (2014).

Author Contributions

T.K. and W.S.K. conceived the idea, designed the research and the experiments; T.K. led experiments with assistance from R.T.; T.K. fabricated and characterized sensors; R.T. designed and assembled RFID; W.S.K. contributed to data analysis and interpretation. T.K., R.T. and W.S.K. wrote the paper and all authors provided feedback.

Additional Information

Competing Interests: This work received support from the Discovery Accelerator Supplement Grant 493028-2016, funded by the Natural Sciences and Engineering Research Council of Canada (NSERC).

Publisher's note: Springer Nature remains neutral with regard to jurisdictional claims in published maps and institutional affiliations.



Open Access This article is licensed under a Creative Commons Attribution 4.0 International License, which permits use, sharing, adaptation, distribution and reproduction in any medium or format, as long as you give appropriate credit to the original author(s) and the source, provide a link to the Creative Commons license, and indicate if changes were made. The images or other third party material in this article are included in the article's Creative Commons license, unless indicated otherwise in a credit line to the material. If material is not included in the article's Creative Commons license and your intended use is not permitted by statutory regulation or exceeds the permitted use, you will need to obtain permission directly from the copyright holder. To view a copy of this license, visit <http://creativecommons.org/licenses/by/4.0/>.

© The Author(s) 2018

Appendix B.

Journal paper discussed in Chapter 4 and 5

3D Printed Disposable Wireless Ion Sensors with Biocompatible Cellulose Composites

Note: Used with permission from WILEY-VCH Verlag GmbH & Co. KGaA, Weinheim. This article was published in [Kim, T., Bao, C., Hausmann, M., Siqueira, G., Zimmermann, T., & Kim, W. S. (2019). Electrochemical Sensors: 3D Printed Disposable Wireless Ion Sensors with Biocompatible Cellulose Composites (Adv. Electron. Mater. 2/2019). *Advanced Electronic Materials*, 5(2), 1970007. doi:10.1002/aelm.201970007]

3D Printed Disposable Wireless Ion Sensors with Biocompatible Cellulose Composites

Taeil Kim, Chao Bao, Michael Hausmann, Gilberto Siqueira, Tanja Zimmermann, and Woo Soo Kim*

As the wireless communication technologies are becoming more crucial for internet-of-things (IoT) electronic devices, sensors have also been equipped with wireless data collection. A conventional way to make wireless sensor systems is to develop active sensor devices with silicon-based chip technologies integrated with an amplifier, a battery, a converter, among others. However, it is difficult to generate disposable inexpensive flexible sensors with all these rigid components. Here, 3D printed disposable wireless ion selective sensor systems with unique form factors, high sensitivity, and flexibility are reported. A 3D printable conductive ink is designed and optimized with cellulose nanofibers by addition of silver nanowires for sustainable and biocompatible sensor applications. Polyimide film which has high surface hydrophobicity is used as a substrate for better resolution of printing. The 3D printed wireless sensor system includes inductor–capacitor circuits, and ion selective membrane electrodes, which can detect quantitative ion concentrations selectively. The change of ion concentrations is detected by measuring the magnitude of S_{11} , reflective coefficient at the resonant frequency of 2.36 GHz using a vector network analyzer. The demonstrated sensitivity is 3.4%/m for ammonium ion (NH_4^+).


Recently, wood-derived cellulose materials which are flexible, recyclable, biocompatible, and low-cost gain significant attention for sustainable and eco-friendly manufacturing of electronic devices.^[1–3] Representative sustainable nanocellulose materials like cellulose nanofibers (CNFs) and cellulose nanocrystals (CNCs) have been used as primary constituent materials for additive manufacturing.^[4–6] Both CNCs and CNFs are mainly utilized as 3D printable ink materials for direct ink writing (DIW) based 3D printing technologies.^[7,8] Specially, conductive cellulose inks which include conductive fillers such as graphene and carbon

nanotubes have been also demonstrated as conductive inks for 3D printed electronic devices.^[9,10] Cellulose has been used as substrates as well as the matrix of conductive inks.^[11,12] Some cellulose inks have been investigated for biomedical applications thanks to their biocompatibility.^[13] Recent development for cellulose inks have provided methods to deal with important volume shrinkage resulting from the drying and evaporation of the dispersing solvent.^[14] In order to make a reliable 3D printable ink, the relevance of understanding parameters such as the rheological properties (controlling the printability)^[15] and the conductivity was evidenced by previous research.^[16] Rheological aspects involve a shear-thinning behavior and the existence of a yield stress to enable a proper extrusion and shape fidelity of prior and after 3D printing.^[17] The conductivity of the ink can be controlled by the addition of conductive fillers such as silver flakes, silver nanowires (AgNWs) as earlier research suggested.^[18,19]

Among other electrochemical sensor platforms, ion selective membrane sensors have been reported as efficient tools to detect ion analytes selectively from ion mixed solutions such as pH,^[20–23] glucose,^[24] or urea.^[25] Furthermore, by integrating with Field Effect Transistors (FETs), the analyte information is quantitatively analyzed using Ion Selective Field Effect Transistors (ISFETs).^[26–28] Recyclable ISFETs based on oxide semiconductors were also studied for sustainability.^[29] High selectivity and stability enable ISFETs to be investigated for potential applications in biomedical and environmental fields. ISFETs are mainly controlled by the generated potential from ion selective electrodes and the generated potential influences the electrical performance of FETs. Therefore, variation of ion concentration is reflected by the fluctuation of drain current, drain voltage, or output voltage. Specially, wireless ion selective sensors are demonstrated to extract remotely ion concentration signals out of analyte solution. Consequently, a great interest was demonstrated over the past years in the fields of real-time monitoring and internet-of-things (IoT) applications. Research was conducted in integrating novel wireless technologies, such as RFID,^[30–34] Bluetooth,^[35,36] Zigbee,^[37] or NFC^[38] together with electrochemical sensors for wireless analytes information recovery. A conventional approach for wireless sensing with silicon-based chip technology has been already developed.^[31]

T. Kim, C. Bao, Prof. W. S. Kim
 School of Mechatronic Systems Engineering
 Simon Fraser University
 Surrey V3T 0A3, BC, Canada
 E-mail: woosook@sfu.ca

M. Hausmann, Dr. G. Siqueira, Dr. T. Zimmermann
 Swiss Federal Laboratories for Materials
 Science and Technology (EMPA)
 Applied Wood Materials Laboratory
 Dübendorf 8600, Switzerland

 The ORCID identification number(s) for the author(s) of this article can be found under <https://doi.org/10.1002/aeml.201800778>.

DOI: 10.1002/aeml.201800778

Here, we report different properties of nanocellulose-based inks composed of AgNWs as conductive fillers and CNFs or CNCs as matrix materials. If the weight ratio of AgNWs in the conductive ink is higher than the percolation threshold, AgNWs make a conductive 3D network. These conductive inks can be used for 3D printing of sensing devices. Also, different 3D printing behaviors of CNF-AgNW ink and CNC-AgNW ink are discussed. After confirming 3D printing capability of CNF-AgNW ink on 3D objects, 3D printed inductor–capacitor (LC) circuits with CNF-AgNW ink are demonstrated. Finally, we report a wireless sensing solution using the ion-selective inductor–capacitor circuits (IS-LC). This novel technology opens a new platform technology for wireless ion detection quantitatively. This is the first demonstration to develop a wirelessly detectable ion sensor consisted of an ion selective membrane electrode (ISME)^[39] integrated with an LC circuit. This is much simpler compared to a battery powered wireless ion sensing system. This LC + ISME circuit is designed to work as an LC sensor, which can be detected at its resonant frequency by the loop antenna connected to the port of vector network analyzer (VNA).^[40] The fabricated sensor demonstrated detection of different concentration of ammonium (NH₄⁺) ion which is among the most important indicators for the metabolism of human body. This platform will be useful for the analysis of remotely detectable ions. Furthermore, the 3D printed sensor systems developed in this study are light-weight, flexible, disposable, and biocompatible with highly 3D curvilinear form factors.

The conductivity of 3D printable inks is strongly dependent on mixing condition between matrix and fillers. To investigate the contribution of matrix material to the percolation of AgNWs and to the formation of a conductive network, CNF-AgNW and CNC-AgNW inks with different AgNW weight ratio are printed on glass slides. The glass slides are considered as appropriate substrates for printing flat and straight lines to access the conductivity by measuring the resistivity of printed inks. Our results demonstrate that AgNWs are randomly distributed in the printed CNF-AgNW ink but aligned in the printed CNC-AgNW ink, as observed in Figure 1. The main reason for the different arrangement of AgNWs is attributed to different interaction between nanocellulose materials and AgNWs during the extrusion processes, so the inks can experience different shear stresses within the nozzles. This difference in interaction comes from the differences in dimension, morphology, and entanglement of NFCs and CNCs. Figure 1a describes randomly distributed AgNWs in 3D printed CNFs which maintain the original random distribution after the extrusion through a nozzle. The same randomly distributed AgNWs are observed by optical microscopy analysis as shown in Figure 1c. An atomic force microscopy (AFM) image (Figure S2a, Supporting

Information) also show a rough surface of CNF matrix which was captured from the entangled structure of CNFs. The entangled CNF structure helps AgNWs maintain the random distribution after extrusion for better percolation. On the other hand, Figure 1b shows how randomly distributed AgNWs in CNCs are aligned along the printing direction after the extrusion from a nozzle. Figure 1d confirms that CNCs do not contribute to the percolation of AgNWs but induces the alignment of AgNWs along the printing direction. AgNWs prepared for this study have a rod-like shape with a diameter of 55 nm and length of 10 μm on average.^[41] CNCs used in this study also have a rod-like shape with a diameter of 6 nm and length of 120 nm. However, the aspect ratio of AgNW (181.8) is 6 times higher than that of CNC (20).^[6] On the other hand, the CNFs have a flexible fiber shape like spaghetti noodles with a diameter of 100 nm and a length in the order of 2 μm. In case of 30 wt% AgNWs inks, there are about 15 AgNWs and 1611812 CNCs per 5 picograms of CNC-AgNW ink and about 15 AgNWs and 350 CNFs per 5 picograms of CNF-AgNW ink.

It has been reported that the fillers in the shape of rigid rods are aligned along the streamlines of the flow of the polymer matrix.^[42] The changing velocities of matrix across the cross section of a printing nozzle generate the axial and radial driving force for fiber rotation along the length of the fiber.^[42] If it is assumed that the potential for rotation is based on the different values of velocity at both ends of a fiber, the rate of rotation is given as the following equation.^[42]

$$\frac{d\theta}{dt} = \beta \frac{\Psi(\theta, t)}{L} \quad (1)$$

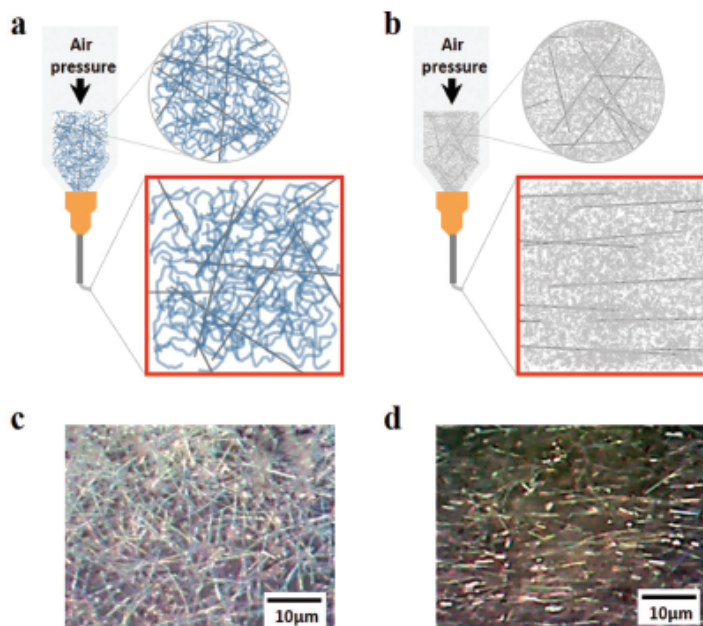


Figure 1. Comparison of printed CNF-AgNW ink and CNC-AgNW ink. a) Schematic of printed CNF-AgNW ink. b) Schematic of printed CNC-AgNW ink. c) Microscopic images of printed ink of 36 wt% AgNW in CNF. d) Microscopic images of printed ink of 30 wt% AgNW in CNC.

where $\Psi(\theta, t)$ is the difference between values of velocity at both ends of a fiber. β is a correction factor for the nonlinear variation of velocities along the length of the fiber and is given as the following equation. β is important only if the aspect ratio L/D of fiber is large.^[42]

$$\beta = \frac{1}{2} \ln \left[\left(\frac{L}{D} \right) - 1 \right] \quad (2)$$

A concentrated suspension of rigid fibers in viscous fluid can be aligned by a simple shear flow.^[43] As CNCs are in a rod-like shape, a given shear stress aligns CNCs and results in a nematic phase.^[44] In concentrated suspensions, CNCs form a liquid crystalline phase with a chiral nematic order. CNCs are reported to be aligned in a similar parallel way.^[45,46] AgNWs, typical anisotropic fillers with high aspect ratio, can be aligned according to the printing direction during the extrusion printing process.^[47] The alignment of CNCs along the printing direction in extrusion is also reported.^[7] Lots of researches on aligning CNC nanocomposites were done to improve mechanical properties of polymer matrices. AgNWs in CNC matrix can be aligned along the printing direction when the matrix material experiences the shear stress during the extrusion through a nozzle. CNF-AgNW ink and CNC-AgNW ink are subjected to the same shear stress while they are passing through printing nozzles. However, because of the flexibility of CNFs, the matrix forms an entangled web-like network structure with a higher aspect ratio, acting like a net, restricting the free rotation or movement of AgNWs inside. In contrast, CNCs present a rod-like shape similar to whiskers with a lower aspect ratio, which works like a media where AgNWs rotate and move easily. As shear stress induces CNCs to be aligned along the printing direction, AgNWs are dragged along and tend to align with the flow.

The resistivity of 3D printed CNF-AgNW has been demonstrated in Figure 2a. CNF-AgNW ink shows reliable conductivity after 3D printing through nozzle due to its percolation of randomly distributed AgNWs. The resistivity of the optimized CNF-AgNW ink is $9.13 \times 10^{-5} \Omega \text{m}$, which results in conductivity of $1.10 \times 10^4 \text{ S m}^{-1}$ of conductivity as shown in Figure 2a, which is similar to the reported value.^[48] Contrarily, the printed ink of 30–36 wt% AgNW in CNC-AgNW did not show any conductivity. For the demonstration of 3D printability of CNF-AgNW ink, a 3D shaped spiral antenna on the surface of a hemisphere is designed as shown in Figure 2b. Figure 2c shows the printed 3D antenna on a 3D hemisphere which has a diameter of 42.5 mm. Figure 2d shows the resonant frequency of the 3D antenna at 2.48 GHz where the magnitude of S_{11} shows the minimum, and the real part of impedance, $\text{Re}(Z_{in})$ shows the maximum.^[49] The printability of CNF-AgNW ink is confirmed by measurement of storage modulus

(G'), loss modulus (G''), and viscosity. The measurement of G' and G'' shows high G' and elastic behavior at low shear stress ($G' > G''$) (Figure S3a, Supporting Information). This condition enables better printability through a rapid solidification after printing.^[7,50] A shear-thinning behavior is observed from Figure S3b in the Supporting Information where the viscosity decreases by several orders of magnitude as the shear rate increases from 9.93×10^{-4} to 1000 s^{-1} .

As the sensitivity of a sensor is closely related to the Q factor, a parametric study of LC design to improve the Q factor was done through a simulation and also studied by experiment. Figure 3a,b illustrates the design of LC circuits in series where inductor (I) and capacitor (C) have different heights. The difference of height was obtained by increasing the number of printed layers by 2 from 2 to 8. C1, C2, C3, and C4 contain interdigitated capacitors (IDCs) with 2, 4, 6, and 8 printed layers, respectively and contain an inductor of 2 printed layers in common. I1, I2, I3, and I4 contain inductors with 2, 4, 6, and 8 layers, respectively and contain an IDC of 2 printed layers in common. A total of eight combinations were prepared (Figure S4a, Supporting Information). The thickness of layers is exaggerated for better understanding of the structure in Figure 3a,b. Figure 3c is obtained from the simulation on how thickness change the maximum of the real part of input impedance ($\max(\text{re}(Z_{in}))$). Here the thickness of LC shows a positive correlation with the $\max(\text{re}(Z_{in}))$. Especially, the thickness of spiral inductor shows stronger effect to $\max(\text{re}(Z_{in}))$ compared to that of IDC at a higher thickness range. The graph in Figure 3d is the experimental result that shows how thickness change the

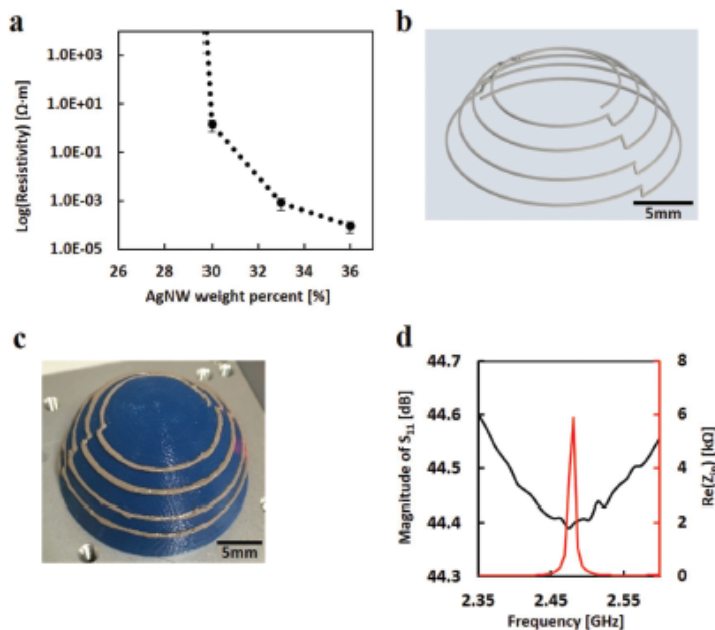


Figure 2. Resistivity and printable properties of CNF-AgNW ink. a) Resistivity of CNF-AgNW ink. b) 3D printing schematics of an antenna. c) 3D printed antenna on a hemisphere. d) Corresponding graphs of magnitude of reflection coefficient S_{11} (black) and the real part of input impedance depending on frequency (red).

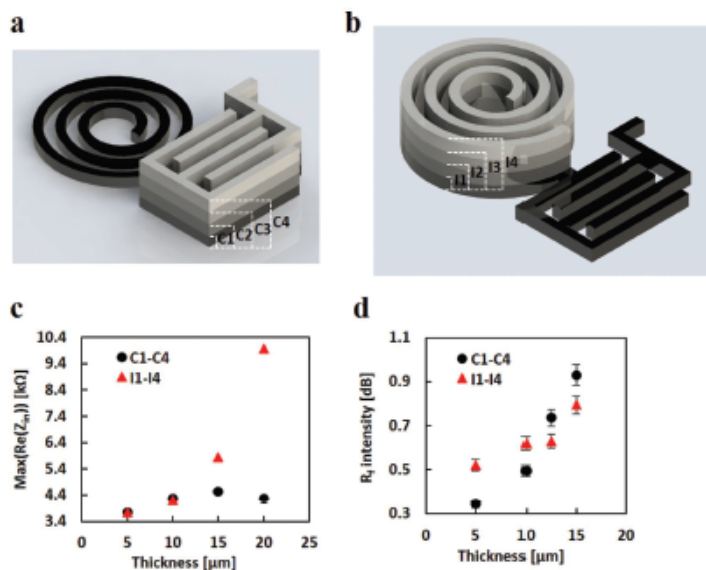


Figure 3. Q factor depending on LC thickness. a) Design of LC circuit with different height of IDC. b) Design of LC circuit with different height of inductor. c) Simulation result for the $\max(\text{Re}(Z_{\text{in}}))$ depending on the thickness of IDC or inductor. d) Experiment result of resonant frequency intensity depending on the thickness of IDC or inductor.

resonant frequency (R_f) intensity at the resonant frequency of LC circuits. R_f intensity is defined as the difference between the magnitude of reflection coefficient S_{11} and a reference value, 45.1 dB at the resonant frequency. As shown in Figure S4b in the Supporting Information, the thickness of LC was proportional to the number of printing layers up to four layers. However, the thickness of LC was not linearly proportional to the number of printing layers over six layers because the ink is not fully stacking in vertical direction but also expanded in horizontal direction. However, this result shows a positive correlation between the thickness of the I or C and R_f intensity. This shows that Q factor of this LC circuit printed with CNF-AgNW ink can be improved by increasing the number of printing layers of either the inductor or the capacitor. Adding layers on top of the previously printed layer increases the probability of making a better conductive percolation network in the final structure. Thus, multilayers of LCs can be applied to IS-LC to improve the sensitivity of electrochemical sensing. The quality factor, Q of LC sensor is given as following equation.^[50]

$$Q = \frac{1}{R_s} \sqrt{\frac{L_s}{C_s}} \quad (3)$$

where R_s is the resistance, L_s is the inductance, C_s is the capacitance of LC sensor.^[50]

If the real part of the input impedance, $\text{Re}(Z_{\text{in}})$ of an LC sensor has a sharper peak, its Q factor is improved. The maximum of the real part of Z_{in} of an LC sensor can be described as the following equation.^[50]

$$Z_{\text{in,max}} = \text{Re}(Z_{\text{in}})_{\text{max}} / f - f_0 = 2\pi f_0 I_0 k^2 Q \quad (4)$$

The resonant frequency f_s can be found from the maximum of $\text{Re}(Z_{\text{in}})$. In normal circumstances, $f_{\text{max}}(\text{Re})$ is approximately considered as f_s .^[50]

The Q factor of LC sensor depends on the resistance of LC sensor as shown in Equation (3). In general, higher Q factor is obtained from a sharper peak which comes with a larger R_f intensity. Thus, the Q factor as well as the R_f intensity will be changed if the resistance of the IS-LC circuit is changed due to the change of ion concentration applied to the ISME. The primary ion of an ion selective membrane is the ion which is targeted to be selectively detected by the membrane, while nonprimary ions are all other interference ions different from the primary ion. An ISME will have a lower resistance if the relevant primary ions are dropped on top of it compared to the cases of nonprimary ions because primary ions can move through the relevant selective membrane while nonprimary ions cannot. Studies on the dependence of resistance of ion selective electrodes on the solution concentration show the bulk resistance of the membranes decreases over the increase of ion concentrations.^[51,52] If the concentration of dropped

primary ions on ISME increases, the resistance of ISME decreases. This reduced resistance of ISME decreases the total resistance of IS-LC sensor as the resistance of ISME and LC circuit are in series as shown in the equivalent circuit of Figure S5 in the Supporting Information. Then, Q factor which is inversely proportional to the resistance of IS-LC (Equation (3)) is increased. And eventually, R_f intensity is increased, too. Thus, wireless sensing of the different ion concentrations is possible by measuring R_f intensity change of IS-LC sensor at the resonant frequency. The change of ion concentrations on IS-LC sensor was detected by measuring the magnitude of S_{11} , the reflective coefficient of S_{11} reflection method, at the resonant frequency of ISME + LC circuit (2.36 GHz) using a VNA. While the radio frequency (RF) power from VNA travels through the loop antenna connected to VNA port as shown in Figure 4a, ISME + LC circuit resonates the most at its resonant frequency, and the returned signal of VNA shows a dip at the resonant frequency.

Figure 4a describes the experimental set up for the wireless detection of ions through the 3D printed IS-LC sensor. The sensor is composed of a 10 μm thick series LC circuit and a sensor of 0.3 mm thick ISME as shown in Figure 4b. For the LC circuit, same layers of LC pattern were printed vertically 4 times, resulting in 10 μm in thickness. This is the maximum printable thickness without lateral margins. Regarding IS part, the thickness was chosen as the single printed layer's thickness of 0.3 mm of 3D printer which showed acceptable conductivity. A VNA was used to find the R_f intensity change depending on different ion concentrations. As the concentration of NH_4^+ , K^+ , and Ca^{2+} ions increases from 0.5 to 2 M, the R_f intensity at the resonant frequency also changes. However,

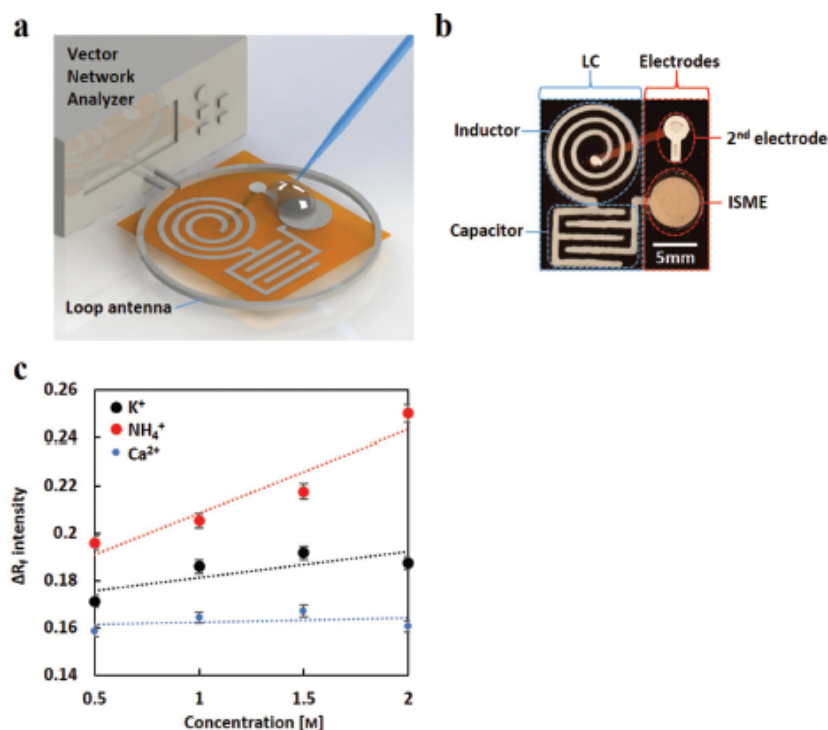


Figure 4. Wireless ion detection system. a) Schematic of IS-LC sensor design and loop antenna with VNA. b) Printed sample of IS-LC sensor. c) Experimental result of IS-LC sensor with NH_4^+ membrane.

there was no shift of the resonant frequency. The graph of NH_4^+ in Figure 4c shows the sensitivity of IS-LC sensor. Here ΔR_f intensity is defined as $(R_f \text{ intensity} - \text{initial } R_f \text{ intensity}) / (\text{initial } R_f \text{ intensity})$. A strong linear relationship between NH_4^+ ion concentration and ΔR_f intensity with a slope of 0.0349 and R^2 value greater than 0.91 demonstrates well the sensitivity of the NH_4^+ membrane. In other words, if we know the ΔR_f intensity value, we can estimate the concentration of primary ion through a calibration. When the concentration of primary ion changes by 1 M, NH_4^+ sensor shows 3.4% change in ΔR_f intensity. Furthermore, graphs for three different ions in Figure 4c demonstrate the selectivity of this IS-LC sensor. The ΔR_f intensity shows a strong linear relationship only with the concentration of NH_4^+ ion. Linear regressions of ΔR_f intensity depending on K^+ or Ca^{2+} ion concentration show lower slope values (-0.0109 and 0.0019 , respectively) and smaller R^2 values (0.6181 and 0.0997 , respectively) compared to the NH_4^+ case. The NH_4^+ selective membrane has pores for NH_4^+ ions. Thus, the NH_4^+ membrane become charged with NH_4^+ ions when the solution with NH_4^+ ions is placed on top of it. If the concentration of NH_4^+ ion is increased, more pores are charged with NH_4^+ ions, and the R_f intensity is increased showing a strong linear relationship. However, the R_f intensity does not have a strong linear relationship with the concentration of nonprimary ions such as K^+ or Ca^{2+} . Thus, the NH_4^+ selective membrane shows the selectivity of NH_4^+ as a primary ion. Figure S7 in the Supporting Information shows relation between ΔR_f intensity

and ion concentration in lower ion concentrations from 0.001 to 0.5 M. It shows a stronger linear relationship in case of NH_4^+ ion with higher slope value: 0.0049 and higher R^2 value as 0.93, compared to the case of K^+ ion with lower slope 0.0022 and lower R^2 value as 0.86 with the logarithmic scale on the x-axis.

The present work reports optimizing and 3D printing of conductive biocompatible ink where the cellulose materials play an important role as a constituent material which affects the distribution and arrangement of AgNWs a lot. Although both CNC-AgNW and CNF-AgNW based inks show sufficient 3D printability with shear-thinning behavior, 3D printed CNF-AgNW ink shows significantly better conductivity compared to 3D printed CNC-AgNW ink for the same wt% of AgNWs. The main cause of this difference in conductivity is that AgNWs are aligned in 3D printed CNC-AgNW ink and randomly distributed to make a conductive network in 3D printed CNF-AgNW ink, which was confirmed by optical microscopy and AFM results.

To develop an LC sensor with a higher sensitivity, improving Q factor is required. Q factor depends on inductance and capacitance of LC which are usually determined by the dimensions and material properties of inductor and capacitor. Even though the modeling of spiral inductors and IDCs are well established, and the inductance and the capacitance may be calculated from established equations using dimensions and material properties of the LC,^[50] LC circuits printed with CNF-AgNW ink of this study have very thin layers of inductor and IDC which have thickness in the order of 10 μm . Therefore, a parametric study

on the thickness of LC circuits was simulated and investigated by the experiment to understand how to obtain the best performance from 3D printed CNF-AgNW LC sensor.

Using the optimized CNF-AgNW ink, a wirelessly detectable ion sensor was fabricated with 3D printed LC circuit and ISME. This IS-LC sensor was designed to show the selectivity of NH_4^+ ion. The change of ion concentrations on IS-LC sensor was wirelessly detected through VNA by measuring the magnitude of reflection coefficient S_{11} and obtaining R_f intensity at the resonant frequency of the sensor; 2.36 GHz. We found that this IS-LC sensor shows high selectivity of NH_4^+ ion. This IS-LC sensor with NH_4^+ ion membrane also shows high sensitivity of 3.4%/ μM change in R_f intensity with the NH_4^+ ion concentration. The resistivity of the optimized CNF-AgNW ink is $9.13 \times 10^{-5} \Omega\text{m}$ ($1.10 \times 10^4 \text{ S m}^{-1}$ of conductivity). The resistivity of printed inductor and IDC part is measured to be $7.58 \times 10^{-4} \Omega\text{m}$ ($1.32 \times 10^3 \text{ S m}^{-1}$ of conductivity). This IS-LC sensor shows the potential as a disposable and flexible application since it has only 1.2 mg of printed CNF-AgNW ink for an LC circuit on a flexible polyimide (PI) film. To our best knowledge, this is the first report on wireless detection of selective ions from an ISME integrated with an LC circuit. This 3D printed light-weighted, flexible, disposable, and biocompatible sensor with high sensitivity and selectivity will open a path to realize wearable ion sensors for IoT and wireless monitoring.

Experimental Section

Preparation of CNF-AgNW and CNC-AgNW Ink: AgNWs were synthesized by a polyol method to generate high aspect ratio AgNWs with a diameter of 50 nm and an average length of 10 μm . Purified AgNWs were dispersed in deionized (DI) water by using a vortex mixer and an ultrasonicator (Ultrasonic Bath model 2510, Branson). AgNW ink was thoroughly mixed with CNF gel which has 1.04 wt% CNF in DI water. CNF-AgNW ink was prepared by evaporating DI water of the mixture using a rotary evaporator (Rotavapor R-300, BUCHI). After the evaporation, the ink was mixed at 1350–1500 rpm for 3 min by a speed mixer (SpeedMixer DAC150.1 FVZ-K, FlackTek, Inc.) for improved homogeneity. CNC-AgNW ink was prepared in a similar procedure. To find the percolation threshold of CNF-AgNW nanocomposite ink, five samples were prepared with different AgNW concentration of 18, 24, 30, 33, and 36 wt%. Printed samples were thermally annealed in an oven at 160 $^\circ\text{C}$ for 30 min.

Preparation of Ion Detectable Sensor: 4 layers of a spiral inductor and an IDC were printed with CNF-AgNW ink through a nozzle with 300 μm diameter on a piece of PI film by a 3D printing system (SHOT mini 100Sx and ML-808GX, Musashi Engineering, Inc.). This printed LC circuit was air-dried at ambient conditions. The resistivity of this LC circuit was measured to be $7.58 \times 10^{-4} \Omega\text{m}$. As shown in Figure 4b, printed ISME was directly connected to the IDC. And the second electrode was also printed to prevent the interference or damage of LC circuit while applying ion solutions to the ISME. Two via holes were made at the center of the inductor and the second electrode. A connection line was printed on the other side of the PI film to connect the inductor and the second electrode. Membrane solution was dropped on top of the ISME after cooling down to make a membrane for the primary ion (NH_4^+).

Characterization: Microscopic images of printed CNF-AgNW ink and CNC-AgNW ink were obtained by microscope NJF-120A with 10X objective lens (HINOTEK, China) and captured by a software, ScopeImage 9.0. The surface morphology of CNF-AgNW ink and CNC-AgNW ink was studied by using Park systems XE-100 AFM. The resistivity of printed sample of CNF-AgNW ink was calculated from the measurement of resistance of printed sample by using an LCR meter

(E4980A High Precision LCR Meter, Agilent Technologies). R&S ZND Vector Network Analyzer was used to measure magnitude of reflection coefficient S_{11} and find R_f intensity. Three IS-LC sensor samples showed the same results that the primary ion's detection was more linear response with the highest R^2 value and the highest slope in the R_f intensity versus ion concentration graphs. The graphs in Figure 4c,d represent the measurement of the last sample. The standard deviation of the response curve of this ISME was found to be less than 1% in the range of ion concentration from 0.001 to 1 μM .

LC Simulation: The change of the $\text{max}(\text{re}(Z_{in}))$ depending on the thickness of IDC or inductor was investigated by a simulation. Computer aided design (CAD) models were developed according to different thickness of LC as shown in Figure 3a,b and simulated by high frequency structure simulator (HFSS) of ANSYS to find the real part of the input impedance depending on frequency. The frequency sweep was done at 451 points from 0.25 to 3 GHz. The maximum value of the real part of input impedance was obtained for each case of different thickness of IDC or inductor from the result plots of the real part of input impedance versus frequency.

Supporting Information

Supporting Information is available from the Wiley Online Library or from the author.

Acknowledgements

This work received partial supports from the Discovery Accelerator Supplement Grant493028-2016 funded by the Natural Sciences and Engineering Research Council of Canada (NSERC), and from the International Short Visit GrantIZK02Z_175457 funded by Swiss National Science Foundation.

Conflict of Interest

The authors declare no conflict of interest.

Keywords

3D printing, cellulose nanofibers, electrochemical sensors, wireless radiofrequency sensor

Received: October 31, 2018

Revised: November 29, 2018

Published online: December 19, 2018

- [1] R. Martins, I. Ferreira, E. Fortunato, *Phys. Status Solidi RRL* **2011**, *5*, 332.
- [2] A. T. Vicente, A. Araújo, M. J. Mendes, D. Nunes, M. J. Oliveira, O. Sanchez-Sobrado, M. P. Ferreira, H. Águas, E. Fortunato, R. Martins, *J. Mater. Chem. C* **2018**, *6*, 3143.
- [3] D. Gaspar, S. N. Fernandes, A. G. D. Oliveira, J. G. Fernandes, P. Grey, R. V. Pontes, L. Pereira, R. Martins, M. H. Godinho, E. Fortunato, *Nanotechnology* **2014**, *25*, 094008.
- [4] K.-Y. Lee, Y. Aitomäki, L. A. Berglund, K. Oksman, A. Bismarck, *Compos. Sci. Technol.* **2014**, *105*, 15.
- [5] Y. Zhang, P. Song, H. Liu, Q. Li, S. Fu, *Compos. Sci. Technol.* **2016**, *125*, 62.
- [6] F. Hoeng, A. Denneulin, J. Bras, *Nanoscale* **2016**, *8*, 13131.

- [7] G. Siqueira, D. Kokkinis, R. Libanori, M. K. Hausmann, A. S. Gladman, A. Neels, P. Tingaut, T. Zimmermann, J. A. Lewis, A. R. Studart, *Adv. Funct. Mater.* **2017**, *27*, 1604619.
- [8] Y. Li, H. Zhu, Y. Wang, U. Ray, S. Zhu, J. Dai, C. Chen, K. Fu, S.-H. Jang, D. Henderson, T. Li, L. Hu, *Small Methods* **2017**, *1*, 1700222.
- [9] A. E. Jakus, E. B. Secor, A. L. Rutz, S. W. Jordan, M. C. Hersam, R. N. Shah, *ACS Nano* **2015**, *9*, 4636.
- [10] H. Koga, T. Saito, T. Kitaoka, M. Nogi, K. Suganuma, A. Isogai, *Biomacromolecules* **2013**, *14*, 1160.
- [11] R. Martins, D. Gaspar, M. J. Mendes, L. Pereira, J. Martins, P. Bahubalindruni, P. Barquinha, E. Fortunato, *Appl. Mater. Today* **2018**, *12*, 402.
- [12] R. Barras, I. Cunha, D. Gaspar, E. Fortunato, R. Martins, L. Pereira, *Flexible Printed Electron.* **2017**, *2*, 014006.
- [13] S. Sultan, G. Siqueira, T. Zimmermann, A. P. Mathew, *Curr. Opin. Biomed. Eng.* **2017**, *2*, 29.
- [14] K. M. O. Håkansson, I. C. Henriksson, C. D. L. P. Vázquez, V. Kuzmenko, K. Markstedt, P. Enoksson, P. Gatenholm, *Adv. Mater. Technol.* **2016**, *1*, 1600096.
- [15] K. Hölzl, S. Lin, L. Tytgat, S. V. Vlierberghe, L. Gu, A. Ovsianikov, *Biofabrication* **2016**, *8*, 032002.
- [16] D. Espalin, D. W. Muse, E. Macdonald, R. B. Wicker, *Int. J. Adv. Manuf. Technol.* **2014**, *72*, 963.
- [17] K. Fu, Y. Wang, C. Yan, Y. Yao, Y. Chen, J. Dai, S. Lacey, Y. Wang, J. Wan, T. Li, Z. Wang, Y. Xu, L. Hu, *Adv. Mater.* **2016**, *28*, 2587.
- [18] C. Yang, C. P. Wong, M. M. F. Yuen, *J. Mater. Chem. C* **2013**, *1*, 4052.
- [19] J. S. Park, T. Kim, W. S. Kim, *Sci. Rep.* **2017**, *7*, 3246.
- [20] A. J. Michalska, C. Appai-Kusi, L. Y. Heng, S. Walkiewicz, E. A. H. Hall, *Anal. Chem.* **2004**, *76*, 2031.
- [21] T. Zhang, C.-Z. Lai, M. A. Fierle, A. Stein, P. Bühlmann, *Anal. Chem.* **2012**, *84*, 7771.
- [22] H. J. Kim, J. W. Hummel, S. J. Birrell, *Trans. ASABE* **2006**, *49*, 597.
- [23] V. Lutov, K. Mikhelson, *Sens. Actuators, B* **1994**, *19*, 400.
- [24] K. Tian, M. Prestgard, A. Tivari, *Mater. Sci. Eng., C* **2014**, *41*, 100.
- [25] R. Ahmad, N. Tripathy, J.-H. Park, Y.-B. Hahn, *Chem. Commun.* **2015**, *51*, 11968.
- [26] S. Nakata, T. Arie, S. Akita, K. Takei, *ACS Sens.* **2017**, *2*, 443.
- [27] Y.-T. Chen, I. Sarangadharan, R. Sukesan, C.-Y. Hseih, G.-Y. Lee, J.-I. Chyi, Y.-L. Wang, *Sci. Rep.* **2018**, *8*, 8300.
- [28] S. Machida, H. Shimada, Y. Motoyama, *Jpn. J. Appl. Phys.* **2018**, *57*, 04FM03.
- [29] J. V. Pinto, R. Branquinho, P. Barquinha, E. Alves, R. Martins, E. Fortunato, *J. Disp. Technol.* **2013**, *9*, 729.
- [30] D. P. Rose, M. E. Ratterman, D. K. Griffin, L. Hou, N. Kelley-Loughrane, R. R. Naik, J. A. Hagen, I. Papautsky, J. C. Heikenfeld, *IEEE Trans. Biomed. Eng.* **2015**, *62*, 1457.
- [31] H. Wang, X. Wang, A. Barfidokht, J. Park, J. Wang, P. P. Mercier, *IEEE J. Solid-State Circuits* **2018**, *53*, 2043.
- [32] A. Martínez-Olmos, J. Fernández-Salmerón, N. Lopez-Ruiz, A. R. Torres, L. F. Capitán-Valvey, A. J. Palma, *Anal. Chem.* **2013**, *85*, 11098.
- [33] R. A. Potyrailo, W. G. Morris, *Anal. Chem.* **2007**, *79*, 45.
- [34] R. A. Potyrailo, C. Surman, W. G. Morris, S. Go, *TRANSDUCERS 2009 - 2009 Int. Solid-State Sensors, Actuators and Microsystems Conf.* **2009**, 1650.
- [35] J. Kim, S. Imani, W. R. D. Araujo, J. Warchall, G. Valdés-Ramírez, T. R. Paixão, P. P. Mercier, *J. Wang, Biosens. Bioelectron.* **2015**, *74*, 1061.
- [36] J. Kim, I. Jeeran, S. Imani, T. N. Cho, A. Bandodkar, S. Cinti, P. P. Mercier, J. Wang, *ACS Sens.* **2016**, *1*, 1011.
- [37] G. Matzeu, C. Oquigley, E. Mcnamara, C. Zuliani, C. Fay, T. Glennon, D. Diamond, *Anal. Methods* **2016**, *8*, 64.
- [38] M. A. Abrar, Y. Dong, P. K. Lee, W. S. Kim, *Sci. Rep.* **2016**, *6*, 30565.
- [39] A. Craggs, G. J. Moody, J. D. R. Thomas, *J. Chem. Educ.* **1974**, *51*, 541.
- [40] Y. Feng, L. Xie, Q. Chen, L.-R. Zheng, *IEEE Sens. J.* **2015**, *15*, 3201.
- [41] X. Liang, T. Zhao, Y. Hu, R. Sun, *J. Nanopart. Res.* **2014**, *16*, 2578.
- [42] M. L. Beaufort, A. B. Metzner, *Journal of Rheology* **1992**, *36*, 143.
- [43] F. Folgar, C. L. Tucker, *J. Reinforc. Plast. Compos.* **1984**, *3*, 98.
- [44] L. Sanchez-Botero, A. V. Dimov, R. Li, D.-M. Smilgies, J. P. Hinestroza, *Langmuir* **2018**, *34*, 5263.
- [45] A. Querejeta-Fernandez, G. Chauve, M. Methot, I. Gourevich, J. Bouchard, E. Kumacheva, *14th IEEE Int. Conf. on Nanotechnology* **2014**, 567.
- [46] M. K. Hausmann, P. A. Rühls, G. Siqueira, J. Läuger, R. Libanori, T. Zimmermann, A. R. Studart, *ACS Nano* **2018**, *12*, 6926.
- [47] T. Kim, R. Trangkanukulij, W. S. Kim, *Sci. Rep.* **2018**, *8*, 3805.
- [48] J. Wang, S. Huang, X. Lu, Z. Xu, Y. Zhao, J. Li, X. Wang, *J. Mater. Chem. C* **2017**, *5*, 9673.
- [49] V. Kuzmenko, E. Karabulut, E. Pernevik, P. Enoksson, P. Gatenholm, *Carbohydr. Polym.* **2018**, *189*, 22.
- [50] Q.-A. Huang, L. Dong, L.-F. Wang, *J. Microelectromech. Syst.* **2016**, *25*, 822.
- [51] M. A. Peshkova, E. S. Koltashova, G. A. Khripoun, K. N. Mikhelson, *Electrochim. Acta* **2015**, *167*, 187.
- [52] A. Ivanova, K. Mikhelson, *Sensors* **2018**, *18*, 2062.

Appendix C.

Journal paper discussed in Chapter 5

A Humanoid Robot Hand Triggering its Motion through Chemical Sensing

Note: This article is an accepted article. [Kim, T., Kaur, M., and Kim, W. S., (2019) Humanoid Robot Actuation through Precise Chemical Sensing Signals., (accepted, *Advanced Materials Technology*)]

Article Type: Full Paper

Humanoid Robot Actuation Through Precise Chemical Sensing Signals

*Taeil Kim, Manpreet Kaur, and Woo Soo Kim**

Additive Manufacturing Laboratory, School of Mechatronic Systems Engineering, Simon Fraser University, Surrey, BC, Canada

E-mail: [...]

Keywords: chemical sensing, humanoid robot hand, ion selective sensor, eco-friendly 3D-printing

As the need for assistive robots is increasing in aging societies, various assistive robot systems including humanoid robots are developed. Humanoid robotic hands are one of the most useful parts to assist humans efficiently. While sensing pressure or temperature from the robotic hands is extensively studied, sensing chemicals is less widely studied despite of the significant importance. Here, we report a unique platform of smartly moving humanoid fingers triggered by chemical sensing. The actuation triggered by chemical sensing from the 3D-printed ion selective membrane electrodes (ISME) plus inductor capacitor (LC) sensor is mimicking the process of a human body reaction to external stimulus. The LC part is printed with disposable and biocompatible cellulose conductive ink material composed of cellulose nanofibers and silver nanowires dispersed in an eco-friendly solvent, deionized water. R_f intensity change of the LC with ISME of NH_4^+ membrane depends on NH_4^+ ion concentration where R^2 is 0.9576. The smart bending movement of a finger is accomplished by logically programmed actuation through detecting the change of interested ion concentration from 0.01 to 1 M at the ISME sensor and controlling bending angle from 10 to 67 degrees accordingly by utilizing a micro-controller. The overall signal-to-noise (SNR) ratio is over 10. This process may be expanded to applications such as micro robot systems which receive external stimulus, judge, and execute the actuation to carry out programmed tasks.

1. Introduction

As the world population of older adults increases toward 24% by 2030, the need for assistive robots in aging societies is increasing. ^[1] Assistive robots are developed in various forms such as fixed-based robots, mobile robots like wheelchair robot, prosthetic, exoskeleton, and humanoid robots. ^[2] These robot systems can assist humans with difficult tasks or work in a dangerous environment autonomously. ^[3, 4] Robotic systems can also support rehabilitation, assist patients with injuries or paralysis, and help daily life work. ^[5-8] These robots will serve people more effectively as their sensing, judging, and performing action become more accurate and reliable. Humanoid robots or robotic hands are used in various fields like service industries, military, agriculture, and medical applications. ^[9] In an assistive humanoid robot system, a hand is one of the most important parts which can do multiple tasks by holding, pushing, and pulling using multiple fingers. These fingers of a humanoid robot are terminal parts of a robot system where sensors can be applied and utilized in the most efficient way. Usually, human fingers sense physical stimulus like pressure and temperature. And it is not possible to detect chemical materials on human skin. Humans sense taste through the contact of the chemical stimulus on the taste buds of tongues and receptors in noses. Touching chemical materials may be harmful. On the other hand, humanoid robot hands can be designed to detect not only physical stimulus but also chemical stimulus. Humanoid fingers are more appropriate for an assistive humanoid robot to detect chemical stimulus. It is easier for robots to use fingertips to detect chemical ingredients in solutions when they handle these samples with hands because they don't have to move joints a lot to examine samples. Human fingers can do tasks like holding with different patterns of grip and sensing pressure and temperature. ^[10] Recently, humanoid robot fingers are reported with capabilities to sense various inputs such as tactile pressure and temperature as well as taste to secure necessary information in order to support humans and carry out assigned tasks. ^[11-13] A lot of research demonstrated robot fingers which can detect tactile pressure and enable grasping objects. ^[14-16] However, robot fingers incorporated with chemical sensors have been less widely investigated. Here, we report humanoid fingers with electrochemical sensors which can sense ion concentrations and move according to the programmed logic. A platform is made for ion sensing on a robotic hand that combines chemical, material, and electronic efforts to detect physiological information and give feedback both by visual motion and wirelessly

through an inductor-capacitor (LC) sensor. This platform will be helpful for detecting the ions visually on a real time basis and receiving the data wirelessly for analysis at the same time.

Robot hands can be assembled with several parts such as fingers, palm, skin, and parts for actuation. The more complicated this fabrication process becomes, the more time and cost it takes, which makes robot hand systems expensive, and challenging to realize lots of practical applications. One of the main barriers to the widespread adoption of assistive robots is high cost. ^[17] The 3D-printing method is useful for the incorporation of sensors into a robot system. It is also a beneficial technology to reduce time and cost for fabrication. In this report, we demonstrated a functional robot hand with all structural parts as well as sensors printed using two additive manufacturing methods; 1) Fused Filament Fabrication (FFF), and 2) Direct Ink Writing (DIW). Various materials like flexible, rigid, and conductive filaments as well as conductive pastes were utilized according to the design requirements of each parts of the robotic hand.

This study shows mechanical actuation depending on the result of detecting ion solution concentration selectively and sensitively. A robot with this type of sensing system can detect certain ions from patients' sweat for health monitoring or control sodium level in liquid type of food. Wearable chemical sensors applicable on human skins have been developed. ^[18-20] However, applications with printed ISME sensors on humanoid robot fingers have been less studied. The robotic hand we developed has ISME sensors to detect chemical ions and LC circuits for wireless detection. ^[21, 22] One of the merits of detecting from printed sensors is the on-site real time detection instead of waiting for the experiment result from the lab. The wireless detection of electrochemical sensing is beneficial because of its easier communication and convenience. However, the real time wireless detection of a target material is challenging. We adopted a passive LC sensors for the simple and efficient wireless detection of ions. The advantage of wireless passive LC sensors is that it enables efficient detection of signals wirelessly without using additional power sources like batteries. ^[23, 24] Cellulose-based materials were developed and utilized to make eco-friendly flexible sensors. ^[25, 26] The LC printed with the cellulose-based conductive ink of this study has its merits of being disposable, biocompatible, and eco-friendly. Even the solvent used for both cellulose nanofiber (CNF) and silver nanowires (AgNWs) to formulate this cellulose-based conductive ink is the deionized water which does not generate any harmful byproduct during the drying

process after printing. In order to develop optimized LCs for this sensing system, the optimization of inductor was executed based on the study about the inductance of inductors with different shapes. ^[27] Based on the optimized sensor designs, we prepared three bendable fingers which have ISMEs and LC circuits at the fingertips. The finger body and the fingertip were prepared by dual FFF printing with a rigid and a conductive filaments. An ISME sensor and an LC circuits were printed on two sides of a fingertip. Each of three fingers has different PVC membranes for three different target ions such as potassium, calcium, and ammonium ions. These three bendable fingers were assembled on a robot palm which has two fixed fingers. Three fingers were assembled with nylon wires passed through its cores, and the wires were connected to motors for bending. The ISME and 2nd electrodes at the fingertips were wired to a circuit with an Arduino to utilize the change of resistance in the sensor for the actuation of a finger. The novelty of this research is the development of 3D printed ISME LC sensor which enables wireless detection of ion concentration as well as the real time actuation depending on the concentration with simple passive circuit.

We designed a feedback system of a robot hand which includes sensing and bending functions as well as a circuit with a logic. This system is capable to transform the result of chemical sensing into electrical signal and use the signal to trigger mechanical movement accordingly. This robotic hand may be applied to a robot system for monitoring ions in plants where various ion solutions are used. The same system can be expanded to soft robotics to make robot which determines the direction to move depending on the environmental situation or a micro robot that will travel inside a human body and make a programmed movement to do assigned tasks such as drug releasing at a set condition. ^[28, 29]

2. Results

2.1. 3D-printed embedded chemical sensor design for humanoid robot fingers

This study shows smartly moving fingers triggered by chemical sensing. The chemical sensing at the ISME sensor on the bottom side of fingertip will create different levels of resistance in the closed LC circuit depending on applied ion concentrations on ISME. The LC circuit on top of the fingertip will function for wireless detection of different ion

concentrations by measuring variation of resonant frequency (R_f) output's intensity from the LC circuits. **Figure C.1a** shows the schematics of overview of experimental wireless sensing setup. When the robot finger is touching the ion solution, the primary ring connected to the VNA port for S11 reflection method is communicating with the LC circuit printed on the fingertip. ^[30] While the radio frequency signal travels through the primary ring, ISME-LC circuit resonates the most and shows a peak of the returned signal at its resonant frequency. The Figure C.1b shows two types of 3D-printing technologies; 1) DIW extrusion 3D-printing, and 2) FFF used to prepare humanoid robot fingers. The detailed fabrication is described in the MATERIALS AND METHODS section.

2.2. The selection of optimal LC circuits

The design of the inductor in the LC circuit was simulated to secure the best performance. Higher inductance value of the inductor enhances the quality (Q) factor of LC and improve the readout distance for the wireless communication as the Q factor of LC sensor is given as the following equation.

$$Q = \frac{1}{R_S} \sqrt{\frac{L_S}{C_S}} \quad (1)$$

where R_S is the resistance, L_S is the inductance, C_S is the capacitance of LC sensor. ^[31] **Figure C.2** describes the characterization of different inductor design and the simulation result of the chosen ISME-LC circuit when its conductivity between 2 electrodes of the ISME-LC sensor is changed. This is mimicking the resistance changing situation from different ion concentrations applied on the ISME-LC circuits. Figure C.2a shows four distinctive 3D LC circuit designs having different 3D inductors with 3 turns, while the design of the Inter Digitated Capacitor (IDC) is the same. The alphabets assigned to LC designs in Figure C.2a mean the shape of inductors (S: Square, O: Octagonal, H: Hexagonal, C: Circular). The number next to the alphabet means the number of turns of inductors. For example, S3 means square inductor with 3 turns. The square inductor has the largest inductance value as shown in Figure C.2b which shows calculated inductance values for total 12 types of designs, 4 kinds of inductors with 1 to 3 turns of inductors. The calculation of inductance was based on the modified formula which was originally presented for planar

spiral inductors. ^[27, 32] A simple modified version of the original formula is given in the following equation. ^[27]

$$L_{mw} = K_1 \mu_0 \frac{n^2 d_{avg}}{1 + K_2 \rho} \quad (2)$$

where $d_{avg} = 0.5(d_{out} + d_{in})$, d_{out} is the outer diameter, d_{in} is the inner diameter, ρ is the fill ratio, and $\rho = (d_{out} - d_{in}) / (d_{out} + d_{in})^{-1}$. The coefficients K_1 and K_2 are layout dependent as given in Table C.1. μ_0 is the vacuum permeability which is approximately $1.257 \times 10^{-6} \text{ N A}^{-2}$.

Another formula based on current sheet approximation is given as following equation and also gives the same result that the square inductor has the highest inductance value. ^[33]

$$L_{gmd} = \frac{\mu n^2 d_{avg} c_1}{2} \left(\ln \left(\frac{c_2}{\rho} \right) + c_3 \rho + c_4 \rho^2 \right) \quad (3)$$

where the coefficients c_1 , c_2 , c_3 , and c_4 are layout dependent as given in Table C.2.

The Q factor of LC is expected to be around 0.1-0.2 from the equation (1) assuming that the inductance is about 120 μH , the capacitance is around 4 pF, and the resistance is about 30-50 k Ω for the LC. If the inductance is higher, or the resistance or the capacitance is lower, the Q factor of LC will be higher, and the sensitivity of LC sensor will be also improved.

2.3. Simulation of input impedance with different Q factor

Figure C.2d shows the simulated H field distribution with a fingertip for the conductivity of 0.1 and 6 S m^{-1} across two electrodes of the ISME-LC sensor. The H field is stronger around LC for the case of higher conductivity which also shows higher Q factor. Figure C.2e shows the image analysis result of H field distribution around LC (Figure C.2d), where larger percentage of higher H field is observed for the case of higher conductivity, 6 S m^{-1} across two electrodes of the ISME-LC sensor. The same fingertip model was used to find the relation between Q factor and conductivity across electrodes of the ISME sensor. It is known that ISME-LC's electrical conductivity is changed, when different ion concentration is detected in the ISME-LC. And the Q factor is related to the maximum of

the real part of input impedance, $\text{Max}(\text{Re}(Z_{in}))$ of an LC sensor as shown in the following equation. ^[31]

$$Z_{max} = \text{Re}(Z_{in})_{max} / f = f_s = 2\pi R_f L_0 k^2 Q \quad (4)$$

where the resonant frequency R_f can be determined by the $\text{Max}(\text{Re}(Z_{in}))$. The simulation result in Figure C.2c shows the linear relationship between $\text{Max}(\text{Re}(Z_{in}))$ and conductivity across electrodes of the ISME-LC sensor. When the conductivity between two electrodes of ISME-LC sensor is increased, $\text{Max}(\text{Re}(Z_{in}))$ is also increased. Thus, the increasing conductivity between two electrodes of ISME-LC sensor increases Q factor. ISME-LC sensor with high Q factor shows a sharper peak, and a larger R_f intensity. Q factor is inversely proportional to the resistance of LC sensor as shown in equation (1). There are some reports on the reduction of the bulk resistance of ISME when the primary ion concentration is increased. ^[34, 35] If the conductivity between two electrodes of ISME-LC sensor increases, the resistance in the closed LC circuit decreases, and the input impedance increases. As a result, the Q factor is increased like the discussion in our previous study. ^[30] This linear relationship between input impedance and conductivity of ISME electrodes shows that it is possible to detect ion concentration change by monitoring the input impedance change.

2.4. Characterization of ISME-LC sensors on the humanoid hand

Fingertips of humanoid robotic hand were designed to have LC side and ISME side as shown in **Figure C.3a**. The LC was placed on top of the fingertip for the efficient wireless transmission. And the ISME sensor was placed at the bottom of the fingertip for the convenient contact between the fingertip and the chemical solution. This ISME-LC sensor are designed to make a closed circuit when two electrodes of the ISME sensor are connected electronically. The actual printed sample images of both sides of a fingertip is shown in Figure C.3b. The detailed fabrication process is explained in the MATERIALS AND METHODS section. An ISME shows a lower resistance value if the primary ion solution is applied between two electrodes compared to the case of nonprimary ion solution because the membrane allows only primary ions to pass through it. The primary ion means the targeted ion which can be detected by the membrane selectively while nonprimary ions mean all other interference ions. The graph in Figure C.3c shows resistance change across the ISME of K^+ membrane with a drop (150 μ l) of K^+ ion solution

of different concentration on top of the membrane and 2nd electrode. As the ion concentration is increased the resistance across ISME is reduced. This ISME sensor is also capable to detect primary ion (K⁺) selectively among nonprimary ions. Figure C.3d shows the time-dependent resistance change between two electrodes of ISME sensor with NH₄⁺ membrane when the two electrodes were connected with ion solutions of 1 M NH₄⁺, 1 M K⁺, and 1 M Ca²⁺. Even though the resistance is slightly changed during the course of 2 minutes, the resistance values are remaining at three different ranges for different ions. Primary ion demonstrated the lowest resistance, which shows the selectivity of the membrane. Also, these fingers work wirelessly to detect different ion concentrations. Figure C.3e shows R_f intensity change of the LC on a fingertip with the ISME of NH₄⁺ membrane depending on NH₄⁺ ion concentration on top of the membrane. Here the linear regression equation is $y = 1.61x + 19.625$ where R² is 0.9576. Thus, the sensitivity of the ISME LC sensor in this case is 1.61 [dB/M]. As the ion concentration is increased, R_f intensity is increased. As the ion concentration increases, the resistance across the ISME is decreased, and the LC circuit shows a higher Q factor which is determined by observing a larger peak at the resonant frequency of the LC circuit. The relative standard error is defined as the standard error divided by the mean. The relative standard error for the resistance depending on different ion concentrations is less than 3.9% for all cases of ion concentrations for NH₄⁺, Ca²⁺, and K⁺ ions. This shows the reliability of the device is very high, and the result data is reproducible.

The stability of the circuit can be identified by the calculation of signal-to-noise (SNR) ratio which can be defined as the ratio of mean to standard deviation of measurement. The SNR ratio for the resistance depending on different ion concentrations of the built circuit is over 10 for all of the 4 cases of ion concentrations (0.1, 0.5, 1, 1.5 M) for NH₄⁺, Ca²⁺, and K⁺ ions, which shows the reliability of the circuit.

2.5. Demonstration of differential motion of humanoid fingers depending on ion concentration

Both the ISME sensor and LC circuit are designed and built on the fingertip of fingers in a humanoid robotic hand. **Figure C.4a** shows a schematic of full set of hand model with two fixed (a thumb and a pinky), and three movable fingers built with 3D printed palm. A thumb and a pinky are printed along the palm using PLA by FFF. The rest three movable fingers are printed with a flexible filament and are designed as cellular solid composed of octet

truss structure for light weight and mechanical durability. ^[36] This structure allows the finger to be durable in motion due to their high mechanical strength as compared to a solid structure using less material. The fingertips are printed separately with white ABS material which are later assembled with the finger body through a designed lock. This design makes it easy to replace the sensing fingertips. The fingertip has an LC circuit and an ISME sensor printed on top and bottom of the fingertip respectively by DIW printing. The fabricated index, middle, and ring fingers are equipped with individually targeted ion sensing capability with NH_4^+ , K^+ , and Ca^{2+} membranes respectively. The resistance change from the ISME is measured and utilized as a triggering signal to power motors that are used to actuate fingers. Each finger is connected to the control circuit by a couple of thin copper wires attached to two electrodes of the ISME sensor. A 110 rpm micro gear motor with 6 - 12 voltage capacity is used to actuate the finger by pulling a nylon string passing through the center of the porous finger body. In the circuit image of humanoid robotic hand in Figure C.4a, V_{in} indicates the applied input voltage. R_{ISME} is the resistance across the ISME sensor. Known resistor (R_{known}) is the resistance which is set to be in the similar range as the R_{ISME} . When the R_{ISME} and the R_{known} are in a similar range, differentiated output signals depending on different ion concentrations are observed clearly. Thus, the known resistor was chosen to be in the similar range of resistance with the measured R_{ISME} so that the ion concentration change can be detected sensitively. When V_{in} and R_{known} are constant, the voltage applied at R_{known} is determined by R_{ISME} from Ohm's law and Kirchhoff's Current Law. The detailed mechanism is explained in the MATERIALS AND METHODS section. The actual image of selectively moving humanoid fingers triggered by chemical sensing is shown in Figure C.4b, and the index finger is bent as a demonstration. We further check the detection of sensing signal and mechanical movement of the finger based on the concentration of different ions. The particular ion is dropped on the ISME, and the sensing response is detected by measuring the resistance change, as well as visually detected by the corresponding movement of the finger based on the resistance value. In Figure C.4c, as the concentration of potassium ions is increasing, R_{ISME} , the resistance across the ISME sensor detected by the micro-controller is decreasing. It shows the same trend compared to the experimental result in Figure C.3c. Smart bending of the finger where bending angle indicates the ion concentration is also demonstrated for the case of K^+ ions. Figure C.4e shows sequential images of a finger with the potassium ion membrane which bends up to a smaller angle when a drop of potassium ion solution with a lower concentration is applied and bends up to a larger angle

when a drop of potassium ion solution with a higher concentration is applied. The bending angle is approximated through post image processing. Series of triggered bending motion depending on different ion concentrations are captured in the Movie S1 in the Supplementary Material. If the concentration of potassium ion is increased, the R_{ISME} is decreased, and the voltage across R_{known} is increased. To realize the smart moving, we set up 4 different levels of motor speeds for each levels of voltage. Higher concentration of potassium ion induces higher voltage for R_{known} which triggers higher motor speed and result in a larger bending angle. (Figure C.4d) The voltage across the known resistor will be changed when the R_{ISME} is changing. If the input voltage, V_{in} is constant, lower R_{ISME} will make a higher voltage for the R_{known} .

3. Conclusion

A chemical sensing humanoid robot which can trigger its motion differentially is essential for self-protecting and assisting humans in various chemical environments. If the robot detects a hazardous chemical, it can move away from the risk of possible damage caused by contact with the chemical or help human to remain in a safe place. The robot can also help human by checking the quality of water and primary ion levels in food or soil. Then it can give information or adjust the purity or primary ion levels. In this smartly moving humanoid robot system, ISME sensors detect different ion concentration and give different signals to the circuit through a micro-controller. The circuit gives feedback signal to the motor which actuates fingers in different ways. To achieve this goal, the optimized design and fabrication process of a smartly moving humanoid robotic hand based on ISME-LC sensors and metamaterials is presented in this paper. The ISME-LC sensors are embedded at the fingertips of the humanoid robotic hand through optimal 3D-printing technologies. ISME-LC sensor functions based on the fact that the resistance across the ISME changes when the concentration of target ion changes. One of the advantages of ISME-LC sensor is its cost-efficient wireless communication without additional power source such as batteries. Thus, simple and easy fabrication is possible with minimum cost using the demonstrated 3D-printing technologies. The chemical sensing humanoid robot hand can detect ion concentrations with minimum amount of sample solution. We believe that the demonstrated humanoid robot system equipped with biocompatible, eco-friendly, cost-efficient, and sensitive ISME-LC sensor will benefit the field of smart robotics. Our study demonstrates the motion actuation of humanoid robot hand from the chemical

sensing. This topic can be extended for further study to detect different inputs. The ISME-LC sensor system can be used in assistive robots for household or in the medical field.

4. Experimental Section

Fabrication of LC circuits and electrodes: LC and two electrodes of ISME were three dimensionally connected to make a closed circuit when two electrodes of ISME are connected electronically. The center of the inductor on the LC side is connected to the rectangular 2nd electrode on the sensor side across the finger thickness. The end of IDC on the LC side is connected to the circular electrode of ISME on the sensor side. Then LC was printed with CNF composite with silver nanowires (AgNWs) by using 3D-printing system (SHOT mini 100Sx and ML-808GX, Musashi Engineering, Inc.). Thin wires were connected to two electrodes by silver epoxy to make connections to the main circuit including micro-controller: Arduino UNO. The membrane for a primary ion was fabricated by dropping a relevant membrane solution on top of the circular electrode and fully drying in a fume hood for about 14 hours. Three primary ions such as potassium, ammonium, and calcium ions were selected, and membrane solutions prepared for those primary ions were applied to each of the ISME electrodes of three fingers. Each membrane was trained by 1M ion solutions of primary ions by applying enough amount of solution to cover the whole membrane and removing it after 30 minutes for more than 7 times.

The LC circuit was printed by the extrusion printing of a conductive CNF-AgNW ink on top of the fingertip. This fingertip was printed using FFF method with 2 kinds of materials. The first material is ABS, and the second material is Electrifi which is a conductive material. ISME sensor parts were printed at the bottom of the fingertip with silver nanoparticle-based ink by Musashi 3D-printing system. The robot finger body was printed with a flexible material, Semiflex filament with 2 types of truss structures which show different mechanical properties. The first truss structure is octet cellular structure which is for the stiff parts of fingers. The second truss structure is re-entrant honeycomb auxetic structures for the bending part, joints of fingers.

Fabrication of humanoid robotic fingers: Multi-material FFF based 3D-printing method is used to make humanoid fingertips and finger bodies. RostockMax SeeMeCNC® printer equipped with 4 nozzle extruder system is used to fabricate the lattice structures of the soft robotic finger body using Semiflex and the fingertip using ABS and Electrifi. Printing

speed was 15 – 20 mm/sec on average with printing temperature around 220 °C for nozzle and 30 °C for bed. A 0.4 mm aluminum nozzle for metal printing and 0.25 mm brass nozzle for thermoplastic filaments are used with 100 µm printed layer resolution. The dimensions of the printed finger had a length of 120 mm and 15 mm in width. Lastly, the palm is printed using PLA filament for the integration with the motor. A hole with 0.1 mm diameter was designed in the finger to insert a nylon string by being fixed at the top of the finger, which allows the finger to bend when it is pulled.

Actuating mechanism of humanoid fingers: The movement of a finger is based on the actuation through a string that is pulled with a micro gear motor. The resistance across the ISME is measured through an ohm meter made from Arduino to actuate the finger depending on the ion sensing. The change in resistance is seen with respect to a reference resistance when the ion concentration or ion type changes. The resistance threshold for each ion sensor is used to trigger the motor's movement. To make the ohm meter with Arduino, a known resistor and the resistance that need to be measured are set up as a voltage divider to measure the voltage. An algorithm is made to calculate the resistance from Ohm's law. The program sets up analog pin A0 to read this voltage. To check the accuracy of this circuit, test runs were made by a placing a known value resistor. The values were accurate with less than 1% error. This is also when the known resistor has closer value to the unknown resistor. For controlling the motor, L293D motor driver IC is used, programmed with Arduino. The L293D is a 16 pin IC, with eight pins on each side dedicated to control a motor. It consists of 2 H-Bridge which allows to control low current rated motor and enable them to move in both clockwise and anti-clockwise directions. The output pins 3 and 4 are connected to the two terminals of the motor. All the connections between L293D and Arduino are mentioned in table C.S1.

Supporting Information

Supporting Information is available from the Wiley Online Library or from the author.

Acknowledgements

This work received financial support from the Discovery Grant and Discovery Accelerator Supplement Grant 493028-2016, funded by the Natural Sciences and Engineering Research Council of Canada (NSERC).

Received: ((will be filled in by the editorial staff))
Revised: ((will be filled in by the editorial staff))
Published online: ((will be filled in by the editorial staff))

References

- [1] M. Shishehgar, D. Kerr, J. Blake, *Smart Health* **2018**, 7-8, 1.
- [2] D. Feil-Seifer, M. Mataric, *9th Int. Conf. on Rehabilitation Robotics*, Chicago, IL, USA, June **2005**.
- [3] J. Penders, L. Alboul, U. Witkowski, A. Naghsh, J. Saez-Pons, S. Herbrechtsmeier, M. El-Habbal, *Adv. Robot.* **2011**, 25, 93.
- [4] W. Lee, Y. Lee, G. Park, S. Hong, Y. Kang, *Autonomous Robots* **2016**, 41, 243.
- [5] W. H. Chang, Y.-H. Kim, *Journal of Stroke* **2013**, 15, 174.
- [6] I. Naotunna, C. J. Perera, C. Sandaruwan, R. Gopura, T. D. Lalitharatne, *2015 IEEE/SICE Int. Sym. on System Integration*, Nagoya, Japan, December **2015**.
- [7] R. Takashima, H. Kawamoto, Y. Sankai, *2017 IEEE Int. Conf. on Robotics and Biomimetics*, Macau, China, December **2017**.
- [8] N. Fukaya, Y. Ogasawara, *2017 IEEE 6th Glob. Conf. on Consumer Electronics*, Nagoya, Japan, October **2017**.
- [9] C.-H. Ting, W.-H. Yeo, Y.-J. King, Y.-D. Chuah, J.-V. Lee, W.-B. Khaw, Humanoid Robot: A Review of the Architecture, Applications and Future Trend, *Res. J. Appl. Sci., Eng. Technol.* **2014**, 7, 1364.
- [10] N. Kamakura, M. Ohmura, H. Ishii, F. Mitsuboshi, Y. Miura, *Jpn. J. Rehabil. Med.* **1978**, 15, 65.
- [11] Z. Kappassov, J.-A. Corrales, V. Perdereau, *Robot. Autonom. Syst.* **2015**, 74, 195.
- [12] D. Han, H. Nie, M. Chen, X. Wang, *Meas. Sci. Technol.* **2016**, 27, 025105.
- [13] B. Ciui, A. Martin, R. K. Mishra, T. Nakagawa, T. J. Dawkins, M. Lyu, C. Cristea, R. Sandulescu, J. Wang, *ACS Sens.* **2018**, 3, 2375.
- [14] R. Ramalingame, A. Lakshmanan, F. Müller, U. Thomas, O. Kanoun, *J. Sens. Sens. Syst.* **2019**, 8, 87.

- [15] T. Bu, T. Xiao, Z. Yang, G. Liu, X. Fu, J. Nie, T. Guo, Y. Pang, J. Zhao, F. Xi, C. Zhang, Z. L. Wang, *Adv. Mater.* **2018**, *30*, 1800066.
- [16] C. G. Núñez, W. T. Navaraj, E. O. Polat, R. Dahiya, *Adv. Funct. Mater.* **2017**, *27*, 1606287.
- [17] H. Tanaka, M. Yoshikawa, E. Oyama, Y. Wakita, Y. Matsumoto, *J. Robot.* **2013**, *2013*, 1.
- [18] E. Singh, M. Meyyappan, H. S. Nalwa, *ACS Appl. Mater. Interfaces* **2017**, *9*, 34544.
- [19] M. Y. Lee, H. R. Lee, C. H. Park, S. G. Han, J. H. Oh, *Acc. Chem. Res.* **2018**, *51*, 2829.
- [20] A. J. Bandodkar, I. Jeerapan, J. Wang, *ACS Sens.* **2016**, *1*, 464.
- [21] A. Craggs, G. J. Moody, J. D. R. Thomas, *J. Chem. Educ.* **1974**, *51*, 541.
- [22] R. D. Armstrong, G. Horvai, *ChemInform* **1990**, *21*, DOI 10.1002/chin.199015343.
- [23] L. Dong, L.-F. Wang, Q.-A. Huang, *IEEE Sens. J.* **2016**, *16*, 4968.
- [24] L. Qin, D. Shen, T. Wei, Q. Tan, T. Luo, Z. Zhou, J. Xiong, *Sensors* **2015**, *15*, 16729.
- [25] R. Barras, I. Cunha, D. Gaspar, E. Fortunato, R. Martins, L. Pereira, *Flexible Printed Electron.* **2017**, *2*, 014006.
- [26] A. Baptista, J. Martins, E. Fortunato, R. Martins, J. Borges, I. Ferreira, *Biosens. Bioelectron.* **2011**, *26*, 2742.
- [27] S. Mohan, M. D. M. Hershenson, S. Boyd, T. Lee, *IEEE J. Solid-State Circuits* **1999**, *34*, 1419.
- [28] K. J. Filipinski, M. V. Varma, A. F. El-Kattan, C. M. Ambler, R. B. Ruggeri, T. C. Goosen, K. O. Cameron, *Curr. Trends Med. Chem.* **2013**, *13*, 776.
- [29] S. S. Mapara, V. B. Patravale, *J. Controlled Release* **2017**, *261*, 337.
- [30] T. Kim, C. Bao, M. Hausmann, G. Siqueira, T. Zimmermann, W. S. Kim, *Adv. Electron. Mater.* **2019**, *5*, 1970007.
- [31] Q.-A. Huang, L. Dong, L.-F. Wang, *J. Microelectromech. Syst.* **2016**, *25*, 822.
- [32] H. Wheeler, *Proc. IRE* **1928**, *16*, 1398.

- [33] E. B. Rosa, *Bull. Bur. Stand.* **1906**, 2, 161.
- [34] M. A. Peshkova, E. S. Koltashova, G. A. Khripoun, K. N. Mikhelson, *Electrochim. Acta* **2015**, 167, 187.
- [35] A. Ivanova, K. Mikhelson, *Sensors* **2018**, 18, 2062.
- [36] M. Kaur, W. S. Kim, *Adv. Intellig. Sys.* **2019**, 1, 1900019.

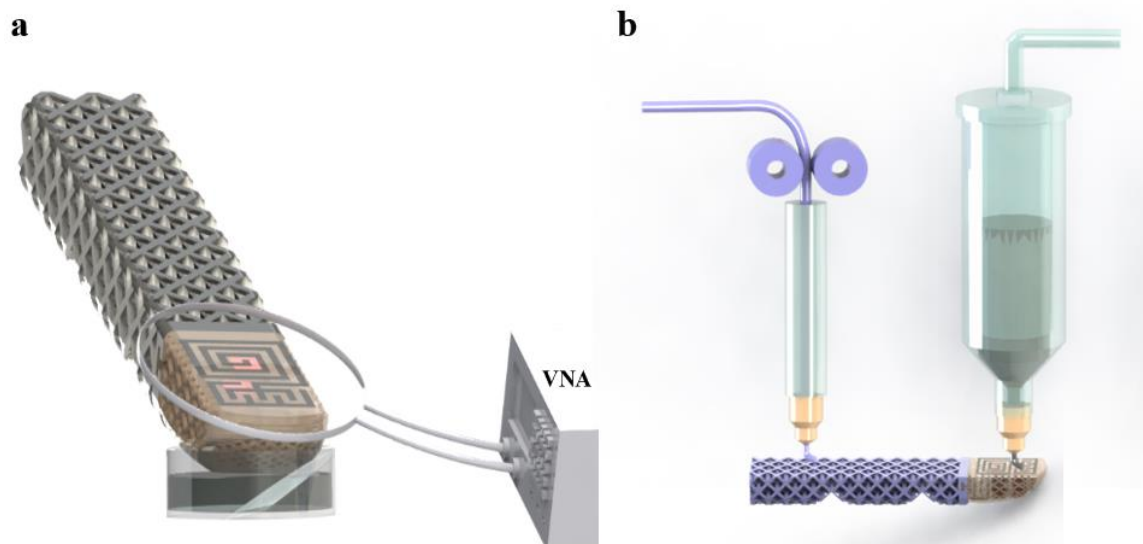


Figure C.1. Schematics of wireless sensing overview and 3D-printing. a) Experimental setup for wireless chemical sensing. b) 3D-printing sequence of humanoid finger body by FFF, followed by DIW printing.

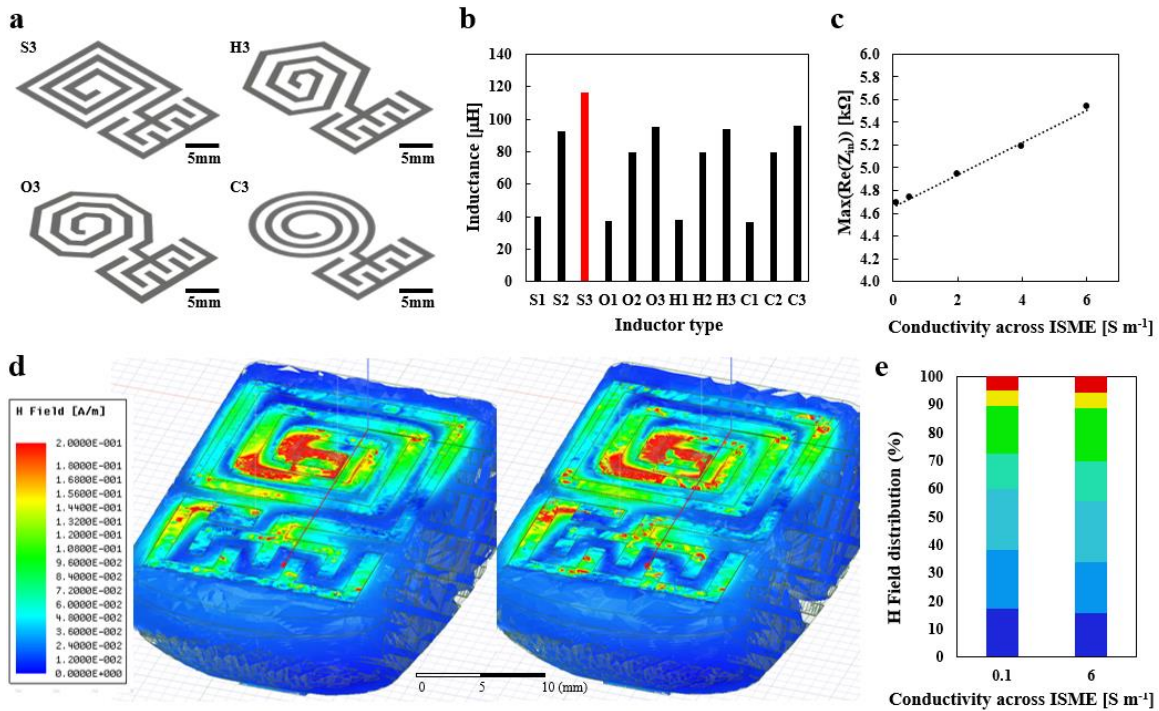


Figure C.2. Characterization of wireless LC circuits. a) Designs for 3D-printing/Wireless characterization of LCs with different inductor shapes (Square, Hexagonal, Octagonal, Circular) with 3 turns. b) Calculated inductance values for 12 types of designs (The alphabet shows the shape of inductors. (S: Square, O: Octagonal, H: Hexagonal, C: Circular) The number means the number of turns.) c) Simulated relation between the conductivity across ISME and maximum real part of input impedance. d) Simulated distribution of H field around the chosen square type LC for the conductivity of 0.1 and 6 S/m across ISME. e) H field distribution comparison of simulation results for the conductivity of 0.1 and 6 S/m across ISME.

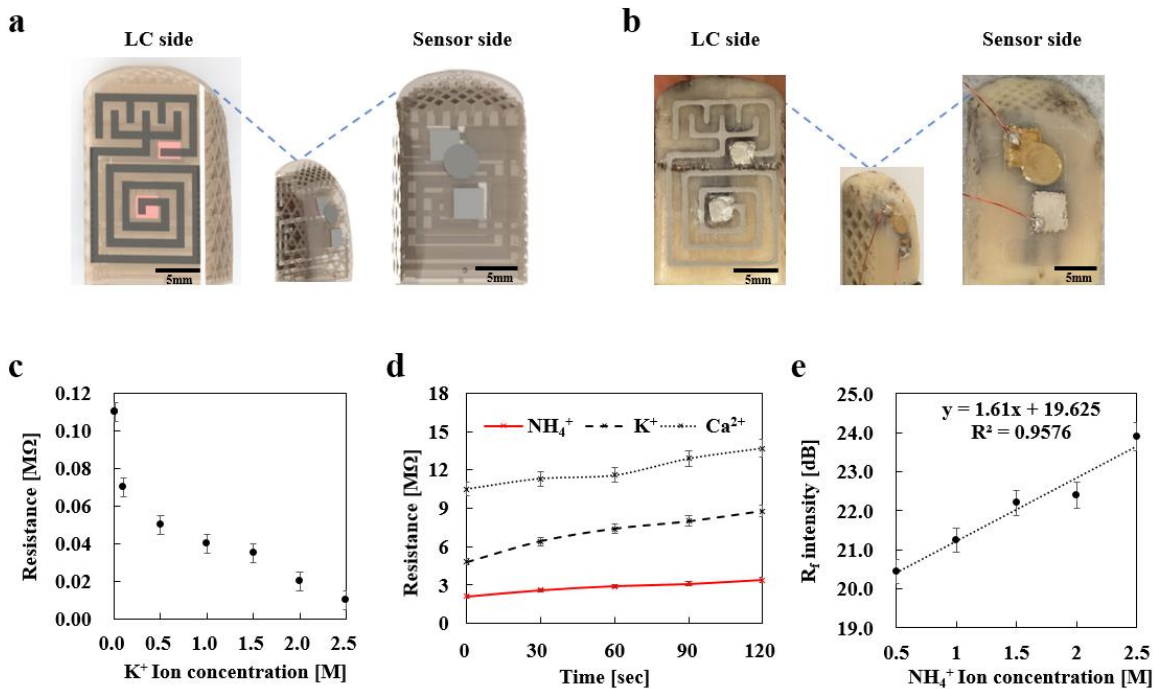


Figure C.3. Qualification of wireless sensing of LC circuit connected with embedded ISME sensors. **a)** Design images of both sides (LC side and Sensor side) of a fingertip. **b)** Actual sample images of both sides of a fingertip. **c)** Electrical resistance change across K⁺ ISME with application of different K⁺ ion concentration. **d)** Electrical resistance change of NH₄⁺ ISME applied with different ions such as 1 M NH₄⁺, 1 M K⁺, and 1 M Ca²⁺ ion solutions depending on time. **e)** R_f intensity change of the LC on a fingertip with the NH₄⁺ ISME depending on NH₄⁺ ion concentration.

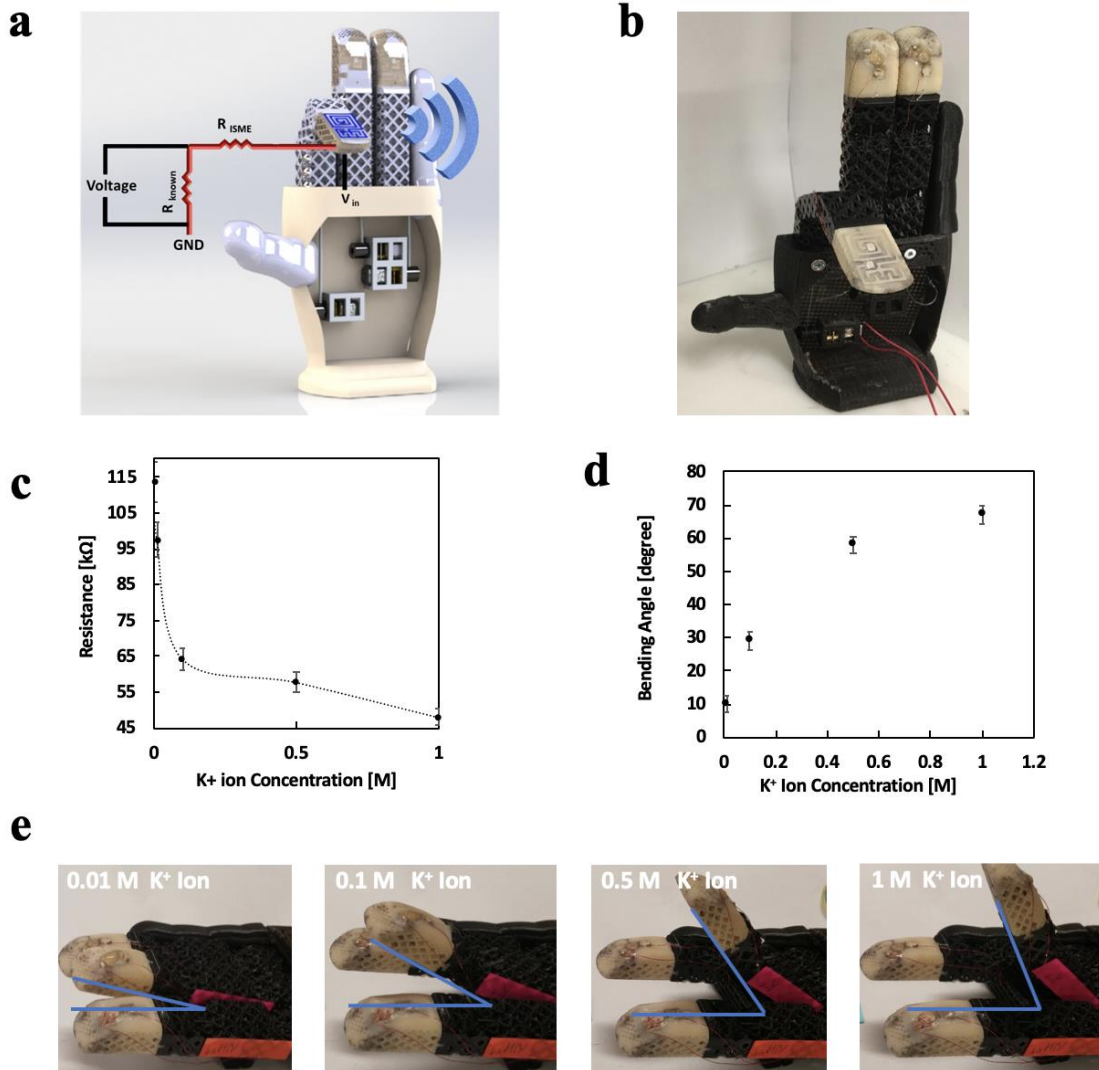


Figure C.4. Differential bending motion of humanoid fingers with quantitative chemical sensing. a) The schematic of humanoid robotic hand with a voltage divider circuit diagram. b) The actual image of fabricated humanoid robotic hand with three movable fingers for detecting primary ions. c) The resistance change depending on the K⁺ ion concentration. d), e) Demonstration of different bending angle of the finger movement actuated by different K⁺ ion concentrations to the extent defined for the voltage thresholds.

Table C.1. Coefficients for modified wheeler expression.

Layout	K_1	K_2
Square	2.34	2.75
Hexagonal	2.33	3.82
Octagonal	2.25	3.55

Table C.2. Coefficients for current sheet expression.

Layout	C_1	C_2	C_3	C_4
Square	1.27	2.07	0.18	0.13
Hexagonal	1.09	2.23	0.00	0.17
Octagonal	1.07	2.29	0.00	0.19
Circle	1.00	2.46	0.00	0.20